Report LR - 604

Experimental Investigation of Tollmien-Schlichting Instability and Transition in Similar Boundary Layer Flow in an Adverse Pressure Gradient (Hartree ß = -0.14)

F.J.M. Wubben

TU Delft

Technische Universiteit Delft

Faculty of Aerospace Engineering
Low Speed Laboratory

Experimental Investigation of Tollmien-Schlichting Instability and Transition in Similar Boundary Layer Flow in an Adverse Pressure Gradient (Hartree ß = -0.14)

F.J.M. Wubben

SUMMARY

The results are presented of a two dimensional experimental investigation of the region of validity of linear stability theory in boundary layer flow, under natural disturbance conditions. Experimental results are compared with two quasi-parallel linear stability computer programs. The first is part of the low speed airfoil analysis and design code of the Low Speed Laboratory (LSL) of the University of Technology Delft (TUD), using tabulated linear stability data. The second program is a finite difference compressible temporal linear stability code, based on Cosal, of the National Aerospace Laboratory (NLR).

The experimental investigations were performed at LSL on the 2m long flat test wall of a small open ended boundary layer wind tunnel with a flexible opposite wall to generate a desired pressure gradient. Except for a short initial pressure region, the pressure distribution corresponded to a Hartree β = -0.14 flow. The free stream turbulence intensity was 0.05%, half of which was contributed by disturbances below 25 Hz, at a free stream reference speed of 10.96 m/s. Boundary layer measurements were done with a single hot wire constant temperature anemometer.

At 23 streamwise stations, mean velocity profiles, power spectra, power distributions across the boundary layer and amplification spectra are presented and compared with boundary layer- and linear stability calculations. Experimental laminar mean velocity profiles compared with results, calculated with a boundary layer code (Bola-2D) of the NLR, showed good agreement. Power distributions across the boundary layer, in the frequency band containing unstable waves, initially showed two maxima, downstream accompanied by a third maximum at the inflection point of the mean velocity profile. This additional maximum was not found from linear stability calculations and hence, may possibly be attributed to non-linear effects. Amplification rates and frequencies of experimental unstable disturbances agree reasonably well with the linear stability calculations.

CONTENTS

Nomenclature 5

1. Introduction 9

2. Numerical methods 12

2.1. The Van Ingen method 12
2.2. The Cosal code 14

3. Test set-up 15

3.1. Windtunnel 15
3.2. The experimental set-up, general description 15
3.3. Test set-up for pressure measurements 16
3.4. Test set-up for hot wire measurements 16

4. Pressure distribution 18

4.1. Choice of distribution 18
4.2. Data reduction and results 19
4.3. Pressure distribution used in calculations 20

5. Data Reduction 21

5.1. Hot wire calibration 21
5.2. Hot wire measurements 24

5.2.1. Mean velocity profiles 24
5.2.2. The sensitivity of the hot wire anemometer 25
5.2.3. Reduction of power spectra 26

5.3. Correction for the wall distance 27
5.4. Boundary layer parameters 28
5.5. Power distributions across the boundary layer 29

5.6. The influence of disturbing signals on the results 30
5.7. Amplification spectra 31

6. Results 34

6.1. Mean velocity profiles 34
6.2. Boundary layer parameters 35
6.3. Some calculations based on linear stability theory 36
6.4. Power spectra 37
6.5. Power distributions across the boundary layer 40
6.6. Amplification spectra 44

7. Some conclusions and recommendations 46

Acknowledgement 48

References 49

Tables

Figures

Appendix A

NOMENCLATURE

a -overheat ratio of hot wire anemometer

a -amplitude of disturbance

a_o -amplitude of disturbance as it just becomes unstable

b -temperature coefficient, [1/K]; equation (5-3)

$E, \bar{E}, e, e'$ -voltage output of hot wire anemometer; mean voltage; fluctuating voltage component; RMS-value of fluctuating voltage component, [V]

$\hat{E}$ -non-dimensional voltage output of hot wire anemometer; equation (5-7)

E_o -calibrated voltage output of anemometer at zero tunnel speed and ambient temperature T_o, [V]; (equation 5-1)

f -frequency, [Hz]

H -shape factor; equation (5-23)

L -test wall length, [m]

n -exponent in hot wire calibration curve; equation (5-1)

n -maximum amplification factor at transition point

n_{max} -maximum amplification factor at arbitrary streamwise position

n_1 -maximum amplification factor at beginning of transition region

n_2 -maximum amplification factor at end of transition region

p -static pressure, $[N/m^2]$

q -dynamic pressure, $[N/m^2]$

R_c -"cold" wire resistance at ambient gas temperature T_c, $[\Omega]$; equation (5-2)

R_L -Reynoldsnumber $\frac{U_{ref}.L}{\nu}$

R_w -hot wire resistance at wire temperature T_w, $[\Omega]$; equation (5-2)

$R_{\delta*}$ $\frac{\tilde{U}_e \delta*}{\nu}$

R_θ $\frac{\tilde{U}_e \theta}{\nu}$

S -sensitivity of hot wire anemometer, [Vs/m]; equation (5-13)

T -temperature, [K]

T_c -"cold resistance" temperature of wire, [K]; equation (5-1)

T_w -temperature of hot wire, [K]; equation (5-1)

T_o -temperature at which E_o is measured, [K]; equation (5-1)

ΔT -overheat, [K]; equation (5-3)

Tu -free stream turbulence intensity; equation (2-2)

U,V,W -velocity components in the x,y,z coordinate system, [m/s]

$\tilde{U},\tilde{V},\tilde{W}$ -mean velocity components, [m/s]

u,v,w -fluctuating velocity components, [m/s]

u', v', w' -RMS-values of fluctuating velocity components, [m/s]

U_{eff} -effective velocity, [m/s]; equation (5-4)

$\hat{U}$ -non-dimensional velocity; equation (5-8)

x,y,z -wind tunnel coordinate system, [m]; figure 3.2

β -Hartree parameter; equation (4-1)

δ -boundary layer thickness, [m]

δ^* -displacement thickness, [m]; equation (5-21)

δ_{99} -wall distance at $(\bar{U}/\bar{U}_e) = 0.99$, [m]

θ -momentum thickness, [m]; equation (5-22)

μ -dynamic viscosity, [kg/ms]

ν -kinematic viscosity, [m^2/s]

ρ -density, [kg/m^3]

Subscripts

cr -critical

e -at boundary layer edge

M -at maximum considered tunnel speed

n -noise contribution

ref -at $x = x_{ref}$ (150.2 mm)

sep -at separation

sett -in settling chamber

u -velocity contribution

x -at boundary layer station with streamwise coordinate x

330 -at boundary layer station x = 330 mm

∞ -reference position

Abbreviations

LSL -Low Speed Laboratory

MS -Mean Square value

NLR -National Aerospace Laboratory

RMS -Root Mean Square value

RPM -Revolutions Per Minute

TS -Tollmien Schlichting

TUD -Delft University of Technology

1. INTRODUCTION

The study of disturbances in two-dimensional boundary layer flow can be divided roughly in four successive stages:

1. the entrance of small external disturbances in the boundary layer;
2. the linear development of Tollmien-Schlichting (TS) waves;
3. non-linear and three dimensional transition phenomena;
4. turbulence.

Only the second stage can be calculated in sufficient detail. At this stage, a simplification of the Navier Stokes equations is used in which velocity perturbations, TS-waves, are thought to be so small that the perturbation equations (see for instance Mack [1]) can be linearized. Experiments (Schubauer and Skramstadt [2], Ross et al [3] showed the validity of this linear stability theory. Because the theory is an initial boundary value problem, solutions are still dependent on the initial TS-waves in stage two.
The mathematical theory, however, can be developed, independently of the initial TS-waves, for the relative disturbances only. A relationship between this initial TS-waves and the external free stream disturbances (like sound and vorticity) seems obvious and is called "the receptivity problem". Despite theoretical (Rogler [4]) and experimental (Kachanov et al. [5]) investigations, the relationship is not completely known, mainly due to the large number of forms of external disturbances.
Exceeding the critical Reynolds number, which is the Reynolds number where initial TS-waves begin to amplify, only disturbances in a limited frequency band will be amplified. In this region the boundary layer acts like a band pass filter plus amplifier.
Downstream, the third stage is entered as non-linear effects become important and linear theory is no longer valid. Experiments in this region have shown that different ways of transition from laminar to turbulent flow are possible. Klebanoff et al. [6] were the first to conduct detailed experiments on transition phenomena and the type of

transition they discovered is known as "the K-breakdown", characterized by the generation of "spikes" in the velocity oscillograms, high frequency fluctuations and the formation of turbulent spots.
A completely different type of breakdown was discovered by Kachanov et al. [7] in which low frequency fluctuations interact with TS-waves and higher harmonics, leading to "spectrum filling" without generation of spikes and turbulent spots.
It was found that the K-breakdown mechanism appeared for larger initial TS-amplitudes than "the subharmonic breakdown" mechanism.
The fourth stage is reached when the flow has become completely turbulent with a smooth and continuous power spectrum.

Because of the complicated character of external disturbances, the receptivity problem and the non-linear wave interaction problem in the third stage, exact prediction of the transition position is still not possible. Therefore, semi-empirical methods, like the so-called e^n method, are designed to estimate this position. At first instance, the maximum amplification factor, n, was chosen 9 and fixes the transition position after a linear stability calculation is performed. This implicitely means that the third stage, which is normally bounded to a small streamwise region is also incorporated. Flat plate experiments showed the dependency of the maximum amplification factor on the spectrum integrated power or turbulence intensity of external disturbances. The latter relation is used in the present e^n-method (see section 2.1) at the Low Speed Laboratory (LSL) of the Delft University of Technology (TUD). Hence, the receptivity problem is bypassed in an empirical way.

In the present report, an experimental two-dimensional study is presented on the stability of the laminar boundary layer (stage 2) and the transition to turbulence (stage 3) under natural disturbance conditions (i.e. without the use of forced disturbances such as due to a vibrating ribbon). One of the objectives was to obtain an overall view of the processes leading to transition as well as to become more familiar with the measurement techniques involved. Main attention was directed on comparison of experimental amplification rates with linear stability theory.

Measurements were performed with a single hot wire probe and spectral analysis was applied to present the frequency dependent evolution of perturbations in streamwise direction.

2. NUMERICAL METHODS

Experimental data were compared with two e^n-methods, the "Van Ingen method" (see Van Ingen [8]) and the Cosal computer code (see Malik & Orszag [9] and Malik [10]) of the National Aerospace Laboratory (NLR). In both methods, the flow is considered locally parallel (V = 0) assuming that the local mean velocity profile determines the stability characteristics while the local boundary layer growth is neglected. Because the overall mean flow is permitted to change, a quasi parallel theory is obtained. The Van Ingen method uses spatial stability theory and the Cosal code temporal theory. Transformation of the spatial results into the temporal or the reverse, can be done with the Gaster transformation (Mack [1]), which strictly is only valid for small local amplification rates. Comparison of calculated spatial data with Gaster transformed temporal results have shown only small differences in practical situations (see for instance Tjandra [11]). Only a brief description of both methods will be given here. More detailed descriptions can be found in the original references.

2.1. The Van Ingen method

The Van Ingen method is part of the two-dimensional incompressible airfoil analysis program used at LSL (Van Ingen et al. [12]) which uses a modified Thwaites method for calculation of the laminar boundary layer. It is assumed that all possible stability diagrams form a one parameter family with the critical Reynolds number as a parameter. This family is derived from a compilation of stability data for the similar Falkner Skan mean velocity profiles, published by Wazzan et al [13] and Kummerer [14] and solutions of the Rayleigh equation for the inviscid stability of reversed flows as occurring in separation bubbles (Van Ingen [15]). All these data have been reduced to a table containing about 600 numbers. Relating the critical Reynolds number to a characteristic parameter of the velocity profile (for instance the shape factor), a stability diagram can be composed for any velocity profile. In the present method, $R_{\theta_{cr}}$ is made a known function of m/m_{sep} with $m = -\frac{\theta^2}{\nu}\frac{dU}{dx}$ and m_{sep} the value of m at separation. It should be remarked that the method is based on reading results from

rather small scale graphs in references [13] and [14] so that the final accuracy may not be very high. At present the whole method is being updated using results of recomputed stability data.
As already remarked in chapter 1, an emperical relation is used between the power content of external disturbances and the maximum amplification factor, n. This relation, deduced from known flat plate experiments (see Van Ingen [16] and Mack [17]) with zero pressure gradient, is also used for other boundary layers suggesting that n is independent of the boundary layer. However, this has not been proved. At LSL, the beginning and end of the transition region is defined respectively at the positions where

$$n_1 = 2.13 - 6.18 \text{ LOG } Tu \tag{2-1a}$$

and

$$n_2 = 5.0 - 6.18 \text{ LOG } Tu \tag{2-1b}$$

with Tu, the free stream turbulence intensity (in %), defined as

$$Tu = 100 \left(\frac{1}{3} (\bar{u}^2 + \bar{v}^2 + \bar{w}^2)\right)^{\frac{1}{2}}/U_\infty \tag{2-2}$$

or for isotropic turbulence ($\bar{u}^2 = \bar{v}^2 = \bar{w}^2$)

$$Tu = 100 \left(\bar{u}^2\right)^{\frac{1}{2}}/U_\infty \tag{2-3}$$

For Tu < 0.1%, the famous flat plate experiments of Schubauer and Skramstadt [2] no longer showed a shift of the transition point for decreasing Tu. This is probably due to sound disturbances which are dominating velocity fluctuations and control the transition proces. It should be observed that the value of Tu as defined by equations (2-2) and (2-3) is based on all velocity disturbances present and not only on those with the "dangerous frequencies". For this reason an "effective freestream turbulence intensity" is used, where sound disturbances and the effective part of the spectrum only, are taken into account. It will be clear that direct measurement of Tu_{eff} is almost

impossible, therefore Tu_{eff} should be obtained from a calibration between the experimental transition position, the corresponding calculated maximum amplification factor and equations (2-1).

2.2. The Cosal code

The Cosal computer code is the compressible version of the "Sally" code. The latter uses incompressible stability theory so it solves the three-dimensional fourth order Orr-Sommerfeld equation.
Cosal solves an eigenvalue problem of an eight order system of differential equations which describe the stability of small disturbances in three dimensional compressible boundary layers. In two dimensional boundary layers, as in the present experiment, the system reduces to 6th order. Cosal is designed to calculate amplification factors as well as eigenfunctions and eigenvalues for swept and tapered wings.
Laminar mean velocity profiles, necessary input for Cosal, are calculated with the Bola-2D program of NLR (Lindhout et al. [18]). The NLR version of Cosal, based on a listing published by Malik [19], was programmed by de Bruin of NLR.

3. TEST SET-UP

3.1. Windtunnel

Experiments were performed in the small boundary layer tunnel of LSL. This tunnel is an open tunnel with a 2m long test section and is driven by a direct current motor with maximum RPM of 3000. The fan has 12 vanes.
The settling chamber has a 0.8 x 0.8 m cross section, the entrance of the rectangular test section has a cross section of 0.08 x 0.48 m which gives a contraction ratio of 16.7 (figure 3.1).
The flat test wall and flexible opposite wall of the test section have a span of 0.48 m and are mounted vertically between two horizontal plates (figure 3.2). The flexible wall is used to obtain a varying cross section area in streamwise direction, so a prescribed pressure distribution can be realized. It is made of transparant PVC and consists of a periodic pattern of three kinds of successive cells (figure 3.3). One cell is partly cut to allow flexibility while the neighbouring cell is equipped with a pressure orifice. Suction slits are made in the third kind of cell which are connected to the suction network of LSL, to prevent boundary layer growth (or worse, separation).
Suction at the leading edge is possible to remove the boundary layer of the contraction wall, hence, a new boundary layer starts at the leading edge of the test wall.

3.2. The experimental set-up, general description

A cartesian coordinate system is defined with the origin at the centre of the test wall leading edge (figure 3.2). The x-axis is directed in streamwise direction along the centre of the test wall, the y-axis is directed towards the flexible wall, normal to the test wall, and the z-axis points to the bottom of the channel along the test wall leading edge.
The test wall is made of chipboard with a plastic coating and has dimensions 2 x 0.48 x 0.02 m. The metal leading edge of the wall is wedge shaped (see figure 3.1) with a length, in x-direction, of 100 mm.

The pressure distribution along the test wall was measured with 42 pressure orifices, divided over two streamwise rows.
The 15 suction cells of the counter wall were connected to the suction network of LSL using 15 calibrated constrictions. The pressure difference over a constriction, was a direct measure for the amount of suction air.
The atmospheric pressure was read from a barometer while the temperature was determined at the end of the test section with a Mensor, PT-100 element, thermometer.

3.3. Test set-up for pressure measurements

Figure 3.4 gives a diagram of the test set-up for pressure measurements. The pressure orifices in the test wall were connected to a Mensor quartz tube manometer via a scanning valve.
The static pressure in the settling chamber was taken as reference, which is nearly the total pressure because of the large contraction ratio. The manometer signal was fed to a Watesta digital counter and was read out and averaged via an interface, by the HP-1000 laboratory computer. The pressure near the leading edge ($x < 150$ mm), where no pressure orifices were present, was measured, with a long static pressure probe (ϕ 6 mm), put into the tunnel via the open downstream end. Four pressure orifices were fitted in the probe, 170 mm from the nose evenly distributed over the circumference. The probe was attached to a traversing system and pressed to the test wall by metal braces which were taped to the wall.

3.4. Test set-up for hot wire measurements

The (single) hot wire (figure 3.5), manufactured at LSL consisted of tungsten wire with a copper coating for the insensitive part. The sensitive part was obtained by etching away the copper coating and had a length of 1 mm and a diameter of 5 μm. The hot wire probe was attached to a support sting, put into the tunnel via one of the 15 measuring holes located along the centre line of the test wall. Holes which were not used, were filled with plasticine to restore the smooth surface. Hot wire probe and support sting were fixed to each other by

means of a variable connector which enabled five streamwise positions for one measuring hole (figure 3.5). The support sting was attached to a traverse system for y-adjustment of the hot wire. The system was placed on a rubbery underground, close to the test wall, to limit vibrations of the support sting (figure 3.2).
The distance of the hot wire to the wall was determined with a Taylor-Hobson telescope and Spindler & Hoyer spotlight (appendix A). Figure 3.6 gives a diagram of the hot wire test set-up. The hot wire was connected to a Dantec (56C01) constant temperature anemometer with overheat ratio a = 0.8.
For measurement of the RMS-value, the anemometer output signal was fed to a DISA bandpass filter with frequency band 5 - 2000 Hz and roll-off rate 18 dB/octave. A Fluke (8842A) digital Volt/RMS meter was used for measuring the mean- and RMS voltage via an electronic switch.
The filtered signal was also input for a Bruel & Kjaer (type 2031) narrow band frequency analyzer. Volt/RMS meter and analyzer data were read out by the computer and stored on disk and magnetic tape.
Halfway the experiments, some instruments were disconnected. At the time, the old set-up was obtained again, a different electronic noise spectrum was present. A different grounding of the instruments before and after the break-up was the reason for different noise spectra. The same noise spectra or likewise, the same test conditions could not be obtained any more, resulting in two different measurement series, both given in the results.

4. PRESSURE DISTRIBUTION

4.1. Choice of distribution

Many measurements in the past have been performed in a flat plate boundary layer. In the present case it was thought wortwhile to select again a similar flow but now with an adverse pressure gradient. For that, a Hartree velocity distribution $U_e(x)$, defined as:

$$\frac{U_e}{U_{ref}} = \left(\frac{x}{x_{ref}}\right)^{\frac{\beta}{2-\beta}} \qquad (4\text{-}1)$$

was chosen to be imposed on the flat test wall of the tunnel. In equation (4-1), U_{ref} is the free stream velocity at the first pressure orifice (x_{ref} = 150.2 mm) and β is a constant.
An important feature of Hartree flow is the similarity of its boundary layer mean velocity profiles. The consequence of this choice is that for linear stability calculations only one stability diagram is required. Thus, possible errors arising from interpolation between several stability charts are reduced to a minimum.
It should be noted that the similarity of the mean velocity profiles will not lead to similarity in the amplitude distributions of a disturbance because these will be dependent on $R_{\delta*}$. This will be discussed in more detail in chapter 5.

A Hartree β = -0.14 and Reynoldsnumber, R_L equal to 1.47 million appeared to be the right combination to obtain the transition point at about x = 800 mm. This last position was chosen as a compromise: on the one hand to avoid the two turbulence wedges starting at top and bottom junctions of the leading edge, but on the other hand to obtain a laminar region as long as possible. At x = 1200 mm, the wedges joined at the centre of the test wall. The amount of suction on the opposite wall was estimated by discretisizing the distributed suction needed, according to a calculation with an adapted version of Head's method, using Raspet's criterium of constant R_θ.
"Natural suction" was obtained at the leading edge of the test wall by sufficiently narrowing the trailing edge cross section inducing an

overpressure at the bleed with respect to the atmospheric pressure. Consequently, a suction pump, generating fairly high sound levels which possibly disturb the flow, was not necessary.

4.2. Data reduction and results

The edge velocity distribution, assuming constant density, was calculated from

$$\frac{U_e}{U_{ref}} = \left(\frac{p_{sett}-p}{p_{sett}-p_{ref}}\right)^{1/2} \qquad (4\text{-}2)$$

with p the measured local static pressure, p_{sett} the static pressure in the settling chamber and p_{ref} the static pressure at x_{ref}. Because of the large contraction ratio, the total pressure could be approximated by p_{sett} with sufficient accuracy (maximum deviation about 0.26 Pa, i.e. 0.2% U_{ref}). Because of the non-dimensional character of equation (4-2), the assumption gave errors which fell within the scatter of the measurements (standard deviation 0.1% U_{ref}). Because of variation in the RPM setting of the tunnel motor, tunnel speed and temperature, the Reynolds number, R_L, varied with a standard deviation of 1%.
For x approaching zero, U_e/U_{ref} in equation (4-1) approaches infinity, values which of course can not be realized physically. Hence, at x-positions smaller than x_{ref}, experimental values were allowed to deviate from equation (4-1). Deviations were also permitted at streamwise locations beyond the transition region (x > 1000 mm) to obtain a convenient outlet pressure.

Measurements with the long static pressure probe at streamwise positions smaller than about 80 mm showed a dependence on the rotational orientation of the pressure probe. Obviously, a pressure gradient normal to the wall, close to the stagnation point, was the reason for this. Measurements were performed for that rotation angle which gave the lowest velocity at the stagnation point. Results in this region should be regarded with some suspicion.

Figure 4.1 shows one of the measured velocity distributions (values in table 4.1). Small undesirable displacement of the counter wall could occur when touching the wall during the positioning of the hot wire. Therefore, the velocity distribution was verified regularly and the counter wall was adjusted when necessary within a tolerance of about 0.3% U_{ref}.

4.3. Pressure distribution used in calculations

Because of the limited accuracy of the pressure measurements at small streamwise positions, those values are not used in calculations. At $x = 98$ mm, the mean velocity profile was measured with a hot wire, from which the momentum thickness was calculated. This value was used as starting point in boundary layer calculations with the LSL program and Bola. The same value was obtained from calculations assuming a Blasius boundary layer flow from the leading edge.
From $98 \leq x \leq 150$ mm, computations done with the LSL program as well as with Bola, were performed with the measured pressure distribution (see table 4.2) while downstream, equation (4-1) was used. It will be clear that differences may occur between the experimental velocity distribution and the distribution used in calculations (see for instance figure 4.1). In particular, $\frac{dU_e}{dx}$ can differ locally considerably from the value derived from equation (4-1).

5. DATA REDUCTION

5.1. Hot wire calibration

As mentioned in chapter 3, hot wire boundary layer measurements were performed with a constant temperature anemometer. An empirical relation between anemometer voltage output, E, and flow velocity, U_{eff}, reads according to Hinze [20]:

$$E^2 = (E_o^2 + BU_{eff}^n)(1 - \frac{T-T_c}{T_w-T_c}) \qquad (5\text{-}1)$$

In this equation, E_o is the anemometer output at zero tunnel speed and corresponding fluid temperature T_c. (At temperature T_c, the overheat ratio is adjusted). B is a constant and n is an exponent with value about 0.5. E_o, B and n are wire dependent quantities. The second term on the right-hand side expresses the correction for changing ambient air temperature, T, to be applied. The overheat ratio, a, is defined as

$$a = \frac{R_w-R_c}{R_c} \qquad (5\text{-}2)$$

with R_w the wire resistance at wire temperature T_w and R_c the "cold resistance" at temperature T_c. (T_w-T_c) is the overheat which can be calculated from

$$(T_w - T_c) = \Delta T = \frac{R_w-R_c}{bR_c} = \frac{a}{b} \qquad (5\text{-}3)$$

with b the temperature coefficient which for tungsten has the value, $5.2.10^{-3}\ (K)^{-1}$.

Positioning of the hot wire parallel to the z-axis and assuming a stationary and two dimensional parallel mean flow (V = 0), the effective velocity, U_{eff}, which cools the wire is obtained from

$$U_{eff} = ((\bar{U} + u)^2 + v^2)^{1/2} \approx \bar{U} + u + \frac{v^2}{2(\bar{U}+u)} \qquad (5\text{-}4)$$

For low turbulence intensities, the third term at the right-hand side can be neglected, leaving only the streamwise velocity components $\bar{U}$ and u.

In the present experiment, relation (5-1) was approximated by

$$E^2 = (E_o^2 + B\, U_{eff}^{\,n})(1 - \frac{T-T_o}{\Delta T}) \qquad (5\text{-}5)$$

with $\Delta T = 230$ K and E_o and T_o respectively voltage and fluid temperature at zero tunnel speed. Notice that T_o not necessarily equals T_c. Equation (5-5) written in non-dimensional form gives

$$\hat{E} = \hat{U} \qquad (5\text{-}6)$$

in which

$$\hat{E} = \frac{E^2/(1 - \frac{T-T_o}{\Delta T}) - E_o^2}{E_M^2/(1 - \frac{T_M-T_o}{\Delta T}) - E_o^2} \qquad (5\text{-}7)$$

and

$$\hat{U} = (\frac{U}{U_M})^n \qquad (5\text{-}8)$$

with E_M, T_m and U_M the quantities at the maximum considered tunnel speed. The advantage of this non-dimensional notation is the vanishing of the constant B.
The exponent n can now be calculated from

$$n \text{ LOG } (\frac{U}{U_M}) = \text{LOG } \hat{E} \qquad (5\text{-}9)$$

A two point calibration, at zero and maximum tunnel, speed provides E_o, T_o, E_M, T_M and U_M, sufficient to use equation (5-6).

Preparatory measurements showed that relation (5-6) was not valid in the complete range of considered velocities (see figure 5.1 which

shows that the calibration points are not on a linear curve. Therefore, a more complicated relation between mean velocity and voltage was obtained from a calibration considering more calibration points. This relation reads

$$\hat{U} = f(\hat{E}) \tag{5-10}$$

$f(\hat{E})$ is a polynomial of third degree with coefficients A_o, A_1, A_2 and A_3 obtained from a least squares analysis. The coefficient A_o equals zero by definition. The exponent n, which in principle can be chosen universally constant (e.g. 0.5), is also calculated with a least squares analysis with the help of equation (5-9). The consequence is that $f(\hat{E})$ is as linear as possible. (If A_2 and A_3 are zero, equation (5-6) is valid).

During a calibration, the hot wire was positioned in the centre of the test section (outside the boundary layer) close to a cross section, containing a pressure orifice. First, E_o was measured at air temperature T_o. The air temperature was measured at the end of the test section assuming the temperature constant over the test section. To ensure a zero velocity in the vicinity of the wire when measuring E_o, a small box was placed temporarily around the probe.
Next, the voltage output, E, corresponding air temperature, T, and dynamic pressure, q, at the nearest pressure orifice were measured at several tunnel speeds, varying between about 2 and 14 m/s. In all experiments, time-averaged quantities were approximated by taking the ensemble average. For calibrations, the number of hot wire voltage samples was chosen 800 at sample frequency 66.67 Hz. Hence, the sampling time was 12 s. The dynamic pressure was averaged over 50 samples. At tunnel speeds smaller than about 2 m/s, q could not be measured with sufficient accuracy. This means that the relation between voltage and velocity, $f(\hat{E})$, in this low velocity region is fully determined by calibration points measured at larger velocities and at zero tunnel speed.
Assuming constant density, the non dimensional velocity was obtained from

$$\frac{U}{U_M} = \left(\frac{q}{q_M}\right)^{1/2} \qquad (5\text{-}11)$$

Figure 5.1 shows a typical calibration curve, $f(\hat{E})$, as well as the measured calibration values. $f(\hat{E})$ is nearly linear while the exponent n has nearly the value 0.5. Comparison of two calibrations performed at different air temperatures differ only little at first sight (figure 5.2). Both calibrations were reduced for the same E_o, T_o and n for comparison. Attention should be paid in concluding that both calibrations provide the same results because U_M and E_M are different for both calibrations, scaling the measured values to each other. Presentation of figure 5.2 in dimensional form shows indeed differences. These differences are probably due to an inaccurate temperature correction in equation (5-5). However, because all results are presented in non-dimensional form, the absolute error ($\Delta U/U_e$) could be kept small, 0.15%. Comparable errors were found in the boundary layer measurements here also due to the temperature correction term.
Repeated calibration of the wire (once a week) appeared very important because of ageing effects resulting in changed wire properties. Comparison of two calibrations performed one month after each other, gave an absolute error of 1.8%.

5.2. Hot wire measurements

Boundary layer measurements were performed at 23 locations along the test wall in the laminar and transitional region of the flow. At several positions across the boundary layer, mean voltages, RMS-values and power spectra were measured. In this report, only data reduced from mean voltages and power spectra will be presented.

5.2.1. Mean velocity profiles

Mean velocity profiles were obtained by measuring the mean voltage, $\bar{E}$, at several y-positions across the boundary layer, and corresponding air temperature T. Substitution of both values in equation (5-10) provided $(\bar{U}/\bar{U}_M)$. This value was divided by $(\bar{U}_e/\bar{U}_M)$, measured at the boundary layer edge, resulting in $(\bar{U}/\bar{U}_e)$.

The determination of the hot wire wall distance y is described in Appendix A. Measuring stations across the boundary layer were between about 0.15 mm and 3δ. At smaller distances, an increased voltage output was observed resulting from heat loss to the wall (Vagt [21]).

The total number of samples was determined by taking K-times, N voltage meter readings (which were averages of 4 samples), such that the total average over these 4KN samples differed less than a suitably chosen percentage from the average over (K-1)N readings (4(K-1)N samples).

$$\left|\frac{\bar{E}_{(K-1)}}{\bar{E}_K} - 1\right| < \epsilon \qquad (5\text{-}12)$$

The percentage ϵ was chosen 0.01%. This gives a scatter of 0.04% in the mean velocity (see equation 5-1)). It should be remarked that the error with respect to the real time average can be larger than 0.04% because both averages in relation (5-12) may be shifted in the same direction with respect to the time average.

5.2.2. The sensitivity of the hot wire anemometer

Before a mathematical derivation for the sensitivity of the hot wire anemometer is given, a physical interpretation is offered in figure 5.4, where the relation between voltage output and velocity is presented schematically. Consider a small velocity fluctuation Δu, at two mean velocities, $\bar{U}_1$ and $\bar{U}_2$. The figure shows immediately that the corresponding voltage fluctuation Δe_1 at $\bar{U}_1$ is larger than Δe_2 at $\bar{U}_2$, or

$$\left(\frac{de}{du}\right)_1 > \left(\frac{de}{du}\right)_2$$

The conclusion can be drawn that the hot wire anemometer is more sensitive at lower mean velocities.

The sensitivity, S, of the hot wire anemometer can now be approximated as (see Hinze [20])

$$S = \frac{e'}{u'} \tag{5-13}$$

with e' the measured RMS-value of the observed fluctuating voltage signal and u' the RMS-value of the corresponding velocity fluctuation. Differentiation of equation (5-10) with respect to E (assuming $E = \bar{E} + e$; $U = \bar{U} + u$) and time averaging, provides the relation between u' and e'.

$$\frac{e'}{u'} = \frac{(\bar{E}_M^2/(1 - \frac{T_M - T_o}{\Delta T}) - E_o^2)\, n\, f(\hat{E})}{(2\bar{E}/(1 - \frac{T - T_o}{\Delta T}))f'(\hat{E})\, \bar{U}} \tag{5-14}$$

$f'(\hat{E})$ is the derivative of $f(\hat{E})$ (see equation (5-10)) with respect to $\hat{E}$. Equation (5-14) expresses the sensitivity of the anemometer.

5.2.3. Reduction of power spectra

The voltage power spectra, measured with the frequency analyzer, were expressed in dB and covered a frequency band of 0-1000 Hz subdivided in 400 intervals of 2.5 Hz each. The number of dB at a certain frequency interval is defined as

$$\text{number of dB} = 20(\text{LOG}(e'/10^{-6})) \tag{5-15}$$

with 10^{-6} (= 1 μV) the reference level and e' the RMS-value within the considered frequency interval.
Combination of equations (5-14) and (5-15) yields (u'/$\bar{U}$) which is further reduced to

$$\frac{u'}{\bar{U}_e} = (\frac{u'}{\bar{U}})(\frac{\bar{U}}{\bar{U}_e}) \tag{5-16}$$

($\bar{U}/\bar{U}_e$) was already obtained in section (5.2.1).

Power spectra were measured and averaged over the same time interval as for the RMS-meter measurements. The sampling time of the latter was determined in a similar way as for the mean voltage measurements

(equation 5-12) although now also the average over (K-2)N readings was included. The three values had to differ less than 1%. This gives a scatter of 1% in u' (see equation 5-14).
Velocity power spectra are finally presented as $LOG(u'/\bar{U}_e)^2$ against frequency (in Hz).

5.3. Correction for the wall distance

Errors, in the determined wall distance of the hot wire will shift the velocity profile to or from the wall, particularly creating errors in δ^* and H.

In order to correct for this error, at first instance the Hartree mean velocity profile for β = -0.14 (from Smith [22]) was used. This limits the applicability to the downstream part of the laminar region where the Hartree pressure distribution was present (x > 150 mm). The theoretical profile from reference [22] is presented in the well-known non-dimensional distance η, defined as

$$\eta = y \left(\frac{U_e}{(2-\beta)\nu x}\right)^{1/2} \qquad (5\text{-}17)$$

To obtain a scaling factor between the experimental and theoretical profiles, independent of the experimentally determined wall distance, the following procedure was used. In both distributions, the values of y and η were determined at $(\bar{U}/\bar{U}_e)$ = 0.25 (η_1 and y_1) and 0.75 (η_2 and y_2) with Lagrange interpolation (see figure 5.5). With these, a factor k was found giving the relation between y and η

$$k = \frac{\eta_2 - \eta_1}{y_2 - y_1} \qquad (5\text{-}18)$$

The necessary correction is then obtained by

$$\Delta y = \frac{\eta_1}{k} - y_1 \qquad (5\text{-}19)$$

The mean velocity distribution at x = 98 mm was corrected in a different way. The experimental pressure distribution (figure 4.1) at this position, shows a pressure gradient of about zero. At smaller x-positions, there is a favourable pressure gradient but this is in the area where results were dependent on the rotation angle of the pressure probe. For zero pressure gradients, a Blasius mean velocity profile ($\beta = 0$) can be expected, characterized by an inflexion point at the surface. The low velocity region of this profile can be approximated fairly well by a straight line. Doing so, a correction was found.

In the region around x = 150 mm, experimental velocity profiles deviated from the theoretical Hartree profile, because of history effects of the preceding non-Hartree boundary layer flow.
Therefore, all laminar experimental velocity profiles were also compared with the calculated Bola-velocity profiles. The Bola profiles were presented in y_B -($\bar{U}/\bar{U}_e$) so a quite arbitrary relation was used to find a correction

$$\Delta y = \frac{1}{3}\{(y_B-y)_{\bar{U}/\bar{U}_e=0.25} + (y_B-y)_{\bar{U}/\bar{U}_e=0.5} + (y_B-y)_{\bar{U}/\bar{U}_e=0.75}\} \quad (5\text{-}20)$$

The velocity profiles in the transition region were not corrected because of a lack of calculated data.

5.4. Boundary layer parameters

The measured velocity profiles were integrated both with Simpson's rule as with Akima's "spline" method, yielding the three boundary layer parameters defined as:

The displacement thickness,

$$\delta^* = \int_0^{\delta} (1 - \frac{\bar{U}}{\bar{U}_e})\, dy \quad (5\text{-}21)$$

the momentum thickness,

$$\theta = \int_{o}^{\delta} \frac{\bar{U}}{\bar{U}_e} \left(1 - \frac{\bar{U}}{\bar{U}_e}\right) dy \qquad (5\text{-}22)$$

and the shape factor,

$$H = \delta^*/\theta \qquad (5\text{-}23)$$

Boundary layer parameters were calculated both with and without correction for the wall distance.

5.5. Power distributions across the boundary layer

The power content of a specific frequency band was obtained from the velocity power spectra by summation of the MS-values, u'^2, of all frequency intervals (2.5 Hz wide) falling within the considered frequency range. This procedure, applied to all spectra measured at a boundary layer station, provided the power distribution across the boundary layer for the specific frequency band. Because the momentum thickness, θ, is not seriously affected by errors in the low velocity region (e.g. due to errors in wall distance), power distributions are presented as LOG $(u'/\bar{U}_e)^2$ - (y/θ). In these, y is corrected for the wall distance with the Bola matching procedure (see section 5.3).

During the experiments, an investigation was performed on the influence of time weighting functions on power spectra. Time weighting functions in spectral analysis are used to limit the number of samples in the time function by multiplication of the time signal by a time window. The disadvantage of the use of time windows is that, according to Thrane [23], it gives rise to a leakage of power from the original frequency into the neighbouring frequencies. During the measurements, a Hanning weighting function was used. Comparison of the total powers calculated from the spectra and the MS-values measured with the RMS-meter showed 1.37 higher values for the first mentioned. It appeared that the RMS-meter measured the exact value for a sinusoidal signal. The factor 1.37 was not corrected for. In calculations of the amplification rate of a disturbance this factor cancels out.

5.6. The influence of disturbing signals on the results

The anemometer velocity signal, $\bar{E} + e_u$, representing the instantaneous velocity, $\bar{U} + u$, is contaminated by electronic noise and other disturbing signals, e_n, generated by the connected instruments. This last contribution will not correlate with the flow velocity but is treated in the data reduction procedure as if representing a velocity. The instantaneous total voltage which is presented to the voltmeter can be written as

$$E = \bar{E} + e_u + e_n \tag{5-24}$$

By taking the time average of equation (5-24), it follows that the mean voltage will not be influenced by disturbing signals provided that $\bar{e}_n = 0$.
The MS-value after filtering reads

$$\overline{(e_u + e_n)^2} = \overline{u^2 + 2e_u e_n} + \overline{e_n^2} \tag{5-25}$$

Assuming that e_u and e_n are uncorrelated, the second term on the right-hand side is zero. Equation (5-25) shows the influence of small disturbing signals on the MS-value or signal power.

In the following, some interesting properties of the signal will be discussed with the help of two figures made in the frequency domain. Figure 5.6 shows three voltage power spectra measured at three levels in the boundary layer at x = 276 mm. Because the fan of the tunnel motor has 12 vanes rotating at about 1600 RPM, a frequency of 320 Hz in velocity was expected. Indeed, this frequency is visible in the spectra as a large discrete peak. This peak which is part of the velocity signal, grows with decreasing wall distance or likewise, grows with decreasing mean velocity. This growth can be explained when considering the mean velocity dependence of the anemometer sensitivity. Transforming the figure to velocity power spectra (figure 5.7), a constant peak value is obtained. This means that the amplitudes of the velocity disturbances generated by the fan, maintain

nearly the same level across the boundary layer (see also figure 6.12).
Peaks at 612.5 Hz and 640 Hz behave like the peak at 320 Hz. The first is thought to be originating from sound produced by the motor, the second is the first harmonic of the 320 Hz signal. Higher harmonics of periodic signals always appear as the signal is not sinusoidal (Priestley [24]). All above-mentioned peaks appeared to be dependent on the RPM and are counted among the velocity signal.
Further analysis of figures 5.6 and 5.7 exhibits discrete peaks at 50 Hz (the electric mains frequency) and multiples of 50 Hz. The presence of the latter demonstrates the non-sinusoidal character of the electric mains. It will be clear that those peaks do not represent velocity fluctuations and should be considered as disturbing signal.
Regarding figure 5.6, the peaks are hardly influenced by changes in sensitivity. Reduction of figure 5.6 to 5.7 shows a decrease of the peaks at smaller mean velocities, inversely proportional to the increased sensitivity.
The same behaviour can be observed at frequencies, not included in the discussion till now, above 400 Hz, attributed to "white noise". Of course, a contribution of the velocity signal may be present in this region but it is dominated by noise.
At for instance 170 Hz, the roles are reversed (figure 5.7). The velocity signal dominates the noise and the first increases slightly at smaller wall distances.

5.7. Amplification spectra

As already mentioned in section 4, amplitude distributions (or power distributions) of a disturbance will alter in streamwise direction. Because in this experiment, in principle similar mean velocity profiles are present, the alteration is only attributed to the changing Reynolds number, $R_{\delta*}$, in streamwise direction.
The consequence of alteration is that several definitions are known in literature to define amplification of small disturbances. Saric & Nayfeh [25] illustrate the possible conflicting definitions with the help of figure 5.8. Following lines of constant η, shows a destabilizing effect along $\eta = \eta_1$ and a stabilizing effect along $\eta = \eta_2$ although

the maximum amplitude has not changed. Saric & Nayfeh remark that the change of total energy of the disturbance across the boundary layer should be a better criterium. However in literature, the experimental amplification rate, (a/a_o), is mostly determined along lines of constant η or maximum u'. (In these, a is the local amplitude of a disturbance and a_o, the amplitude of a disturbance as it just becomes unstable).
In the present experiment, it has been decided to determine amplification rates from spectra measured closest to lines of constant (y/θ). For Hartree flow the following relation is valid

$$\frac{y}{\theta} = \frac{\eta}{\Theta} \qquad (5\text{-}25)$$

with Θ the non-dimensional boundary layer momentum thickness which for $\beta = -0.14$, is equal to $\Theta = 0.53856$ (Smith [22]). Thus for Hartree flow, lines of constant (y/θ) are equivalent to lines of constant η.

Both numerical methods considered, are based on locally or quasi-parallel theory, resulting in another difficulty. In this theory, the local growth rate will not be dependent on the normal coordinate y neither will the computed amplification rate which is the integral of the local growth rate in time or space. As discussed, the experimental amplification rate depends on the path through the boundary layer in streamwise direction. This makes it difficult to compare experimental amplification rates with quasi-parallel theory. However, because of a lack of non-parallel numerical results, data were presented compared with quasi-parallel calculations. It should be noted that the streamwise change of the amplitude distribution originates from the quasi-parallel theory because $R_{\delta*}$ is allowed to change in streamwise direction.

In theory, a_o is thought to be an arbitrary constant while in practice of course a_o may be different at every frequency and location in the boundary layer. In contrast to vibrating ribbon experiments, in the present experiment, the levels of a_o were very small, such that contributions of disturbing signals were dominant. Therefore, amplification rates of disturbances (experimental as well as computed) were

determined with respect to a reference station (x = 330 mm) where sufficient amplification of the disturbances has occurred. The amplitudes of the experimental disturbances at the reference station are expressed as a_{330}.

The RMS-values of a sinusoidal signal with amplitude a, equals ($a/\sqrt{2}$). Hence, the quotient of the RMS-values of two sinusoidal signals provides the ratio of their amplitudes. The spectral RMS-values will be proportional to the amplitude, thus, amplification of a disturbance, with certain frequency, was calculated from the velocity power spectra by taking the quotient of their respective RMS-values. Because velocity power spectra were made non-dimensional with $\tilde{U}_e$, equation (4-1) is used in the reduction. Graphs of $LN(a_x/a_{330})$ as function of frequency will be referred to as amplification spectra.
The advantage of reduction to amplification spectra is the vanishing of the electric mains peaks provided that both velocity power spectra were measured at the same mean velocity in the boundary layer. (Note that the power content of electric mains peaks depends on the mean velocity (see section 5.6)). Peaks at the fan blade frequency (± 320 Hz), its harmonic frequency (± 640 Hz) and the frequency of the motor sound (± 612.5 Hz) will also vanish, provided that both spectra were measured at identical motor RPM.

6. RESULTS

6.1. Mean velocity profiles

All results presented in this chapter are, unless mentioned otherwise, corrected for the error in the experimentally determined wall distance of the hot wire, with the Bola matching procedure described in section 5.3. Mean velocity data and velocity power spectra can be made available on floppy disk by LSL. Applied wall distance corrections and file names of uncorrected mean velocity profiles and spectra are given in tables 6.1. Stations measured twice or even more times are accompanied with a superscript for distinction. As mentioned in section 3.4, power spectra were obtained in two measurement series, also given in tables 6.1. At a number of stations no power spectra will be presented because they were measured for other filter settings than the principal series. The mean velocity will not be influenced by filter settings, provided that disturbances are small, so all measured mean velocity profiles are given in the tables and were used for reduction to boundary layer parameters.

The boundary layer development, in the laminar region ($x \leq 709$ mm) compared with Bola mean velocity profiles is presented in figures 6.1. Agreement between experiment and computation is quite satisfactory except for some local regions close to the wall, attributed to local deviations in the experimental pressure gradient not taken into account in the calculations. Because no correction was applied for variations in tunnel speed, small deviations from unity can be observed at the boundary layer edge.
The points plotted in the origin are added for calculation of boundary layer parameters. It follows that the wall distance was determined with a standard deviation of 0.05 mm.

Figure 6.2 shows experimental and Bola mean velocity profiles at two boundary layer stations compared with the Hartree $\beta = -0.14$ profile, presented as η -(U/U_e) (Smith [22]). In these, the first two profiles were matched with the Hartree profile at $(U/U_e) = 0.5$, from which a y-conversion constant, k, was found:

$$k = \frac{\eta_{0.5}}{y_{0.5}} \qquad (6\text{-}1)$$

Experimental and Bola profiles were then transformed in η-ordinates. At x = 155 mm, differences are considerable because of history effects due to the preceding non-Hartree β = -0.14 boundary layer. However, good agreement is obtained at x = 458 mm indicating that the Hartree flow is approached further downstream.

6.2. Boundary layer parameters

Boundary layer parameters δ^*, θ and H, reduced from the uncorrected mean velocity profiles, are presented in the figures 6.3 and table 6.2. The figures show a comparison with Bola laminar boundary layer computations.
Differences between the calculated curves and experimental values may be due to errors in the determined wall distance, differences between pressure distribution used in calculations and experiment, the variation in tunnel speed, possible errors in the hot wire calibration curve and errors in the temperature correction term of equation (5-5). Differences in integration results between Simpson's rule and Akima were only found in the third decimal.

Figures 6.4 and table 6.3 show the boundary layer parameters of corrected mean velocity profiles. Corrections are almost entirely visible in δ^* when compared with figure 6.3a because δ^* is especially sensitive to changes in the wall region (see equation (5-21)). The opposite is true for θ which is scarcely influenced. Therefore θ is a suitable parameter to scale the corrected normal distance y. Remaining differences between the experimental H and calculations (figure 6.4c) are mainly due to differences in θ (figure 6.4b).
The development of the shape factor shows the onset of transition at about 700 mm. At about x = 900 mm transition seems to be completed. Finally, table 6.3 also gives (δ_{99}/θ) with δ_{99} the y-ordinate at $(U/U_e) = 0.99$. For comparison, $(\delta_{99}/\theta) = 7.370$ for Hartree β = -0.14.

A comparison between calculations with Bola and the LSL program is presented in the figures 6.5. The figures of δ^* and H show a difference at about 150 mm due to the sudden increase in pressure gradient for which the Thwaites method in the LSL program is rather sensitive. Figure 6.5b shows that θ is less influenced.
Downstream, good agreement is obtained with H approaching the value of 2.963 slowly, which is the value for Hartree β = -0.14 (Smith [22]).

6.3. Some calculations based on linear stability theory

Figures 6.6 shows the local amplification factors, calculated with the Van Ingen method, for several frequencies, as function of the streamwise coordinate x. Figure 6.7, further shows the envelope for maximum amplification at any frequency.
At x = 700 mm and 900 mm, where the beginning and end of the transition region were observed, maximum amplification is found near 127 Hz and the maximum amplification factors, n_1 and n_2, are respectively 11.3 and 13.8. The corresponding "effective" free stream turbulence intensity according to equation (2-1), is 0.035%.

Replotting figure 6.6 as function of frequency provides figure 6.8 which is in essence an example of an amplification spectrum, dealt with in section 5.7. However, here the undefined initial amplitude a_o is used as reference. The figure clearly demonstrates a shift of the maximum and unstable modes, to smaller frequencies when proceeding downstream. Unstable TS-frequencies can be expected between 15 and 425 Hz.

A comparison between amplification curves calculated with Cosal and the LSL program is presented in the figures 6.9 and 6.10. The differences may be due to:

a. inaccuracies and/or interpolation errors in the table with stability data used in the Van Ingen method (see also section 2.1);
b. differences in the input data of Cosal and the van Ingen method calculated respectively with Bola-2D and the modified Thwaites method;

c. the fact that Cosal is based on temporal stability theory from which the plotted spatial results are derived with the Gaster transformation. This transformation is strictly only valid for small local amplification rates.

A recent comparison at NLR (Tjandra [11]) of Cosal results, with Van Ingen data and spatial stability calculations performed by Arnal [26], for three Hartree flows (β = -0.15, 0, 1), shows the same tendency as found in the figures 6.9 and 6.10 for β = -0.15. That is, larger "Van Ingen amplification rates" in comparison with Cosal and Arnal data. The two last-mentioned show, good agreement. No significant differences were observed in the frequency ranges of unstable modes, calculated with the three methods for β = -0.15.
Concluding, the first cause, above-mentioned, appears to be most important reason for differences in figures 6.9 and 6.10.

6.4. Power spectra

Power spectra are shown in figures 6.11 for 19 boundary layer stations at different wall distances in the laminar and transitional flow region. The free stream spectrum, which changes little downstream for one series, is always presented as reference for spectra measured within the boundary layer.
At small x-positions where spectra are mainly dominated by disturbing signals, the boundary layer spectrum measured closest to the maximum in power over the frequency interval 25-1000 Hz, is shown. At larger streamwise stations, boundary layer spectra are presented, measured closest to (y/θ) = 0.7 and 2.8 at which, maxima in power distributions were observed for the frequency interval 25-200 Hz (see section 6.5).

The first station considered in the figures 6.11 is at x = 98 mm which shows the features of disturbances already discussed in section 5.7. In this region several disturbances are present which vanish in streamwise direction. However, at low frequencies (< 30 Hz), a large power contribution can be observed. This hump will not damp nor amplify downstream and strongly resembles the high fluctuation levels at very low frequencies (about 5 Hz) in open jet facilities (Meier et

al. [27], and Michel and Froebel [28]). Those high fluctuations in open jet facilities are induced by the large vortices in the free shear layer of the jet. Although the present experiments were not performed in an open jet, an unsteady velocity field may have been generated in the laboratory (experiments were performed in an open tunnel) which may affect the flow inside the test section. According to Meier et al. [27], those low frequency oscillations do not influence the transition process.

Up to x = 276 mm, no clear amplification of disturbances can be observed probably due to dominating disturbing signals.
Only at x = 330 mm, a clear hump can be observed around 190 Hz, representative of TS-frequencies, plotted in figure 6.8. This station is shown for both series because it was used as reference station for amplification spectra.
Further downstream, the hump slowly shifts to lower frequencies and increases in magnitude. At x = 330 mm, the maximum of the hump is found in the spectrum, measured closest to $(y/\theta) = 2.8$ but at x = 430 mm, the maximum is shifted towards the wall. At this last station, a second hump appears around 100 Hz with its maximum at $(y/\theta) = 2.8$. The appearance of a second hump seems to resemble the experiments of Kachanov et al. ([7] and [29]) possibly corresponding to sub-harmonics of TS-waves.
In Kachanov's experiments a fundamental wave (TS-wave) was generated by a vibrating ribbon at the initial part of a flat plate at zero incidence. Downstream, breakdown started with the appearance of low frequency fluctuations including the subharmonic (half the fundamental frequency). Results corresponded in general with a theoretical model of Craik [30] in which the resonant interaction of a fundamental wave with a pair of oblique travelling subharmonic waves is described mathematically. This means that the appearance of subharmonics goes hand in hand with the appearance of three dimensionality and according to reference [7], appears much earlier than previously supposed.
The observation of a whole bunch of low frequency oscillations including the subharmonic could be explained by means of the parametric resonant interaction of small initial subharmonic disturbances with the fundamental wave. Phase and amplitude of initial subharmonics

change randomly in time like external free stream disturbances. The consequence is that amplitude and phase of a resonantly amplified subharmonic also change with time although the phase, changes with jumps of 180^0 as the amplitude of the subharmonic becomes zero. Fourier analysis of such signals provides a bunch of low frequency oscillations including the subharmonic. The amplitude distribution of the fundamental wave across the boundary layer initially showed a typical TS-profile with two maxima, downstream accompanied by a third maximum. The amplitude distribution of the subharmonic exhibited one maximum close to the critical layer.

In the present experiment attention was focussed on the amplification of natural disturbances. Hence, in power spectra, amplitudes corresponding to possible existing subharmonics will overlap with fundamental contributions. It is nearly impossible to distinguish between the two. Only at frequencies at the boundary of the unstable zone, the subharmonics will dominate the fundamental or the reverse. Initially, the power dip at 125 Hz (x = 330 mm) may be the boundary between subharmonic and TS-contributions but it can also be due to smaller external disturbances at this frequency. The latter reason could not be demonstrated from measured free stream spectra because of the influence of disturbing signals. Downstream, amplification is also observed at 125 Hz although the power dip remains visible.
At x = 518 mm, above 200 Hz only the peaks generated by the tunnel motor actually correspond to the velocity signal. All the other contributions can be attributed to disturbing signals with decreasing powers at smaller wall distances. An interesting change in this behaviour can be observed in the spectra at x = 568 mm. Particularly the frequency interval 200-300 Hz shows increased power with respect to the free stream spectrum, but also at higher frequencies a growth can be observed. It will be evident that now no longer disturbing signals dominate the velocity signal. The same phenomenon was observed in the experiments of Kachanov et al. [7] due to interaction processes between the low frequency oscillations and the fundamental wave which is the start of the filling of the spectrum to turbulence. Hence, at this station and further downstream, differences between linear stability calculations and experiments can be expected.

At x = 709 mm where clear differences between the experimental and calculated mean velocity profile were seen for the first time, all spectral components grow evenly. Oscillograms showed the typical intermittency phenomenon characterized by high frequency fluctuations alternating with more regular laminar flow.
Even further downstream, the spectra become smooth with only one maximum in power distributions across the boundary layer, at which the spectra in figures 6.11 are presented.

6.5. Power distributions across the boundary layer

To demonstrate some interesting properties of the signal, power distributions are presented at x = 276 mm in various frequency bands (figure 6.12). Plotted points for one (y/θ) are deduced from the same spectrum. Hence, over 800 spectra were measured to determine power distributions at all considered boundary layer stations.

Comparison of distributions determined in the frequency ranges 0-1000 Hz and 25-1000 Hz shows the large contribution of low frequency oscillations (< 25 Hz). The free stream turbulence intensity, in which all disturbances are represented, was 0.05%, half of which was contributed by disturbances below 25 Hz. It will be clear that usage of this turbulence intensity in an e^n-method may give an inaccurate transition prediction because disturbances which will not affect the transition process are also included. A better criterion can possibly be obtained by considering only disturbances which will actually amplify and take part in the transition process. It should be noted that it is actually this effect that led van Ingen to use an "effective" free stream turbulence intensity (see section 2.1). This "effective" turbulence intensity will in general differ from the experimental free stream turbulence intensity. The latter indeed differs from the "effective" value of 0.035%, given already in section 6.3.
To avoid the contributions of the electric mains, several distributions are shown for frequency bands avoiding the electric mains frequency and its harmonics. The distribution for 305-345 Hz, dominated by the peak at 320 Hz corresponding with the fan frequency, remains at a fairly constant level except for very small wall distances.

Distributions for 205-245 Hz, 255-295 Hz and 355-395 Hz demonstrate the typical profiles of disturbances dominated by disturbing signals. As discussed in paragraph 5.7, the contributions of disturbing signals in voltage power spectra change only little across the boundary layer. Hence, the considered distributions will be directly proportional to the inverse of the hot wire sensitivity.

The spectra discussed in the previous paragraph showed interesting phenomena in the frequency band 25-200 Hz for which power distributions are presented in figure 6.13 at several streamwise stations. This frequency band will later be subdivided in four smaller ranges to avoid the electric mains peaks and to demonstrate the frequency dependence of the power distribution shape.
The figure shows maxima at three levels of (y/θ) (maximum A at about 0.7, B at about 2.8 and C at about 8.3). Power spectra were presented at the first two levels in the previous section. Only at x = 330 mm and 709 mm fewer than three maxima are visible. At the first, the signal to noise ratio is too low to observe possible other maxima while at x = 709 mm the transition region is entered. Non-similarity of streamwise power distributions as discussed in section 5.8, is scarcely visible.
It will be clear that these distributions are mixtures of all kinds of modes. Therefore, smaller frequency ranges are considered in the following, starting with 155-195 Hz where a tendency to amplification was observed for the first time (figures 6.14).At small x-positions, the presence of the B-maximum in the distributions is much less clear than in the previous figure. However down-stream, the considered maximum grows quicker than the A- and C-maximum and becomes the absolute one near x = 568 mm. At x = 709 mm, a different distribution is observed again. Figures 6.15 show the evolution for the frequency band 105-145 Hz in which the B-maximum is the absolute from the very start (x = 396 mm).At even lower mid-frequencies, the B-maximum is represented more strongly (figure 6.16) while in the frequency band 25-45 Hz (figure 6.17) only the B-maximum is left over. So, it appears that the second maximum becomes more important at smaller frequencies.

A comparison of these results with Cosal calculations is presented in figures 6.18 and 6.19. The Cosal amplitude distribution was determined from the calculated eigenfunction, except for an arbitrary multiplicative constant, and was therefore matched arbitrarily at the C-maximum of the experimental power distribution.
Figures 6.18 show experimental power distributions for the frequency interval 155-195 Hz, compared with Cosal results of a 175 Hz wave. (Calculated power distributions did not change much with frequency (compare for instance figures 6.18 with 6.19)). At x = 330 mm, with relatively small signal to noise ratio, matching gives no consistent results. Downstream where the velocity signal dominates disturbing signals, agreement is much better. In calculations, the amplitude approaches zero at $y = \infty$ which is a boundary condition of the Orr Sommerfeld equation. However in experiments, at some boundary layer thicknesses, an almost constant power content is found, representative for the free stream oscillations in the considered frequency band. It should be noted that this value is also affected by contributions of disturbing signals. Hence, particularly at upstream boundary layer stations, differences in the free stream are observed.
Figures 6.18 show, when matched at the C-maximum, good correspondence at the A-maximum and at the absolute minimum in the boundary layer which coincide with the 180^0 phase reversal of a TS-wave. Only at downstream stations, the experimental minimum is found somewhat further from the wall compared with the calculations.
The Cosal distributions compared with linear stability calculations performed by Arnal [25] at nearly corresponding R_θ and Hartree β =-0.15, showed good agreement.
The B-maximum is not found from the linear stability calculations and was therefore attributed to non-linear effects. Figures 6.19 show similar results for the experimental frequency band 105-145 Hz compared with calculations at 130 Hz. The same trends are visible as in the previous figure with the B-maximum clearly present in the experimental results, contrary to the computations.

The existence of the B-maximum can not be explained with certainty from these experiments. Only some reflective thoughts about its presence will follow below.

Because the second maximum becomes more and more dominant at smaller frequencies and knowing from references [7] and [29] that a subharmonic maximum is found near the critical layer, the second maximum may possibly be related to subharmonic oscillations. At relatively high frequencies (155-195 Hz), initial TS-waves may dominate subharmonics because the latter will be related to TS-waves with twice the frequency of these subharmonics, which were not found from the spectra. Of course, TS-waves may be present at these frequencies (310-390 Hz) but are buried in contributions of disturbing signals. It is thought that corresponding subharmonics are of the same- or lower magnitude at these small x- positions. Further downstream, the subharmonic influence seems to grow and is added to TS-distributions. At smaller frequencies, subharmonics correspond to more powerful TS-waves. Consequently, these subharmonics will amplify relatively more due to resonant interaction processes and are therefore clearer visible in power distributions.
Considering figure 6.17 again, the frequency interval 25-45 Hz shows no typical TS-profile but rather the shape of a subharmonic distribution (see reference [29]). At this frequency band, linear instability is predicted further downstream (figure 6.8) so subharmonics may dominate TS-waves.

As discussed in the previous paragraph, an interesting change was observed in the spectra above 200 Hz, at boundary layer station x = 568 mm. To demonstrate this change across the boundary layer, power distributions were determined in the frequency band 505-545 Hz. At small x-positions (< 568 mm), this band is dominated by disturbing signals as shown in figure 6.20. The power content in the free stream may differ from one distribution to the other because experiments were performed in two measurement series with different noise spectra.
At x = 568 mm, a discontinuity is visible in the distribution, close to the inflexion point in the mean velocity profile. Similar discontinuities are present at x = 616 mm and 673 mm, here located at the boundary layer edge. It appears from the figure that the power content in the boundary layer is increased suddenly when approaching the wall. From this it seems that possible interaction processes between low frequency oscillations and fundamentel waves, at first remain confined

to only a part of the boundary layer. Downstream, the whole boundary layer is affected and at x = 709 mm, a quite different distribution can be observed with the maximum at the inflexion point of the mean velocity profile. This last station is considered as the start of the transition region.

To demonstrate the gradual filling of the spectrum in the transition region across the boundary layer, power distributions are presented in various frequency bands (figure 6.21). At x = 709 mm, the point of phase reversal can still be observed in several distributions but downstream it has disappeared. Only at x = 872 mm, the distribution shape becomes independent of the corresponding frequency band. The next two stations show turbulent distributions with a rather constant power across the boundary layer except for the wall region where a clear maximum is visible.

6.6. Amplification spectra

Amplification spectra, already discussed in section 5.7, were determined from velocity power spectra of corresponding series, measured closest to (y/θ) = 0.7 and 2.8 where maxima were observed in the power distributions for the frequency band 25-200 Hz. As demonstrated in the previous paragraph, the A-maximum corresponds with linear stability calculations provided that the matching at the C-maximum was valid, so experimental amplification spectra at this level are expected to agree with computations.

It should be remarked that amplification is with respect to the spectrum, measured at x = 330 mm. Hence, the vertical scale in the amplification spectra is not the "n_{max}-factor". The calculated (with the van Ingen method) "n_{max}-factor" has already the value of 5 at x = 330 mm (see figure 6.7) so this value should be added to the vertical scale to obtain the "n_{max}-factor".

Figures 6.22 present the spectra for (y/θ) = 0.7 at several boundary layer stations, compared with calculations performed with the van Ingen method and Cosal. Peaks, located around 320, 612.5 and 640 Hz

originate from small differences in tunnel motor RPM at both stations. Because of the relatively small signal to noise ratio at the reference station (x = 330 mm), the observed amplification at downstream stations, will be lower than the actual growth. However, from figures 7.22, the maximum amplification at small x-positions, appears to be stronger than the factors predicted with the van Ingen method and Cosal. Only further downstream, the experimental amplification curve is lower than the one predicted with the van Ingen method, while Cosal gives reasonable agreement. Up to x = 616 mm, all figures demonstrate a narrower experimental frequency band of amplified waves in comparison with the van Ingen method.

Similar conclusions can be drawn from figures 6.23, for $(y/\theta) = 2.8$. Comparison of figures 6.22 with 6.23 at corresponding boundary layer stations (see for instance figure 6.24), shows a tendency of the amplification, determined at the B-maximum in power distributions, to shift to lower frequencies. This shift may possibly be attributed to a most intense presence of subharmonic oscillations at the B-maximum.

7. SOME CONCLUSIONS AND RECOMMENDATIONS

Agreement between experimental mean velocity profiles and the Hartree $\beta = -0.14$ profile appeared good, downstream of about $x = 250$ mm where the effects of the non-Hartree initial region were damped out. Comparison with Bola-2D calculations for the experimental pressure distribution gave excellent correspondence over the whole laminar region except for some small regions close to the wall. These differences may be attributed to local deviations in the experimental pressure gradient not taken into account in calculations.

Linear stability calculations performed with the van Ingen method, compared with Cosal results, showed an overprediction of amplification factors by the first, due to inaccuracies in the stability table.
Measured amplification factors showed good correspondence with calculated results of the van Ingen method and Cosal in a large part of the laminar boundary layer. Unstable modes however, were found in a smaller frequency band than predicted with the van Ingen method.
Power distributions across the boundary layer, at frequency bands corresponding to the most unstable TS-waves, showed three maxima of which only two were obtained from linear stability calculations. The second maximum may be attributed to non-linear effects which seemed to appear much earlier than expected. The distribution shape depended on the frequency band considered, both in the laminar region and a large part of the transition region.
Subharmonic breakdown may have been the path to turbulence in the present experiment. This was indicated by the existence of two humps in power spectra, an additional B- maximum in power distributions and a shift of amplification, determined at the B-maximum, to lower frequencies in amplification spectra, in comparison with spectra reduced at the A-maximum.
The start of spectrum filling initially remained confined to only a part of the boundary layer, downstream soon observed in the whole layer.
Comparison of the present experimental results with non-parallel linear stability- and non-linear stability codes deserves recommendation.

The present experiment demonstrates that despite the early observation of non-linear processes along the test wall, e^n-methods which are based on linear stability theory, may give a reasonable prediction of amplification factors in large part of the laminar boundary layer. Hence, it still seems to be a fairly reliable method for transition prediction in engineering studies provided that the relation between the maximum tolerable amplification factor and the initial disturbances is known. Possibly, only external disturbances which actually take part in the transition process should be included in last-mentioned relation. It is questionable if only external oscillations at TS-frequencies should be considered in these or also at frequencies of secondary modes (e.g. subharmonics).

ACKNOWLEDGEMENT

The author is indebted to his collegues of the scientific, technical and administratieve staff for their support during this work and to ir. A.C. de Bruin of NLR for performing the Bola and Cosal calculations. This work was partially supported by the NLR.

REFERENCES

1. L.M. Mack: Boundary-layer linear stability theory. AGARD-R-709. Special course on stability and transition of laminar flow, 1984.

2. G.B. Schubauer, H.K. Skramstadt: Laminar boundary layer oscillations and transition on a flat plate. NACA Report 909, 1948.

3. J.A. Ross, F.H. Barnes, J.G. Burns, M.A.S. Ross: The flat plate boundary layer, part 3. Comparison of theory with experiment. J. Fluid Mechanics (1970), vol. 43, part 4.

4. H.L. Rogler: The coupling between free stream disturbances, driver oscillations, forced oscillations, and stability waves in a spatial analysis of a boundary layer. AGARD CP 224, laminar-turbulent transition.

5. Yu S. Kachanov, V.V. Kozlov and V.Ya Levchenko: Occurrence of Tollmien-Schlichting waves in the boundary layer under the effect of external perturbations. Fluid Dynamics, 13, (translated from Izvestiya Akademii Nauk SSSR), 1978.

6. P.S. Klebanoff, K.D. Tidstrom, L.M. Sargent: The three dimensional nature of boundary layer instability. Journal of Fluid Mechanics, vol. 9, part 2, 1960.

7. Yu S. Kachanov, V.V. Kozlov, V.Ya Levchenko: Non-linear development of a wave in a boundary layer. Fluid dynamics 12 (translated from Izvestiya Akademii Nauk SSSR), 1978.

8. J.L.. van Ingen: A suggested semi-emperical method for the calculation of the boundary layer transition region. Report VTH-74. Delft University of Technology, 1956.

9. M.R. Malik, S.A. Orszag: Efficient computation of the stability of three dimensional compressible boundary layers, AIAA-81-1277, 1981.

10. M.R. Malik: Finite-difference solution of the compressible stability eigenvalue problem. NASA CR-3584, 1982.

11. A.M. Tjandra: Vergelijking van de locale opslingering van Tollmien-Schlichting golven volgens drie verschillende lineaire stabiliteits berekeningsmethoden (in Dutch). NLR Memorandum AI-88-010 U, 1988.

12. J.L. van Ingen, L.M.M. Boermans, J.J.H. Blom: Low speed airfoil section research at Delft University of Technology. ICAS-80-10.1, 1980.

13. A.R. Wazzan, T.T. Okamura, A.M.O. Smith: Spatial and temporal stability charts for the Falkner-Skan boundary layer profiles. DAC 67086, McDonnel Douglas Corp, 1968.

14. H. Kümmerer: Nümerische Untersuchungen zur Stabilität ebener laminarer Grenzschichtströmungen. Dissertation Technische Hochschule, Stuttgart, 1973.

15. J.L. van Ingen: On the calculation of laminar separation bubbles in two dimensional incompressible flow. AGARD-CP-168: "Flow separation", Göttingen, 1975.

16. J.L. van Ingen: "Transition, pressure gradient, suction, separation and stability theory", Low-speed boundary layer transition workshop II, 1976, Rand Corp., Santa Monica, Calif.

17. L.M. Mack: "On the effect of free stream turbulence on boundary layer transition, Low-speed boundary layer workshop II, 1976, Rand Corp., Santa Monica, Calif.

18. J.P.F. Lindhout, G. Hoek, E. de Boer, B. v.d. Berg: "A method for the calculation of 3D boundary layers on practical wing configurations", Journal of fluids Engineering, vol. 103, 1981.

19. M.R. Malik: "Cosal a black box compressible stability analysis code for transition prediction in three dimensional boundary layers". NASA CR-165925.

20. J.O. Hinze: Turbulence (second edition). McGraw-Hill, New York, 1975.

21. J.D. Vagt: Hot wire probes in low speed flows. Prog. Aerospace Sci., vol. 18, 1979.

22. A.M.O. Smith: Improved solutions of the Falkner and Skan boundary layer equation. Douglas aircraft Company, Inc., no. FF-10, 1954.

23. N. Thrane: The discrete fourier transform and FFT analysers. Bruel & Kjaer Technical Review, no. 1, 1979.

24. M.B. Priestley: Spectral analysis and time series. Volume I, Academic Press, 1981.

25. W.S. Saric, A.H. Nayfeh: Non-parallel stability of boundary layers with pressure gradients and suction. AGARD-CP-224, Laminar Turbulent transition, Lyngby, 1977.

26. D. Arnal: Diagrammes de stabilité des profils de couche limite auto-semblables, en ecoulement bidimensionnel incompressible, sans et avec courant de retour. Rapport Technique OA no. 34/5018, CERT, 1986.

27. H.U. Meier, U. Michel, H.P. Kreplin:The influence of windtunnel turbulence on the boundary layer transition. Perspectives in turbulence studies, symposium, DFVLR, Göttingen, Springer-Verlag, May 1987.

28. U. Michel, E. Froebel: Lower limit for the velocity fluctuation level in windtunnels. Exp. in Fluids 6, 49-54, 1988.

29. Yu S. Kachanov, V.Ya Levchenko: The resonant interaction of disturbances at laminar-turbulent transition in a boundary layer. Journal of Fluid Mechanics 138, 1984.

30. A.D.D. Craik: Non linear resonant instability in boundary layers. Journal of Fluid Mechanics, vol. 50, part 2, 1971.

x (mm)	$\tilde{U}_e/\tilde{U}_{ref}$	x (mm)	$\tilde{U}_e/\tilde{U}_{ref}$	x (mm)	$\tilde{U}_e/\tilde{U}_{ref}$
0	.987	434.3	.931	1050.8	.877
1	.922	450.8	.930	1151.0	.876
2	.909	467.7	.927	1251.2	.886
3	.909	484.1	.926	1351.4	.906
5	.930	501.1	.924	1451.5	.914
10	.974	517.6	.921	1552.0	.923
15	.993	534.2	.920	1651.8	.925
20	1.006	550.6	.918	1751.8	.958
25	1.013	567.8	.917	1851.7	1.013
30	1.017	587.1	.914	1951.8	1.079
40	1.017	601.1	.913		
50	1.015	620.3	.911		
60	1.015	634.5	.910		
70	1.013	650.9	.907		
80	1.011	667.8	.906		
90	1.010	684.0	.904		
100	1.010	701.0	.904		
110	1.009	717.3	.903		
120	1.007	734.3	.901		
130	1.005	750.8	.900		
140	1.002	767.8	.898		
150	1.000	784.3	.897		
		801.1	.896		
150.2	1.000	817.8	.894		
250.8	.966	834.4	.894		
350.1	.946	850.8	.891		
417.3	.935	950.2	.885		

Table 4.1: Experimental velocity distribution

x(mm)	(x/L)	$\bar{U}_e/\bar{U}_{ref}$	$\frac{d(\bar{U}_e/\bar{U}_{ref})}{d(x/L)}$
98	0.0490	1.0100	0.000
100	0.0500	1.0100	-0.160
105	0.0525	1.0096	-0.200
110	0.0550	1.0090	-0.300
115	0.0575	1.0081	-0.400
120	0.0600	1.0070	-0.440
125	0.0625	1.0059	-0.440
130	0.0650	1.0048	-0.440
135	0.0675	1.0037	-0.440
140	0.0700	1.0025	-0.460
145	0.0725	1.0013	-0.480

For $x \geq 150$ mm:

$$\frac{\bar{U}_e}{\bar{U}_{ref}} = \left(\frac{x}{x_{ref}}\right)^{\frac{\beta}{2-\beta}}$$

$$\frac{d(\bar{U}_e/\bar{U}_{ref})}{d(x/L)} = \left(\frac{\beta}{2-\beta}\right)\left(\frac{L}{x_{ref}}\right)\left(\frac{x}{x_{ref}}\right)^{\frac{2(\beta-1)}{(2-\beta)}}$$

with x_{ref} = 150.2 mm, L = 2000 mm and β = -0.14.

Table 4.2 : Velocity distribution used in calculations

x (mm)	Filename (mean velocity profile)	Filename spectra	Δy	series
98[1]	&LMEA7	-	0.010	-
98[2]	&LMEA8	-	-0.042	-
98[3]	&LMA35	&LS098	-0.034	2
155[1]	&LMEA9	-	-0.010	-
155[2]	&LMA20	&LS155	-0.010	1
172	&LMA11	-	-0.008	-
189	&LMA12	-	-0.042	-
206	&LMA10	-	-0.105	-
222	&LMA28	&LS222	0.035	2
276	&LMA25	&LS276	0.005	2
330[1]	&LMA19	&LS301	-0.007	1
330[2]	&LMA24	&LS302	0.006	2
396[1]	&LMA22	-	0.030	-
396[2]	&LMA26	&LS396	-0.060	2
413	&LMA23	-	0.016	-
430	&LMA27	&LS430	-0.060	2
458	&LMA18	&LS458	-0.059	1
518	&LMA29	&LS518	0.060	2
568	&LMA17	&LS568	-0.077	1
616	&LMA36	&LS616	-0.033	2
673	&LMA15	&LS673	-0.071	1
709	&LMA30	&LS709	0.082	2
741[1]	&LMA13	-	-	-
741[2]	&LMA14	&LS741	-	1
804	&LMA31	&LS804	-	2
854	&LMA21	&LS854	-	1
872	&LMA32	&LS872	-	2
931	&LMA33	&LS931	-	2
966	&LMA34	&LS966	-	2

Table 6.1: Uncorrected mean velocity profiles. Δy is the correction obtained from the Bola correction procedure ($y_{cor} = y + \Delta y$).

x (mm)	δ^* (mm)	θ (mm)	H
98*	.644	.242	2.661
155*	.853	.313	2.725
172	.923	.329	2.805
189	1.030	.347	2.968
206	1.153	.370	3.116
222	1.071	.382	2.804
276	1.289	.435	2.963
330*	1.455	.498	2.922
396*	1.634	.537	3.043
413	1.638	.541	3.028
430	1.762	.582	3.027
458	1.833	.612	2.995
518	1.845	.626	2.947
568	2.099	.686	3.060
616	2.177	.738	2.950
673	2.301	.760	3.028
709	2.201	.746	2.950
741*	2.225	.798	2.788
804	2.172	.934	2.325
854	1.859	1.017	1.828
872	1.718	1.074	1.599
931	1.844	1.220	1.511
966	1.964	1.330	1.477

* Average of more realizations

Table 6.2: Boundary layer parameters of uncorrected mean velocity profiles.

x (mm)	δ^* (mm)	θ (mm)	H	δ_{99}/θ
98*	.623	.241	2.585	7.299
155*	.843	.321	2.702	7.412
172	.915	.328	2.790	7.317
189	.988	.347	2.847	7.476
206	1.049	.368	2.851	7.459
222	1.105	.383	2.885	7.415
276	1.294	.435	2.975	7.531
330*	1.455	.497	2.928	7.436
396*	1.619	.536	3.021	7.402
413	1.654	.542	3.052	7.362
430	1.702	.581	2.929	7.284
458	1.775	.612	2.900	7.240
518	1.904	.627	3.037	7.464
569	2.022	.685	2.952	7.448
616	2.144	.738	2.905	7.575
673	2.230	.759	2.938	7.373
709	2.282	.746	3.059	7.564
741*	2.225	.798	2.788	6.924
804	2.172	.934	2.325	6.772
854	1.859	1.017	1.828	7.174
872	1.718	1.074	1.600	8.170
931	1.844	1.220	1.511	8.984
966	1.964	1.330	1.477	8.464

* Average of more realizations

Table 6.3: Boundary layer parameters of corrected mean velocity profiles δ_{99}/θ = 7.37 for Hartree β = -0.14 flow.

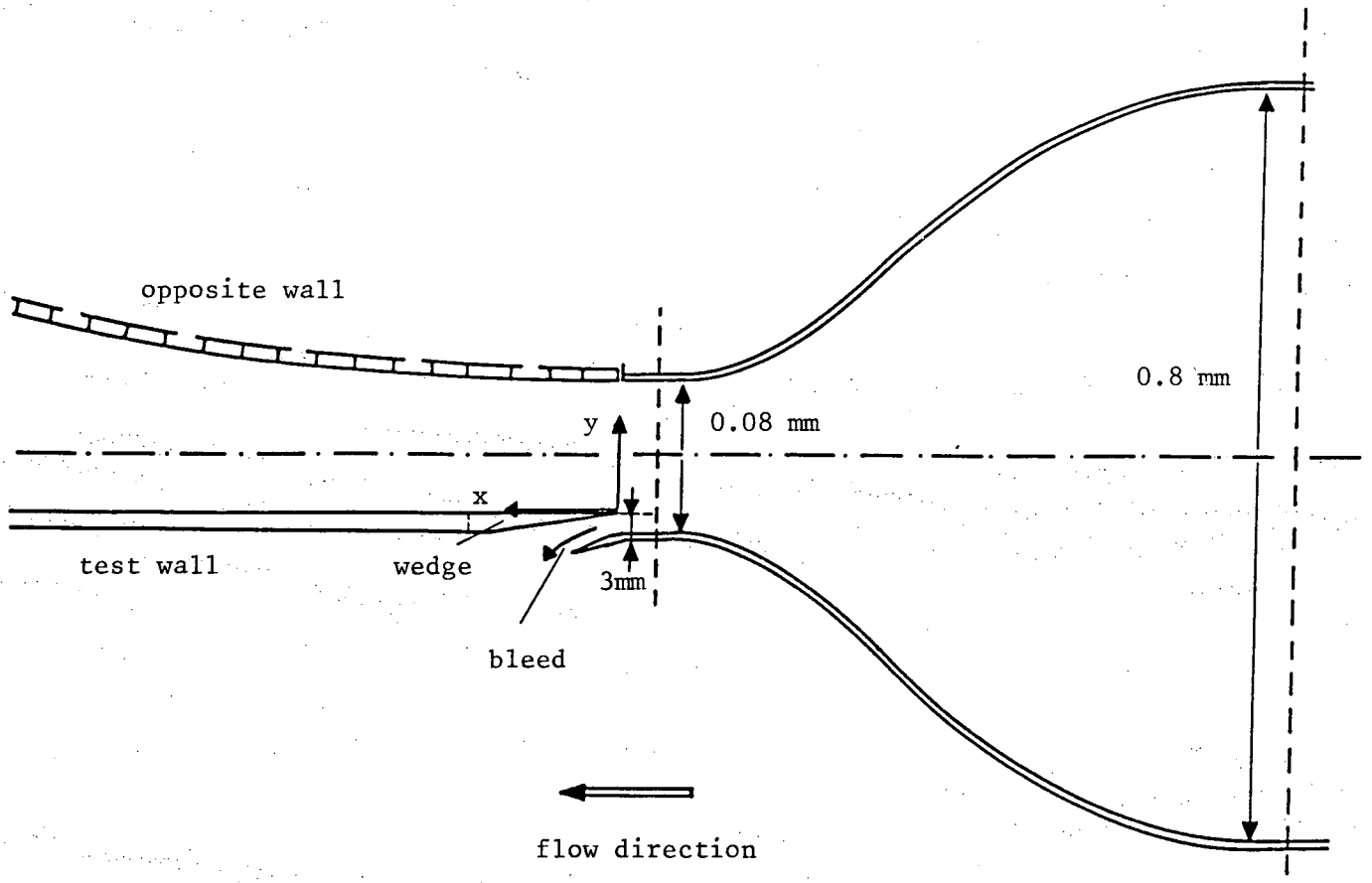

Figure 3.1 : Top view of longitudinal cross section of contraction and test section.

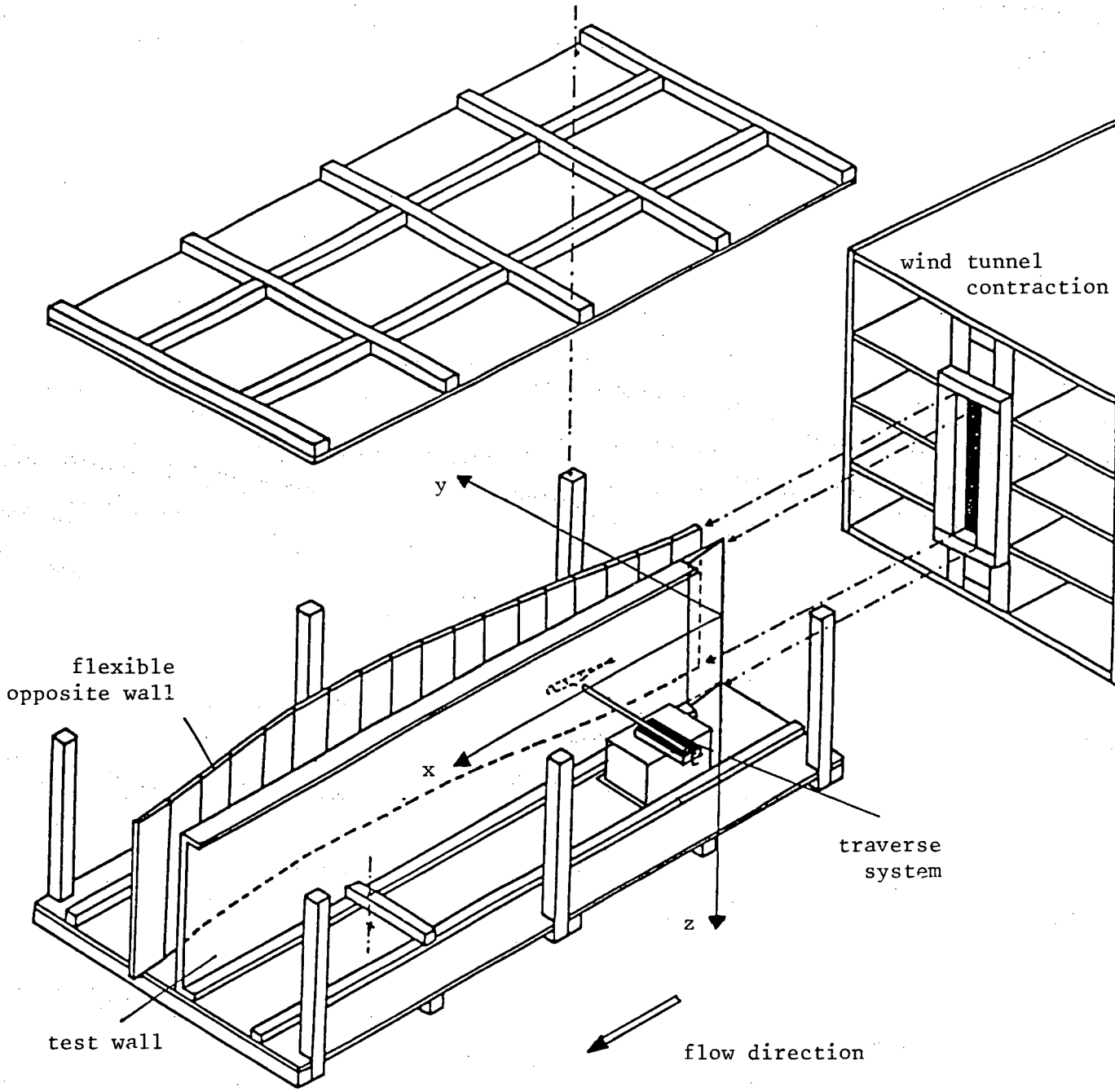

Figure 3.2 : Exploded view of test section and location of coordinate axes.

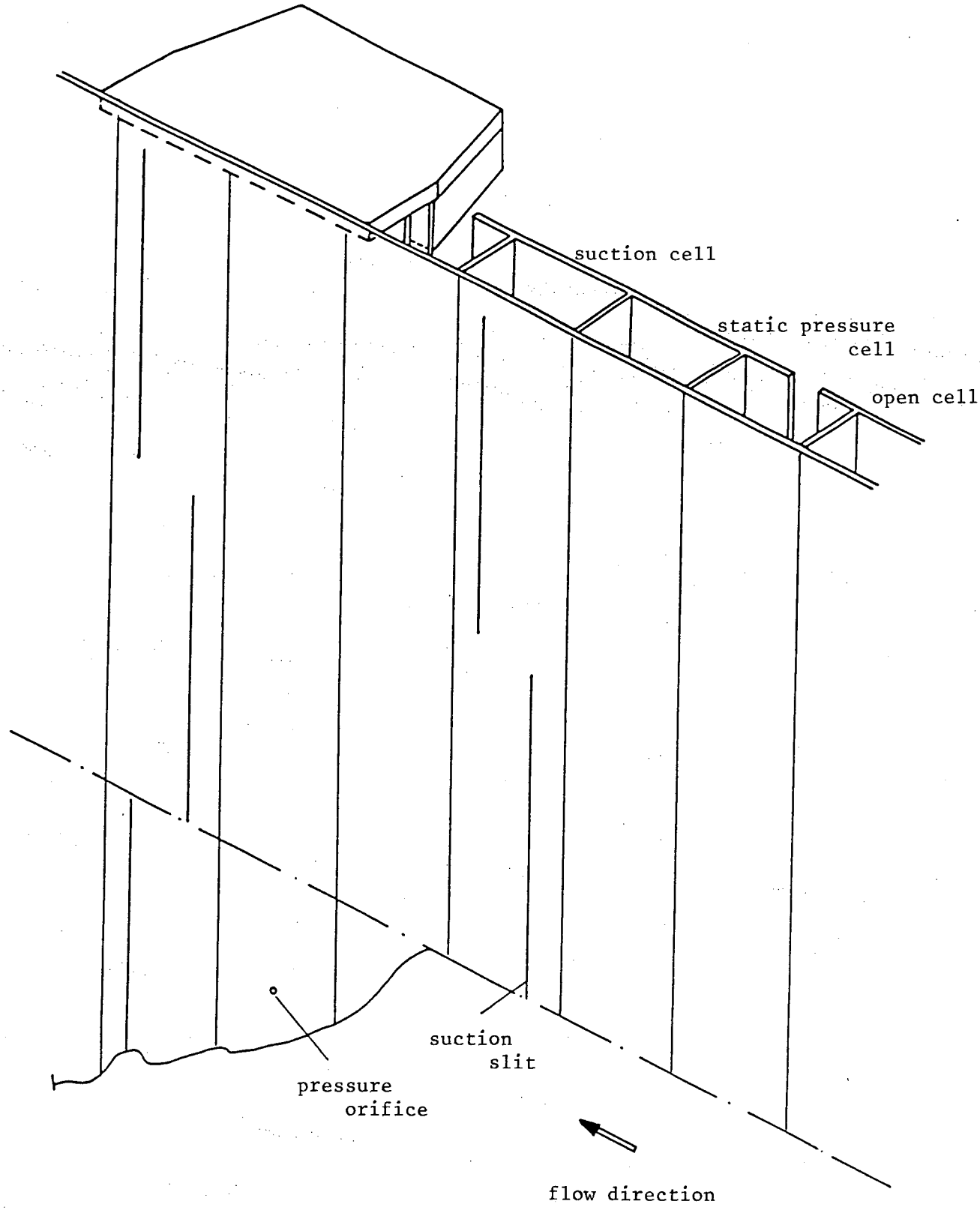

Figure 3.3 : Construction of the flexible opposite wall.

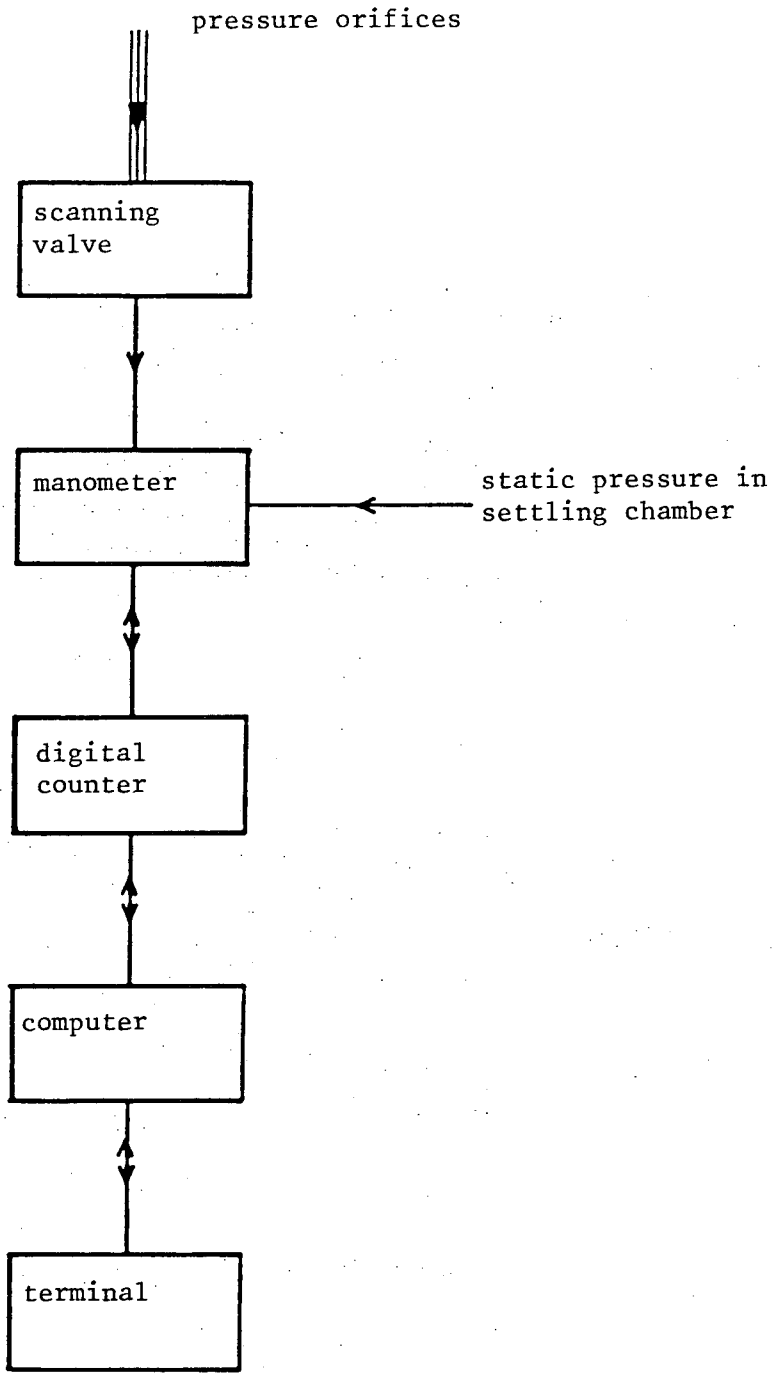

Figure 3.4 : Test set-up for pressure measurements.

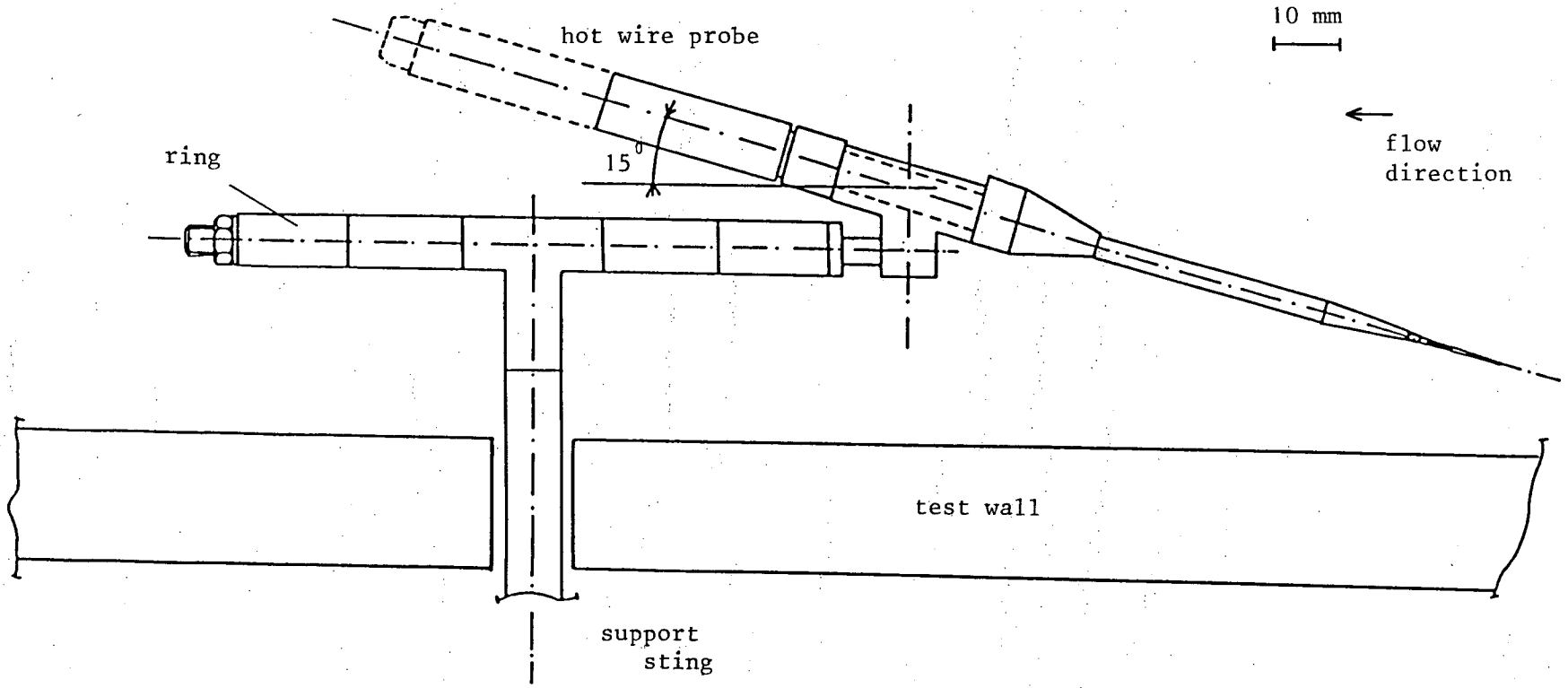

Figure 3.5 : Hot wire probe and connection to support sting.

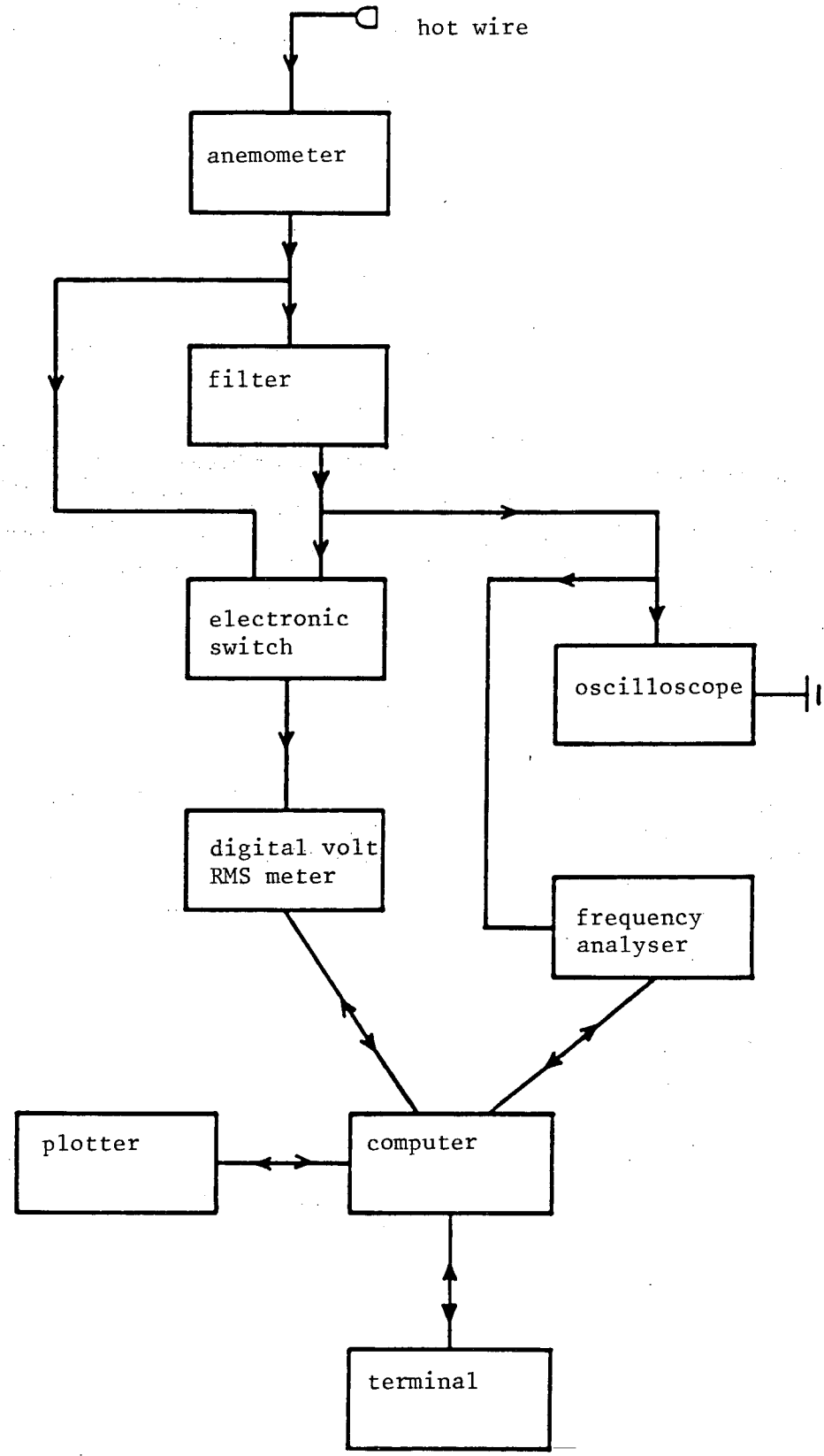

Figure 3.6 : Test set-up for hot wire measurements.

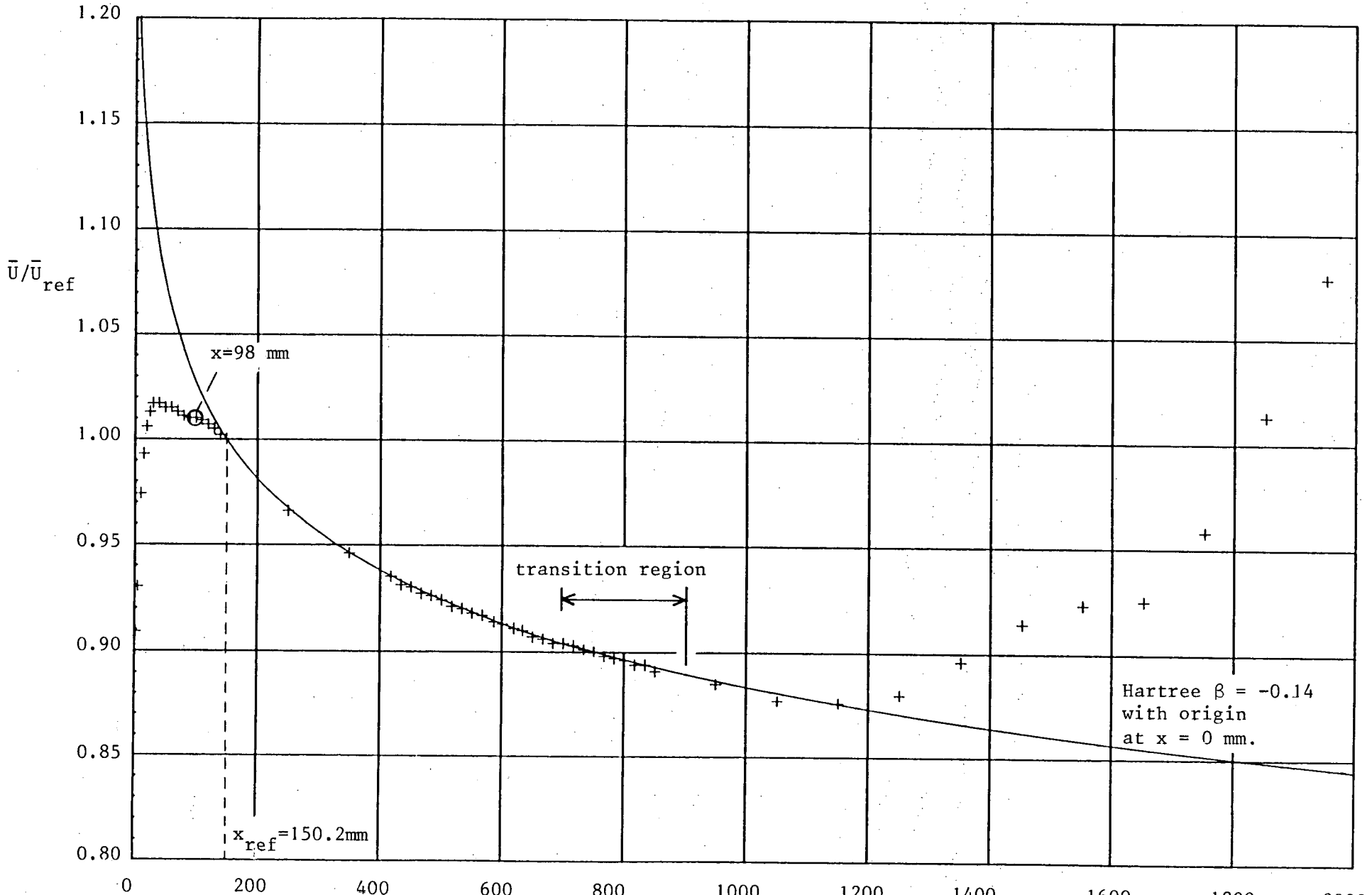

Figure 4.1 : Theoretical (-) and experimental (+) velocity distribution, Hartree β = -0.14.

$T_0 = 23.9\ ^0C$

$E_0 = 1.523\ V$

$n = 0.492$

$$f(\hat{E}) = 0.0958\ \hat{E}^3 - 0.1314\ \hat{E}^2 + 1.0360\ \hat{E}$$

Figure 5.1 : Calibration curve and -points.

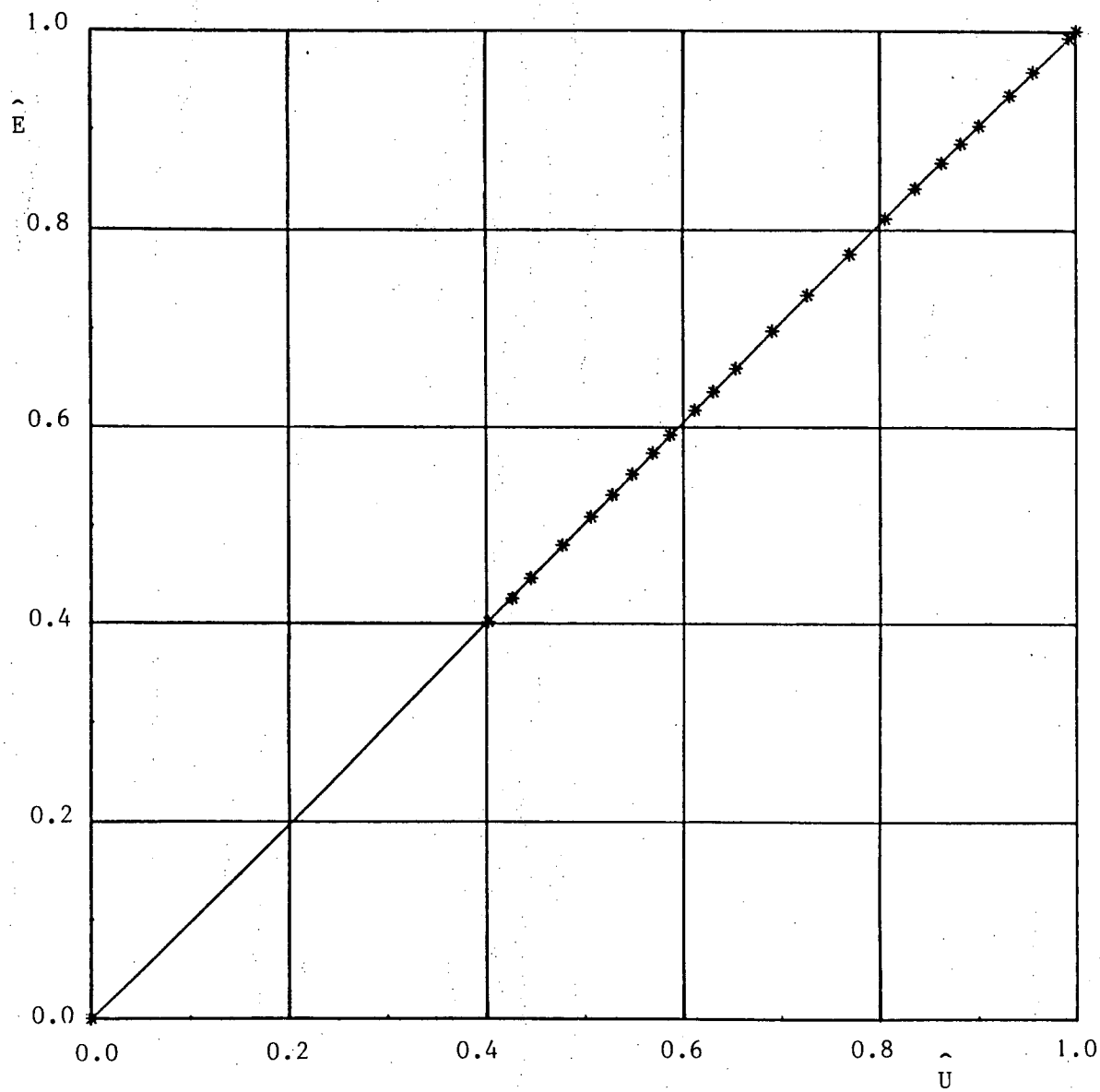

T_0 = 23.9 ^{0}C

E_0 = 1.523 V

n = 0.492

$24.9 \leqslant T \leqslant 25.5$ ^{0}C

$23.5 \leqslant T \leqslant 24.1$ ^{0}C

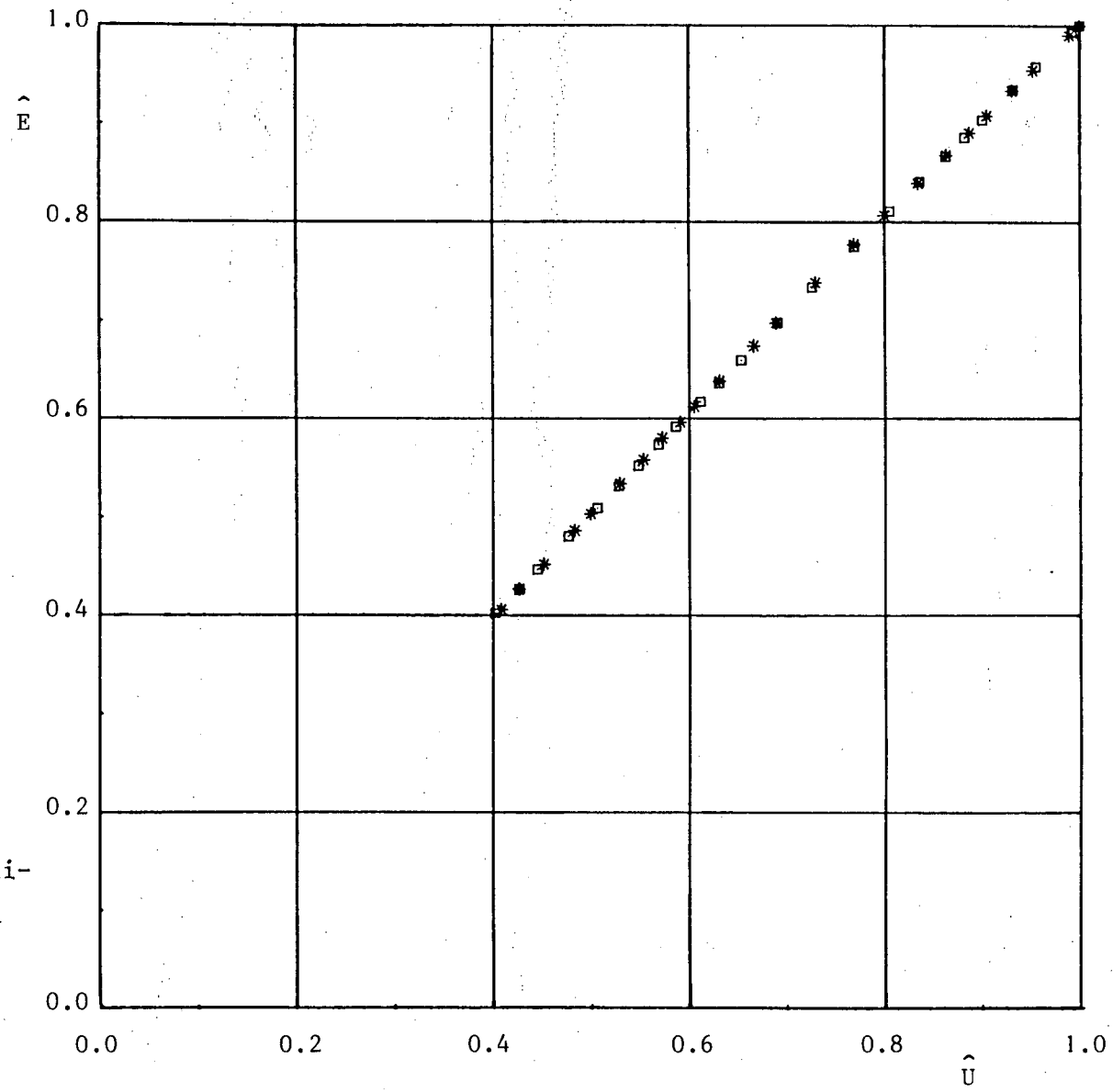

Figure 5.2 : Comparison of two calibrations reduced with the same constants.

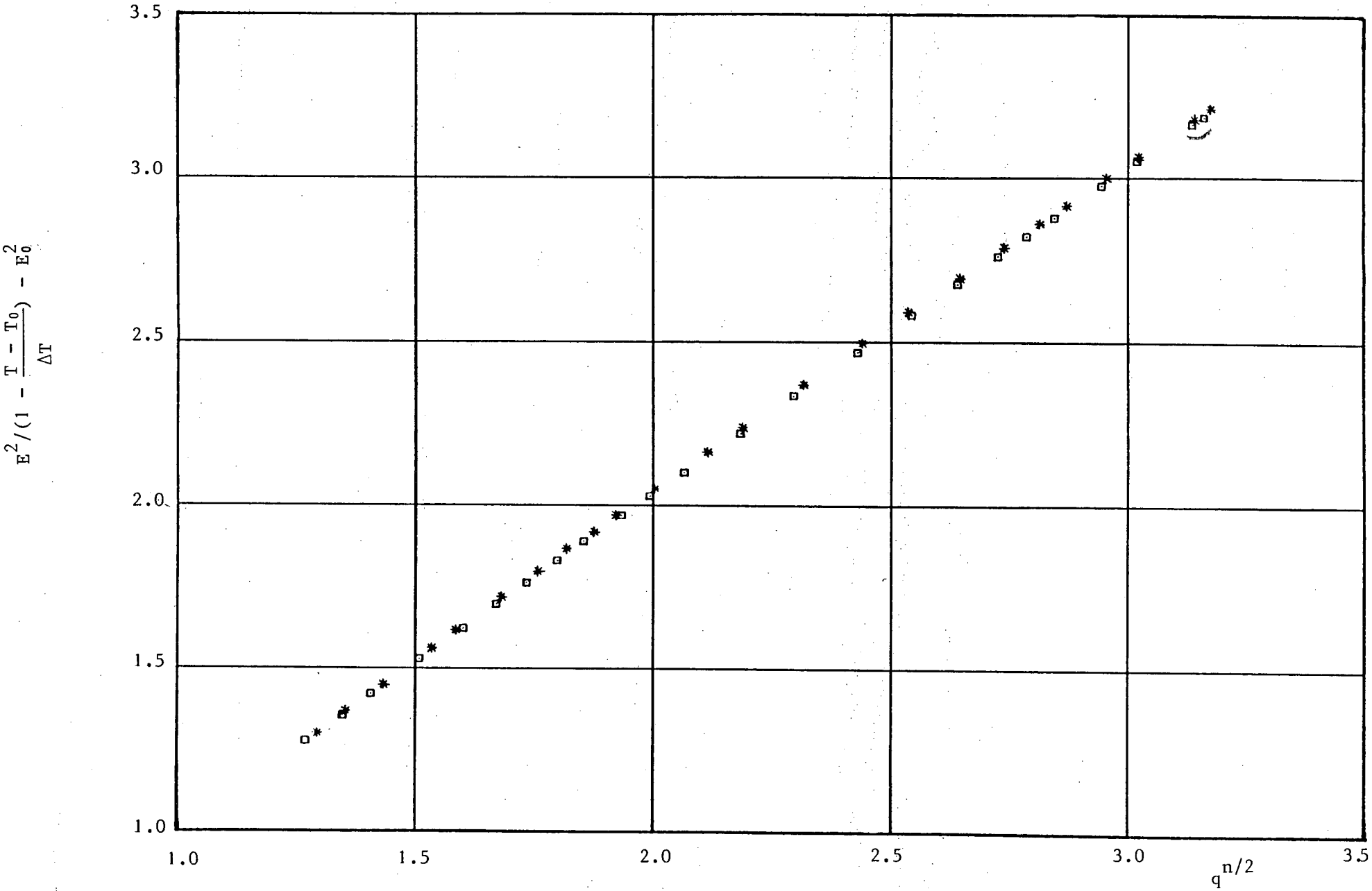

Figure 5.3 : Comparison of two calibrations reduced with the same constants (presented in dimensional form).

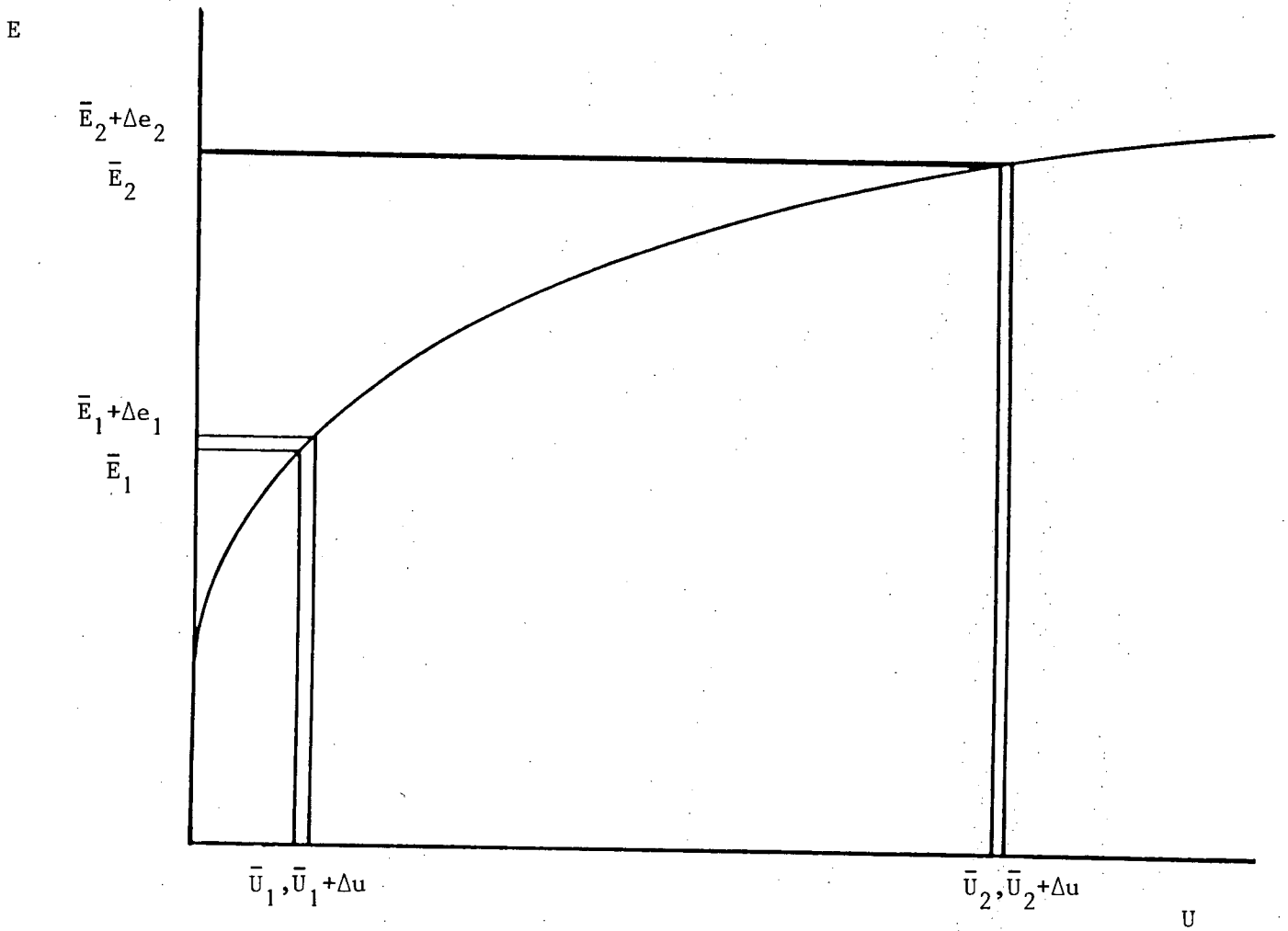

Figure 5.4 : Schematic relation between anemometer output and velocity.

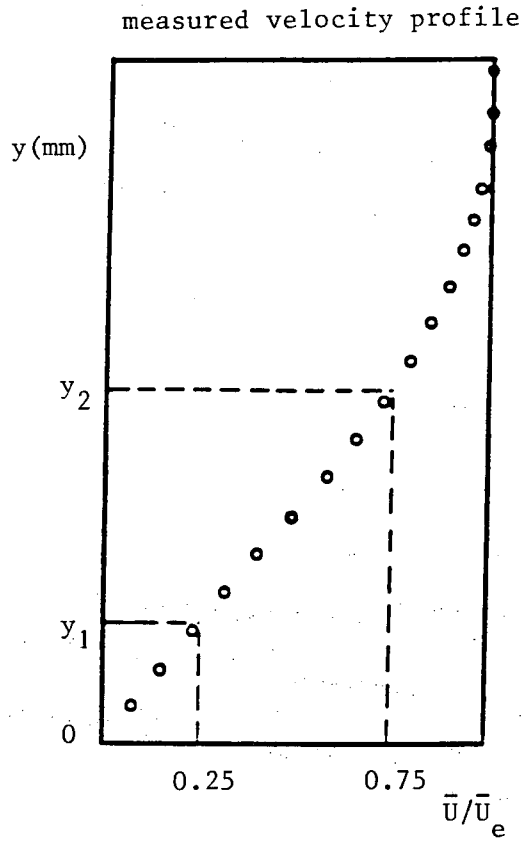

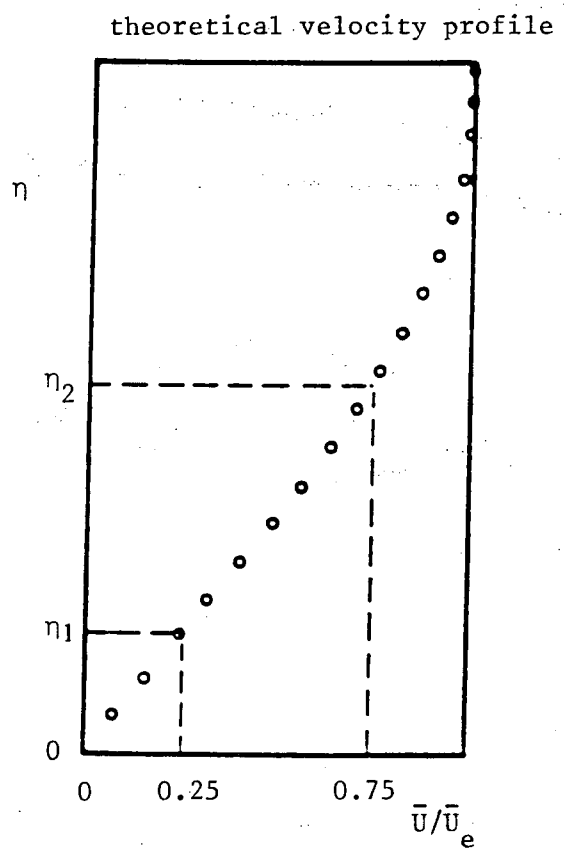

Figure 5.5 : Lagrange interpolation in the experimental and theoretical mean velocity profile.

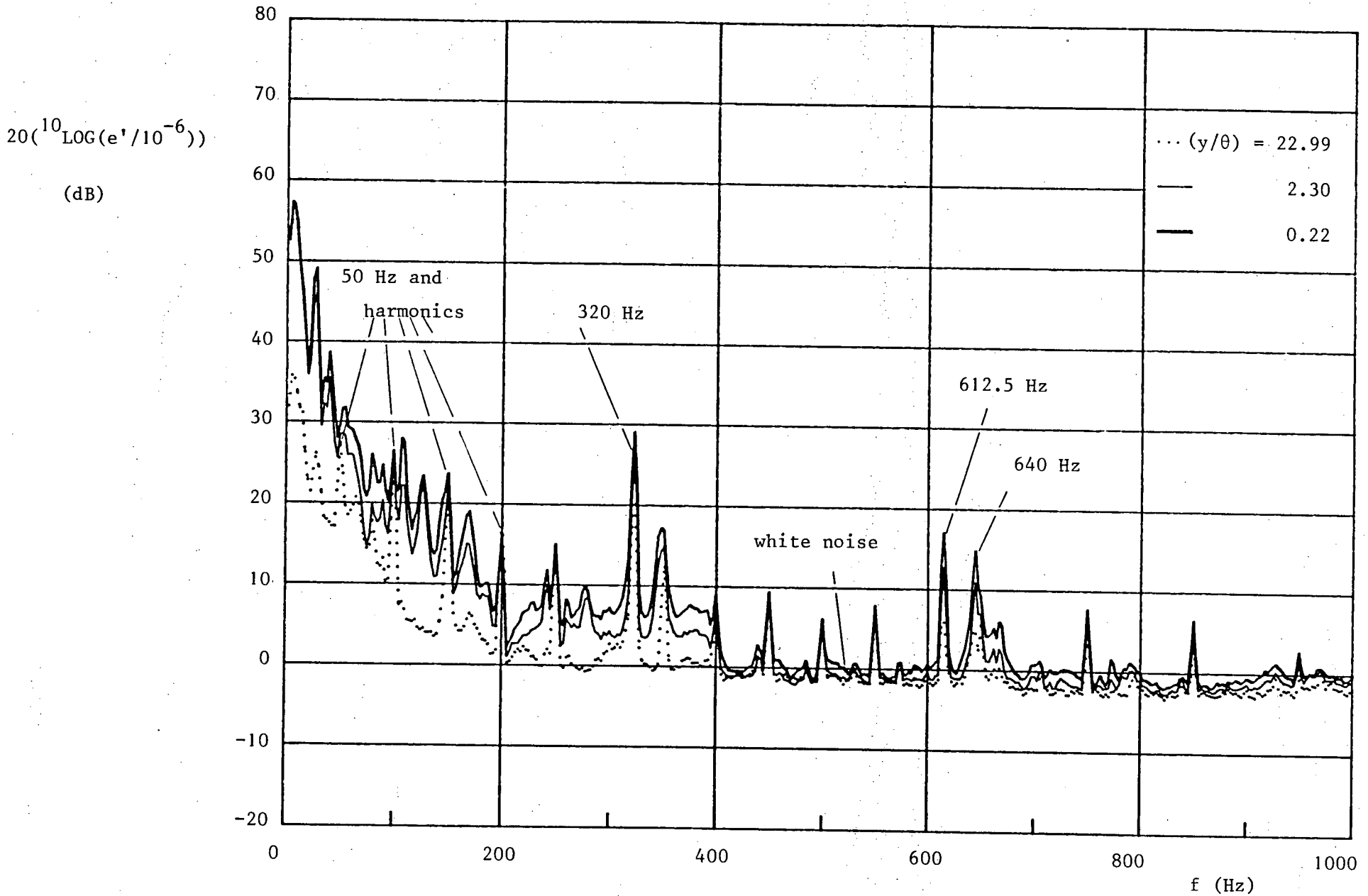

Figure 5.6 : Voltage power spectra at three levels across the boundary layer, x = 276 mm.

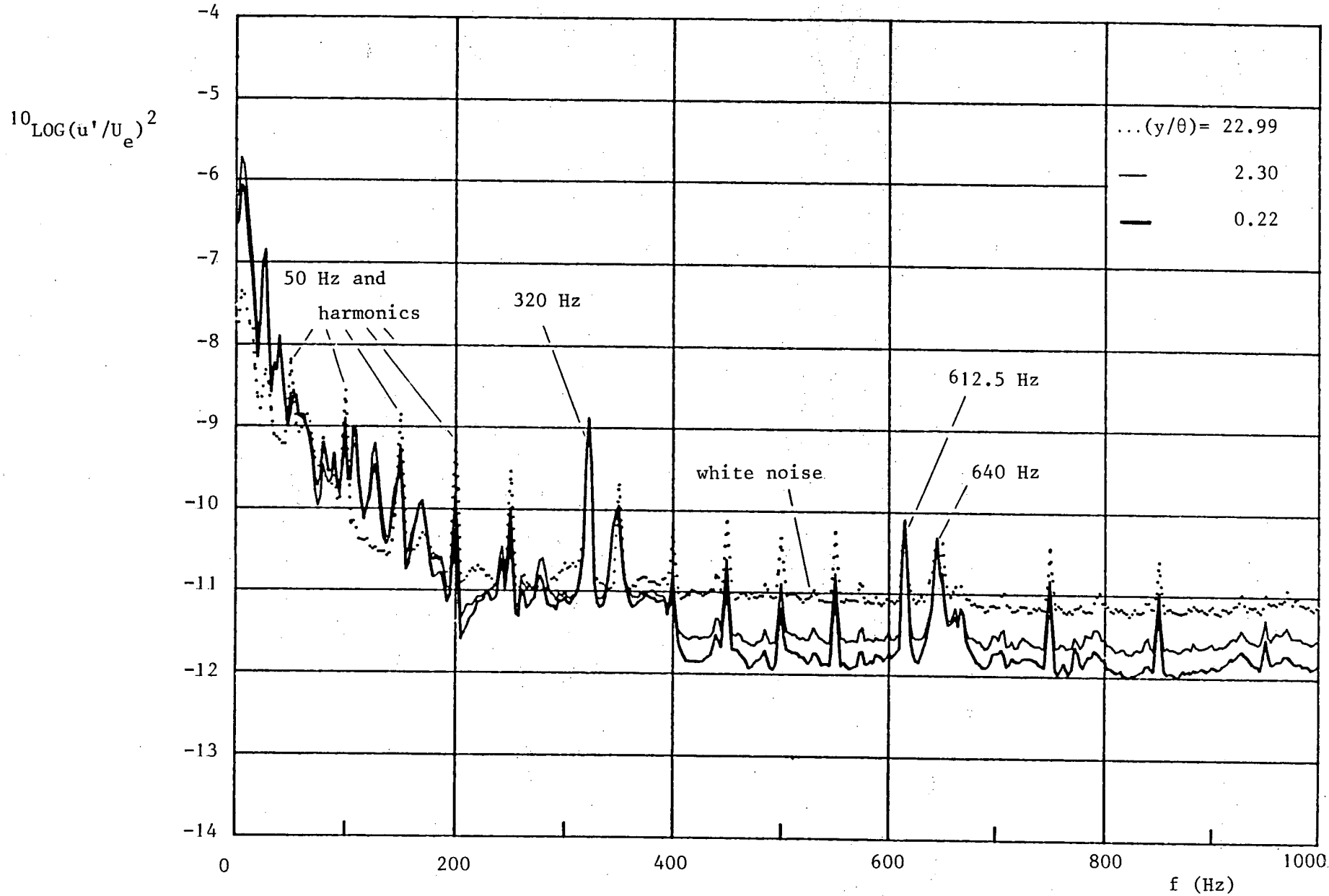

Figure 5.7 : Velocity power spectra at three levels across the boundary layer, x = 276 mm.

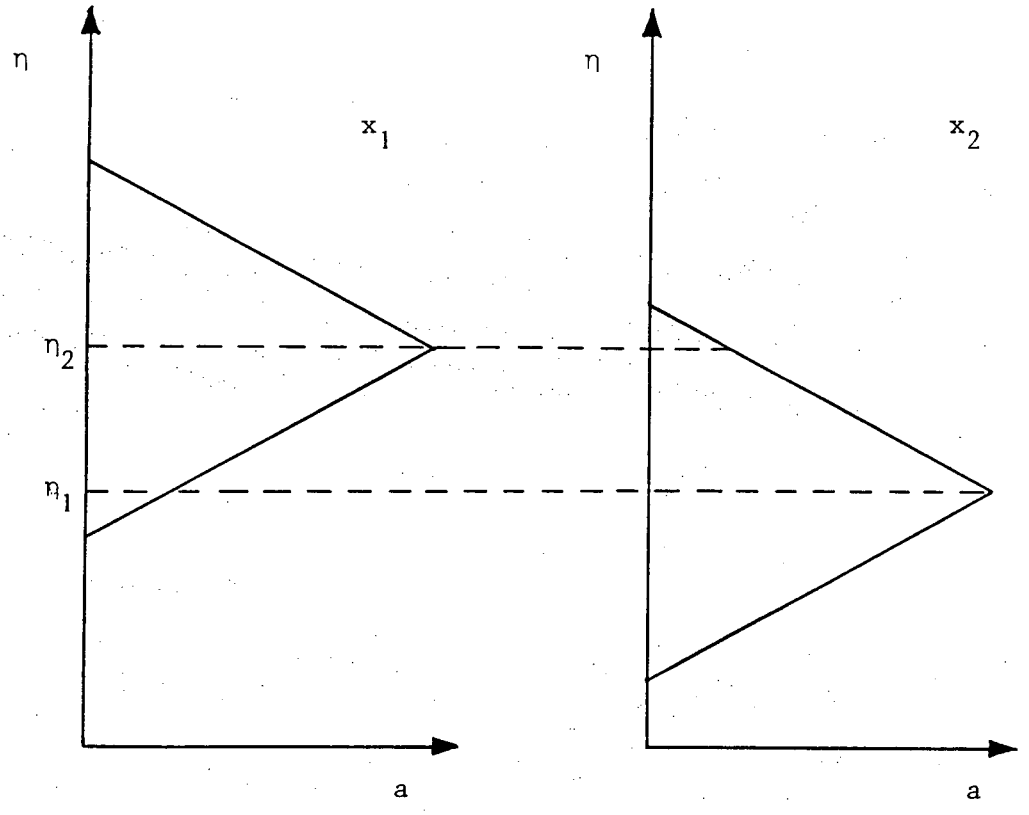

Figure 5.8 : Schematic development of amplitude distribution ($x_2 > x_1$)

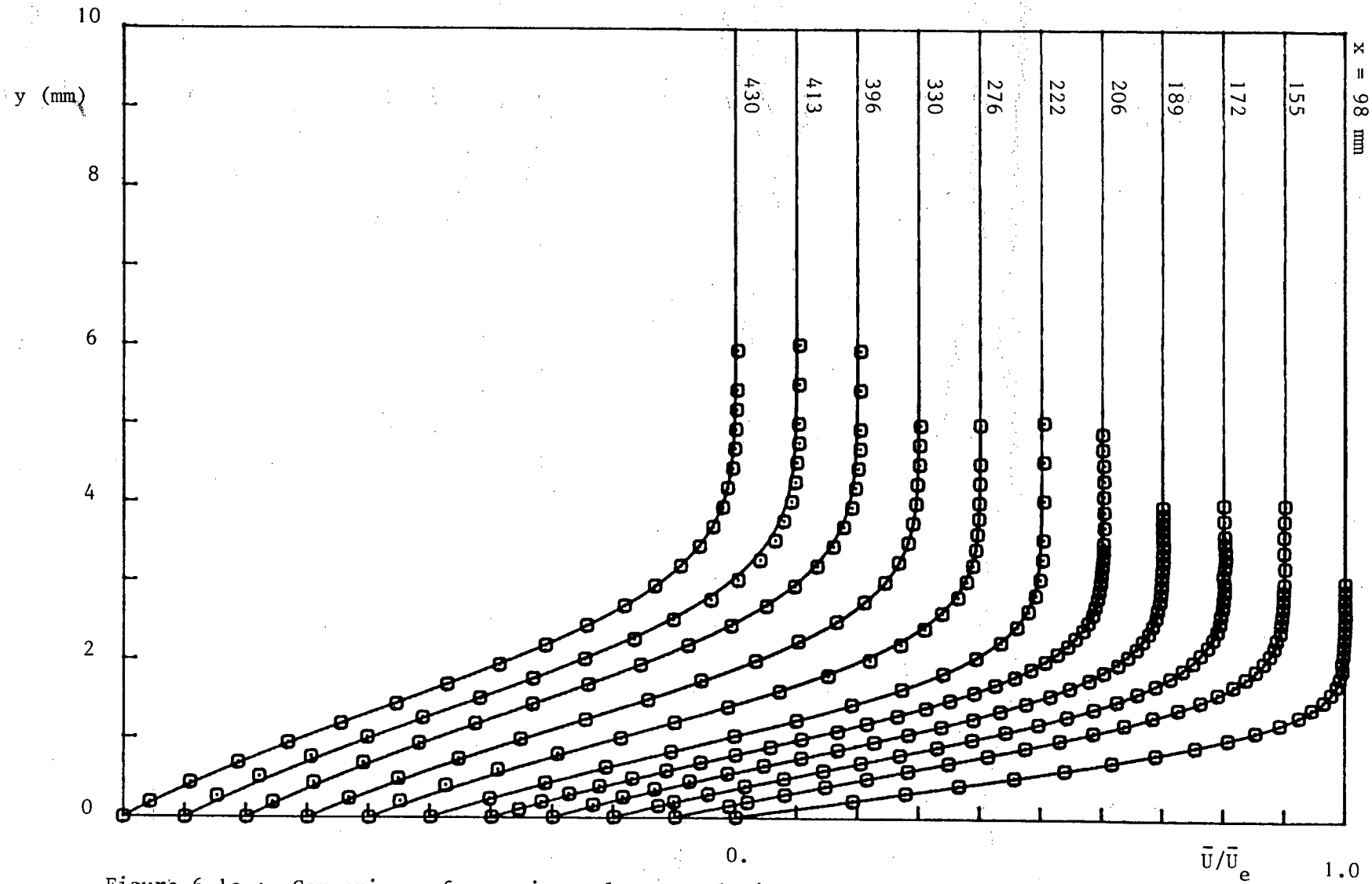

Figure 6.1a : Comparison of experimental mean velocity profiles (⊙) with Bola calculations (—).

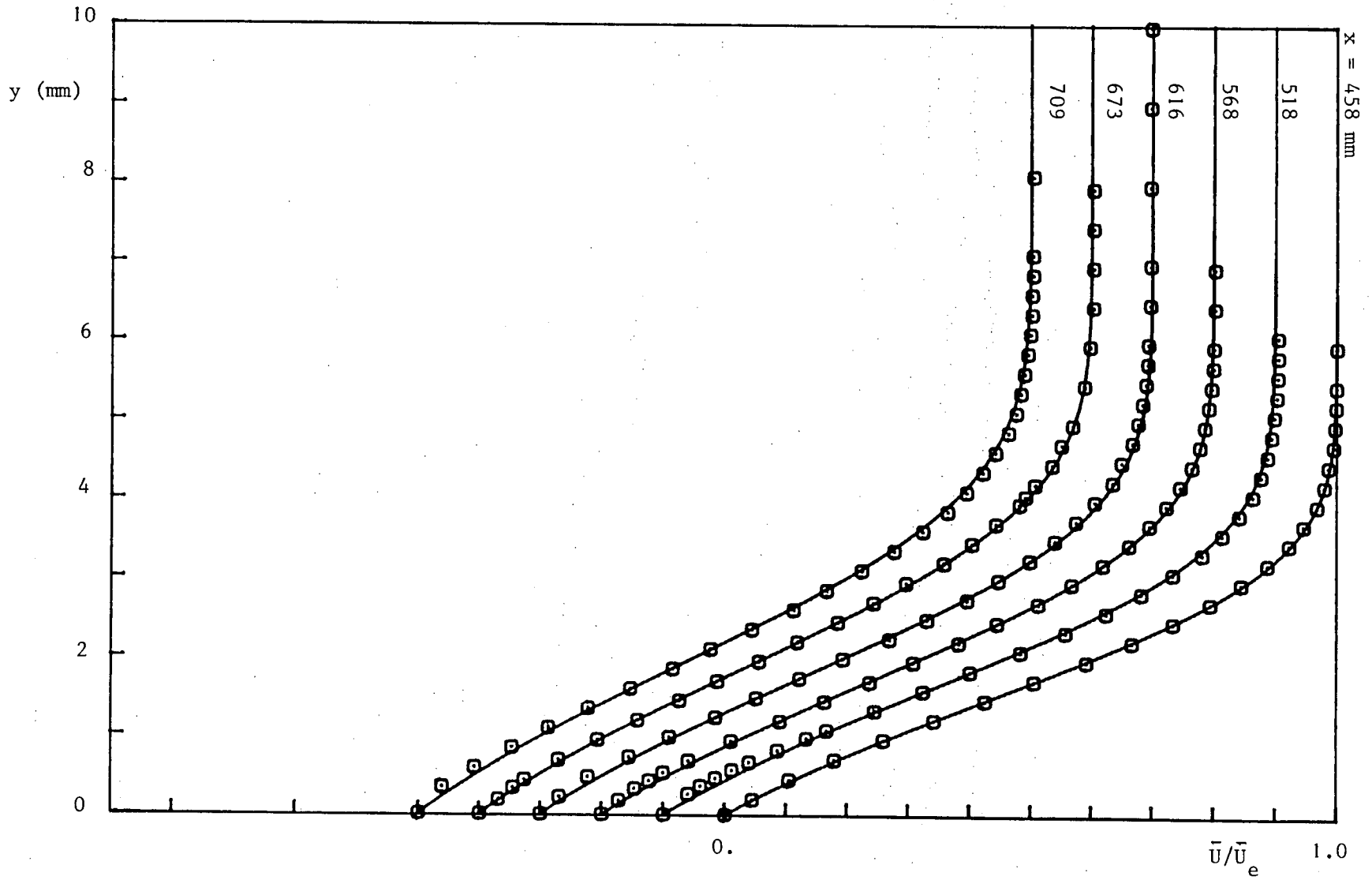

Figure 6.1b : Continued.

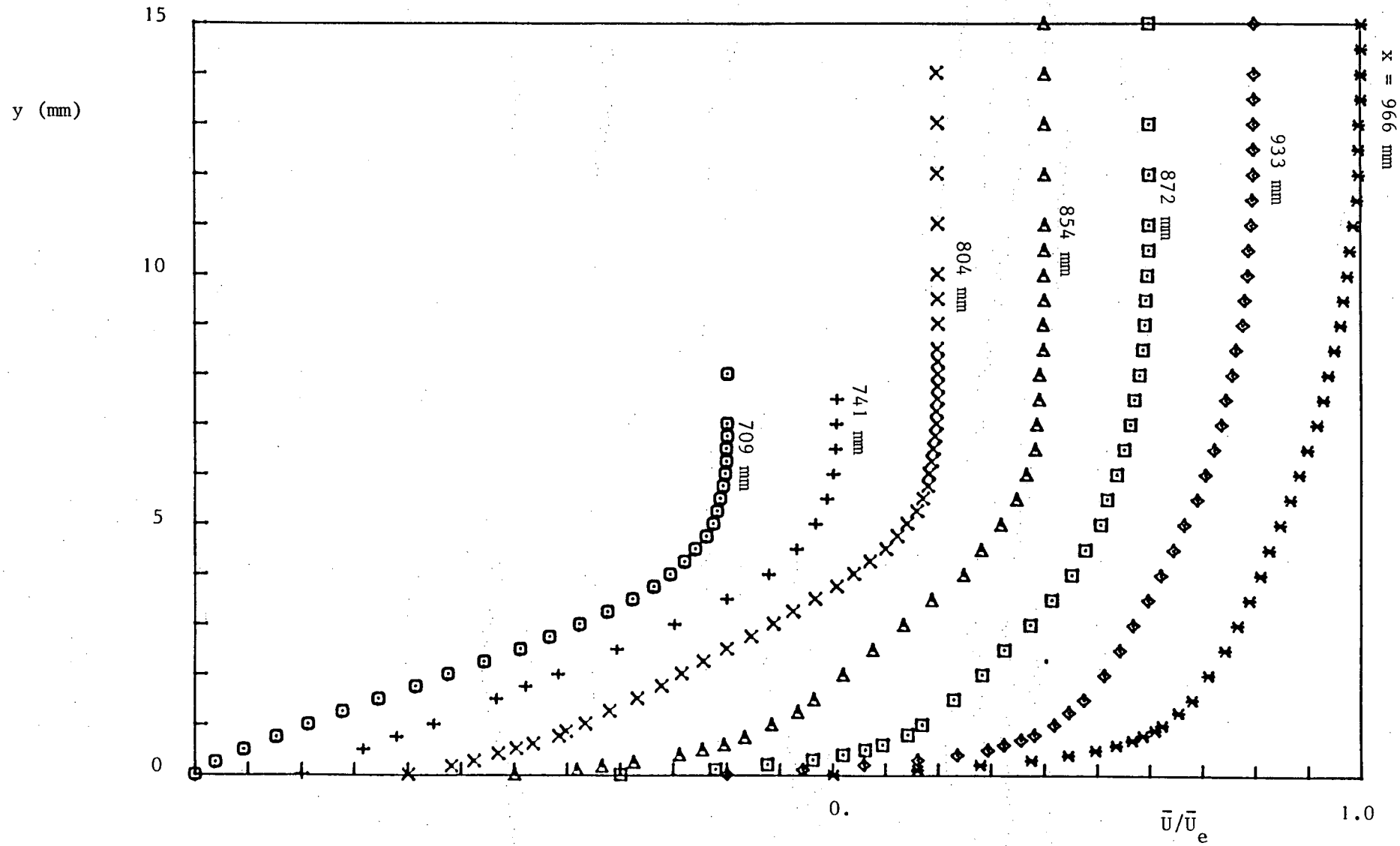

Figure 6.1c : Mean velocity profiles in the transition region.

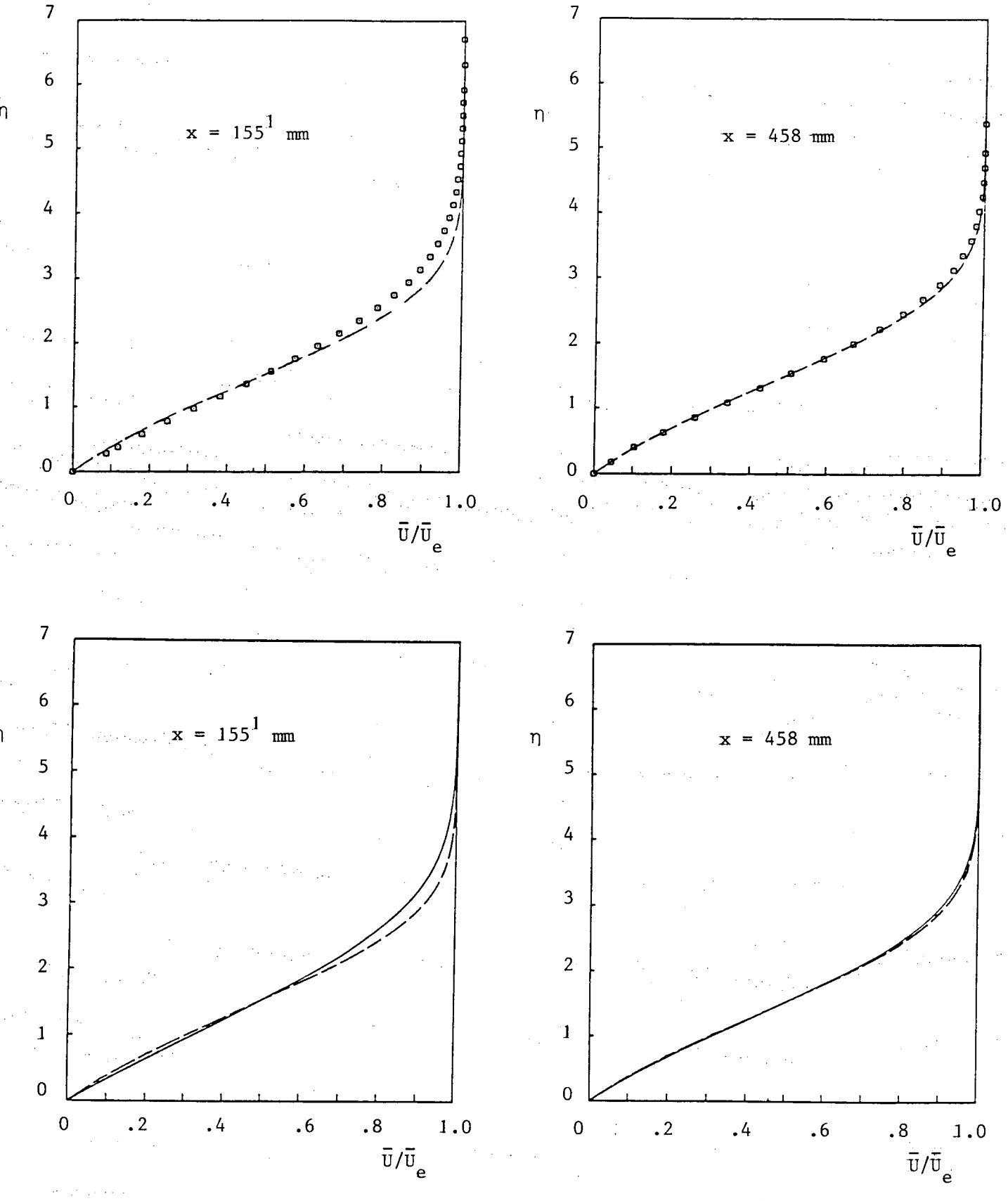

Figure 6.2 : Velocity profiles at two streamwise stations compared with Hartree β=-0.14 profile. (⊙) experiment, (—) Bola, (-·-) Hartree.

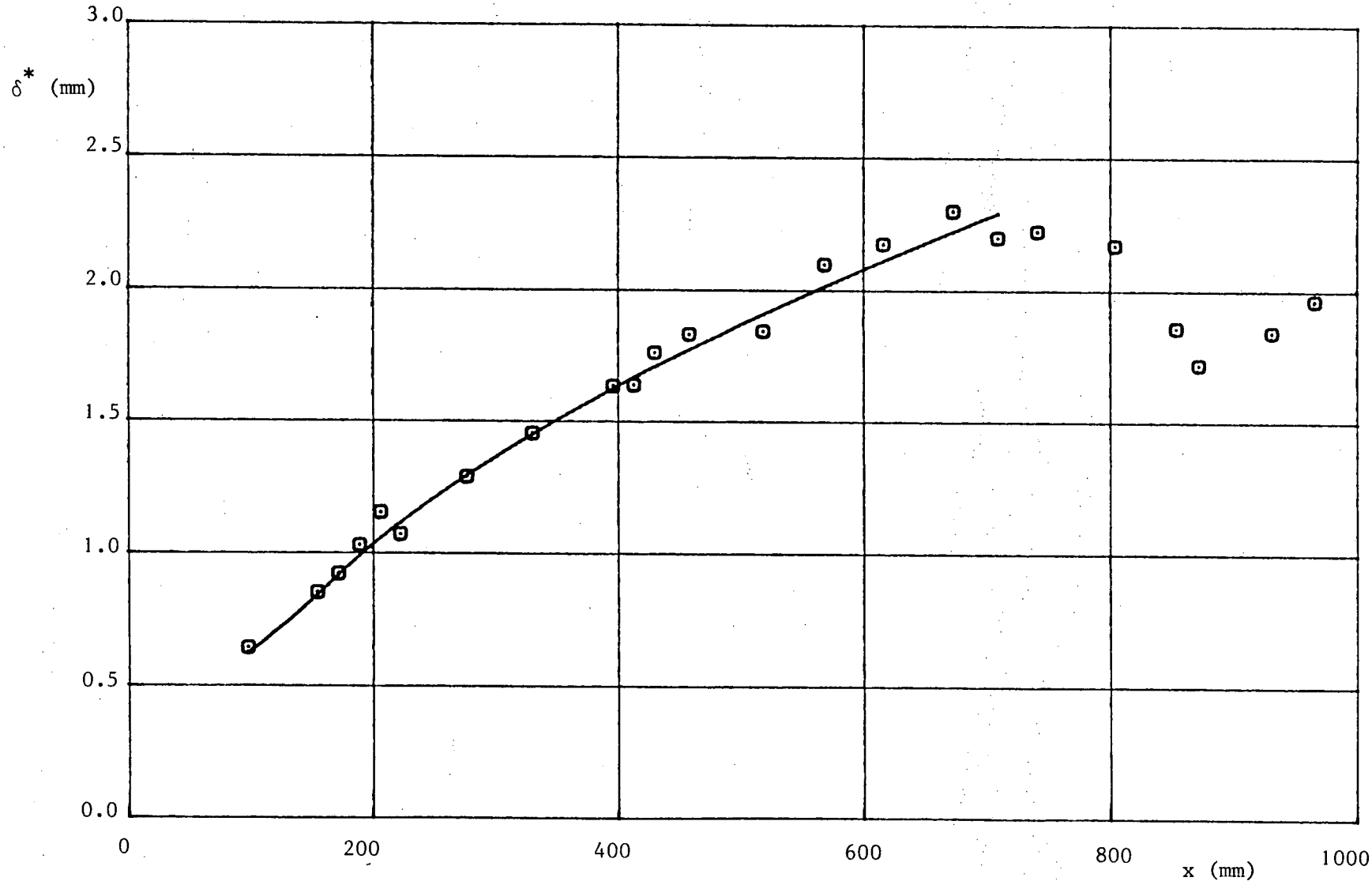

Figure 6.3a : Distribution of displacement thickness. (—) Bola results, (⊙) experiments (uncorrected wall distance).

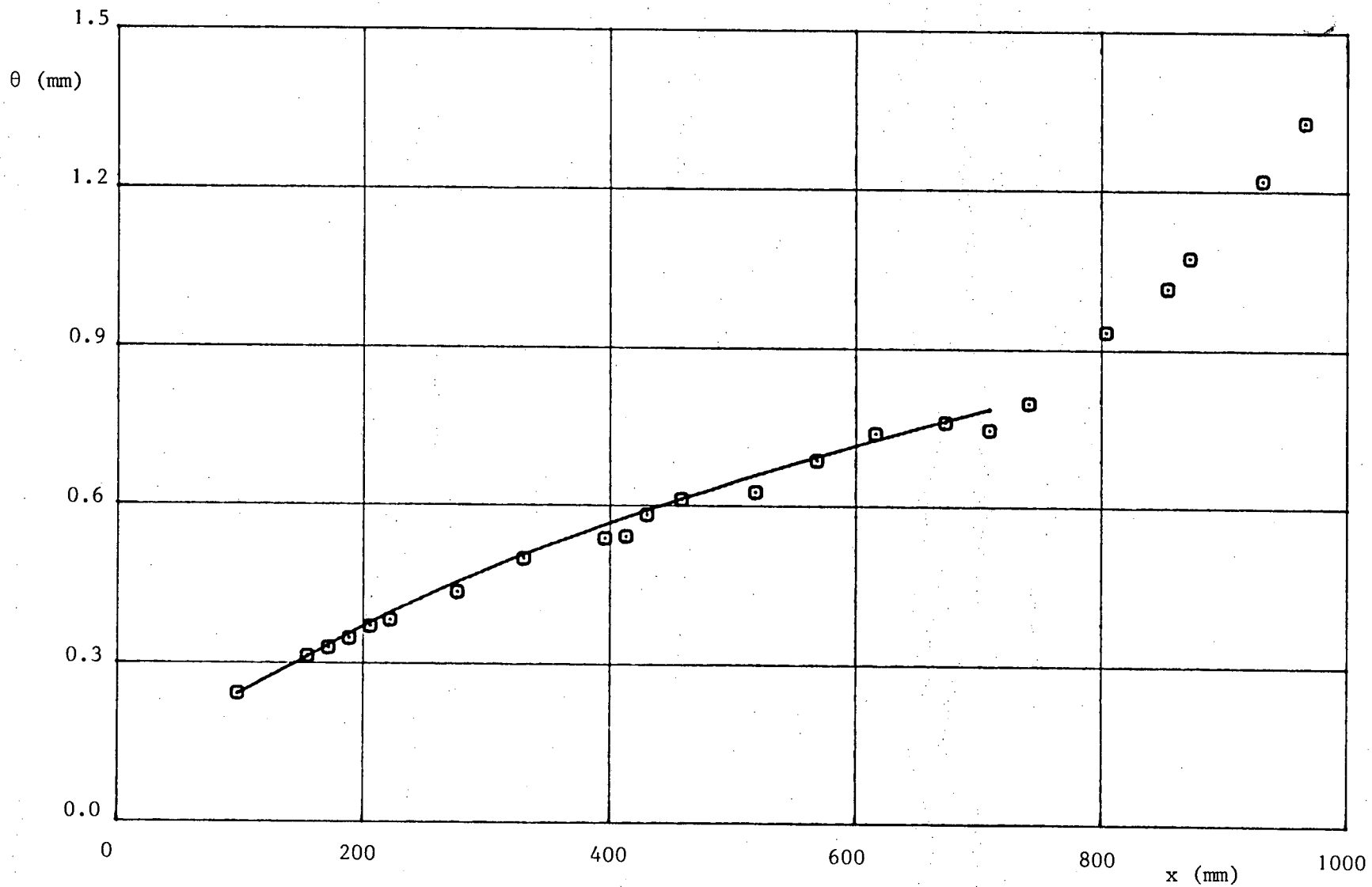

Figure 6.3b : Distribution of momentum thickness. (—) Bola results, (⊙) experiments (uncorrected wall distance).

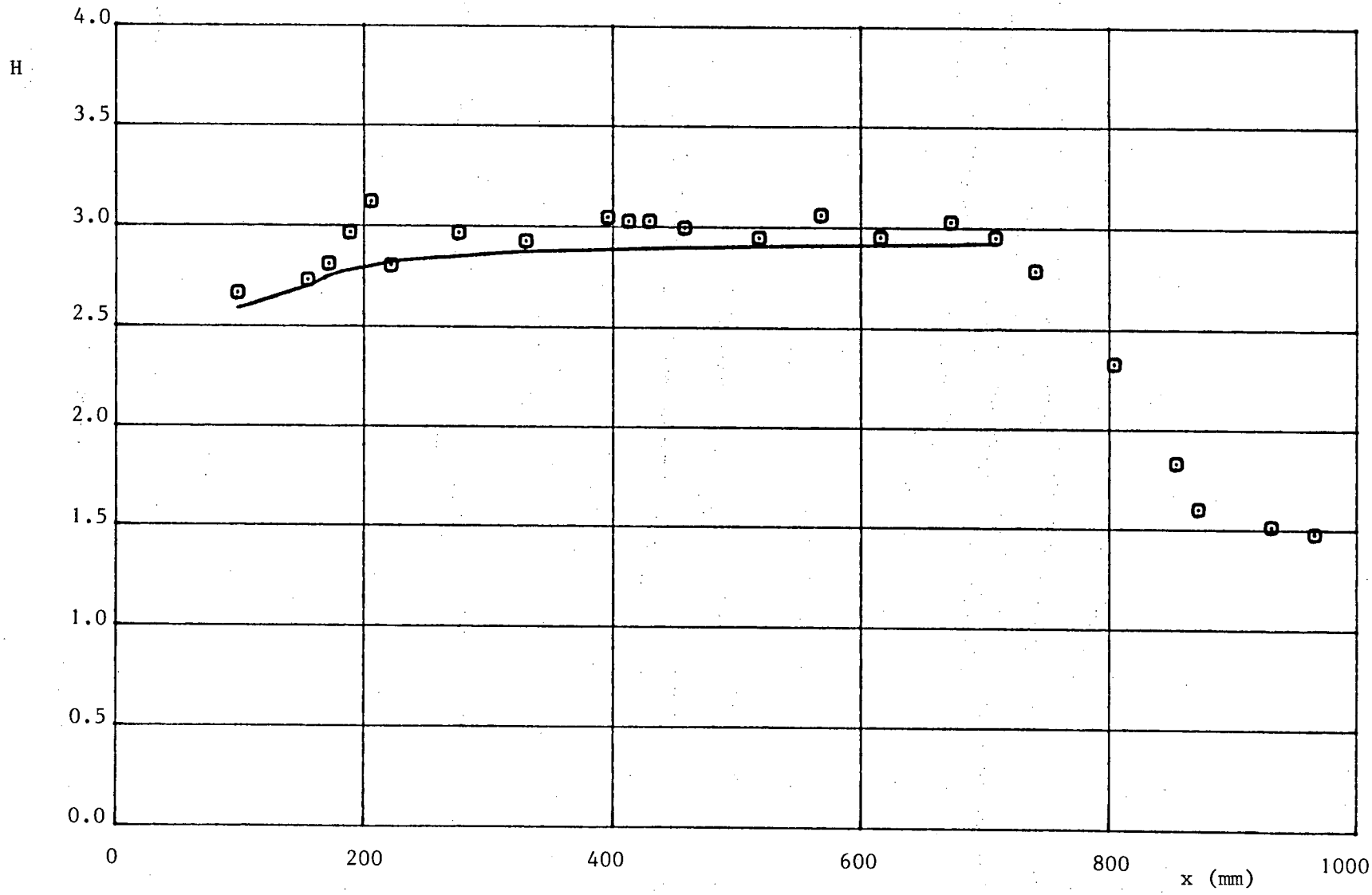

Figure 6.3c : Distribution of shape factor. (—) Bola results, (⊙) experiments (uncorrected wall distance).

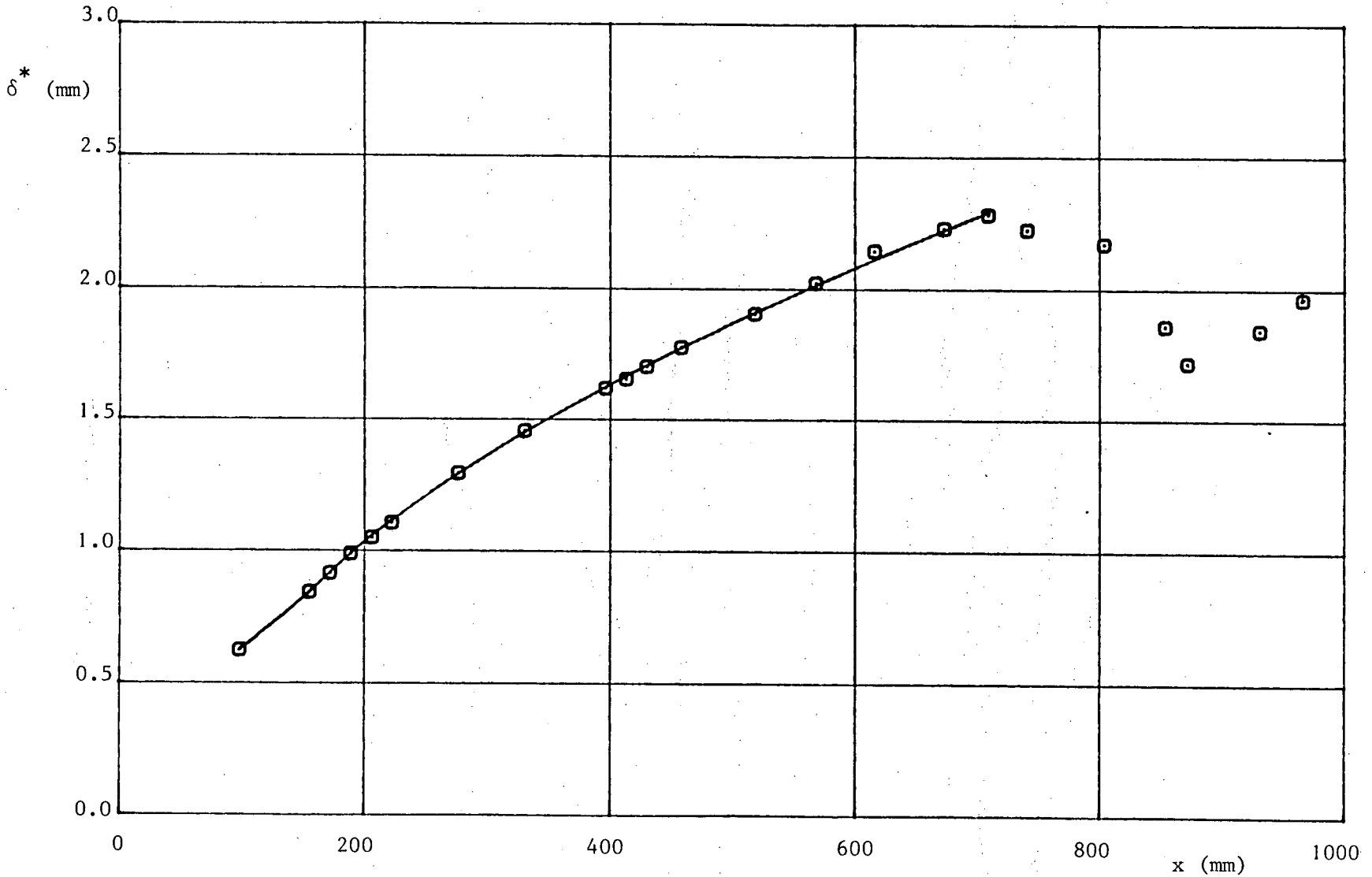

Figure 6.4a : Distribution of displacement thickness. (—) Bola results, (⊙) experiments (corrected wall distance).

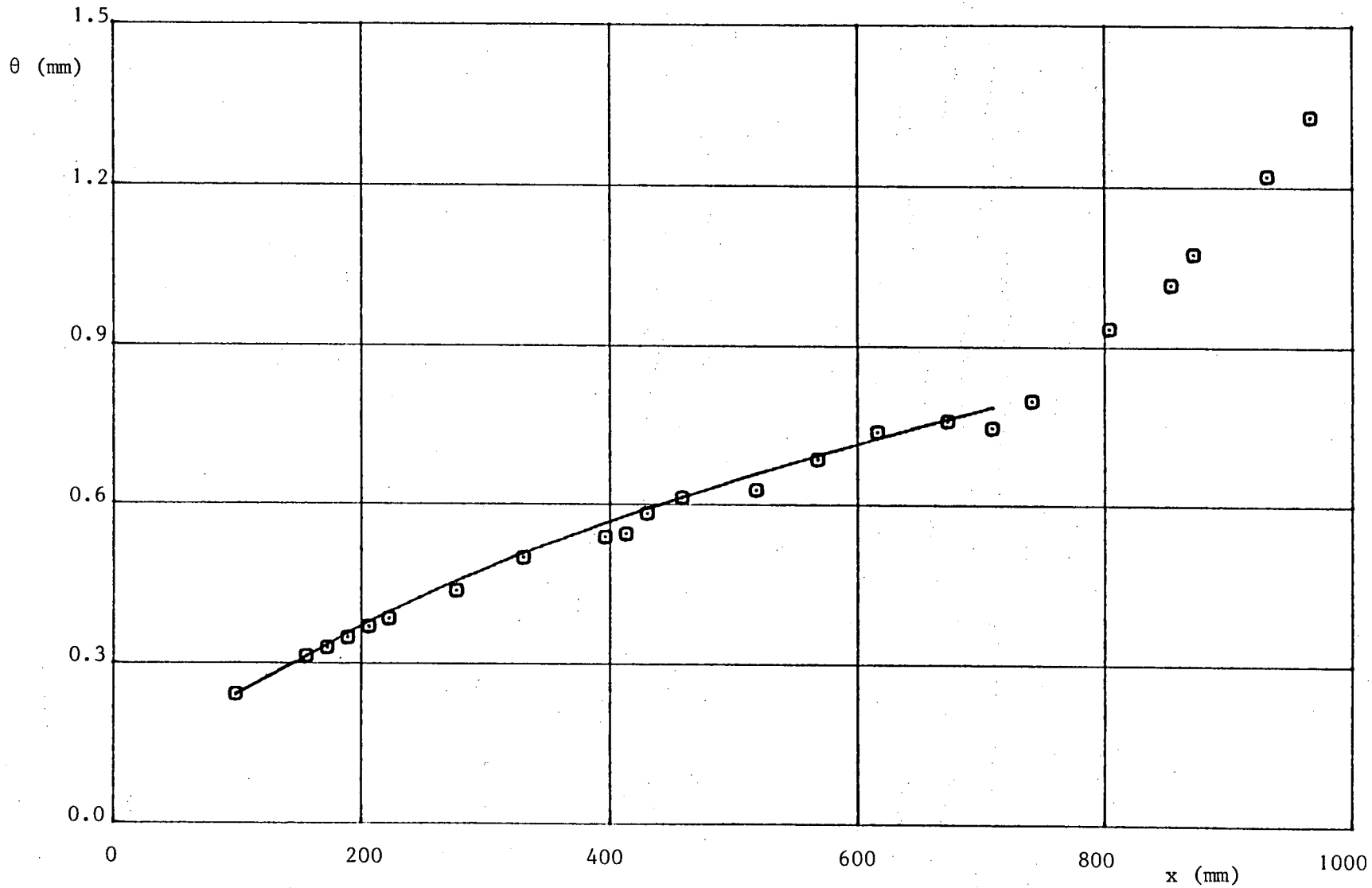

Figure 6.4b : Distribution of momentum thickness. (—) Bola results, (⊙) experiments (corrected wall distance).

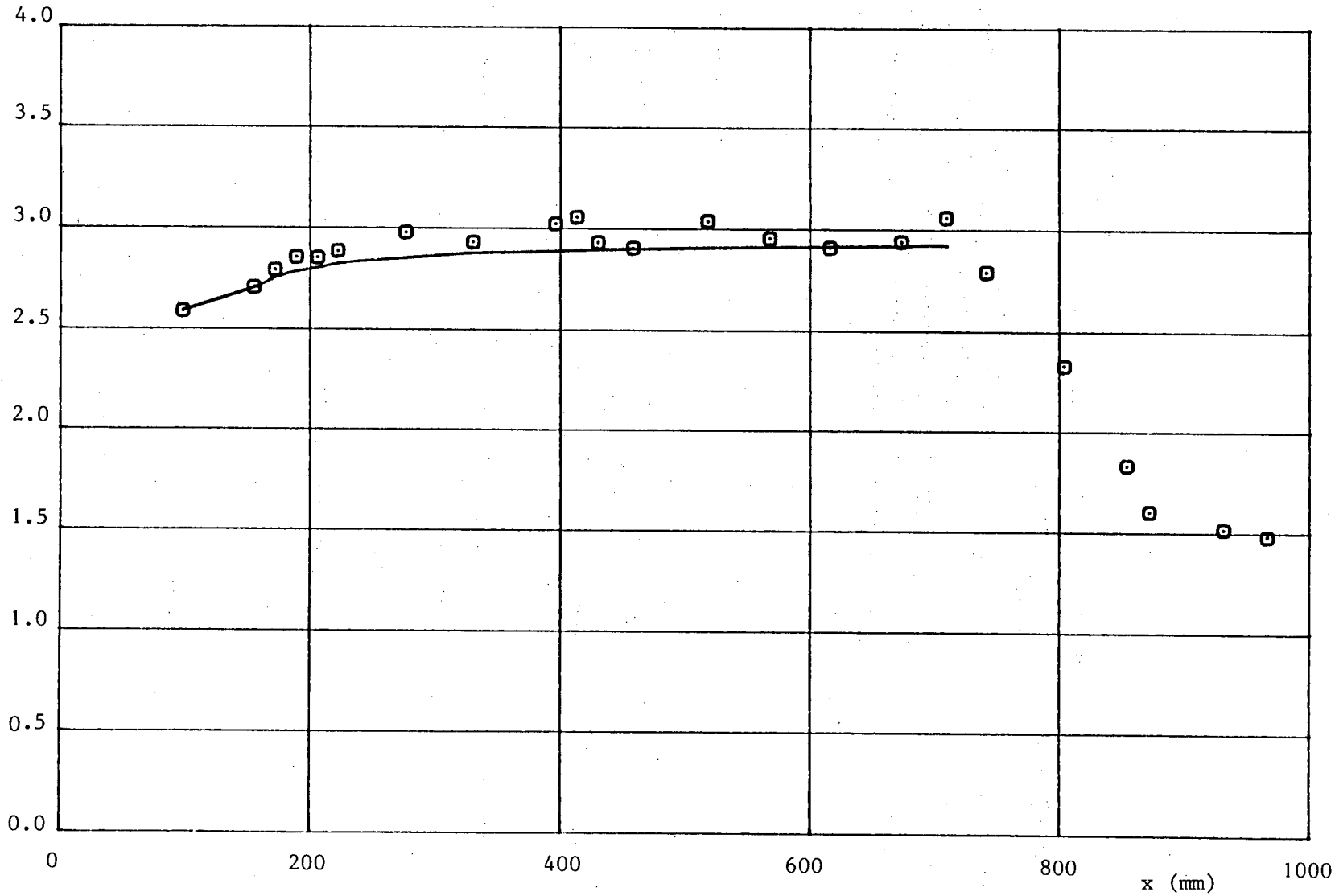

Figure 6.4c : Distribution of shape factor. (—) Bola results, (⊙) experiments (corrected wall distance).

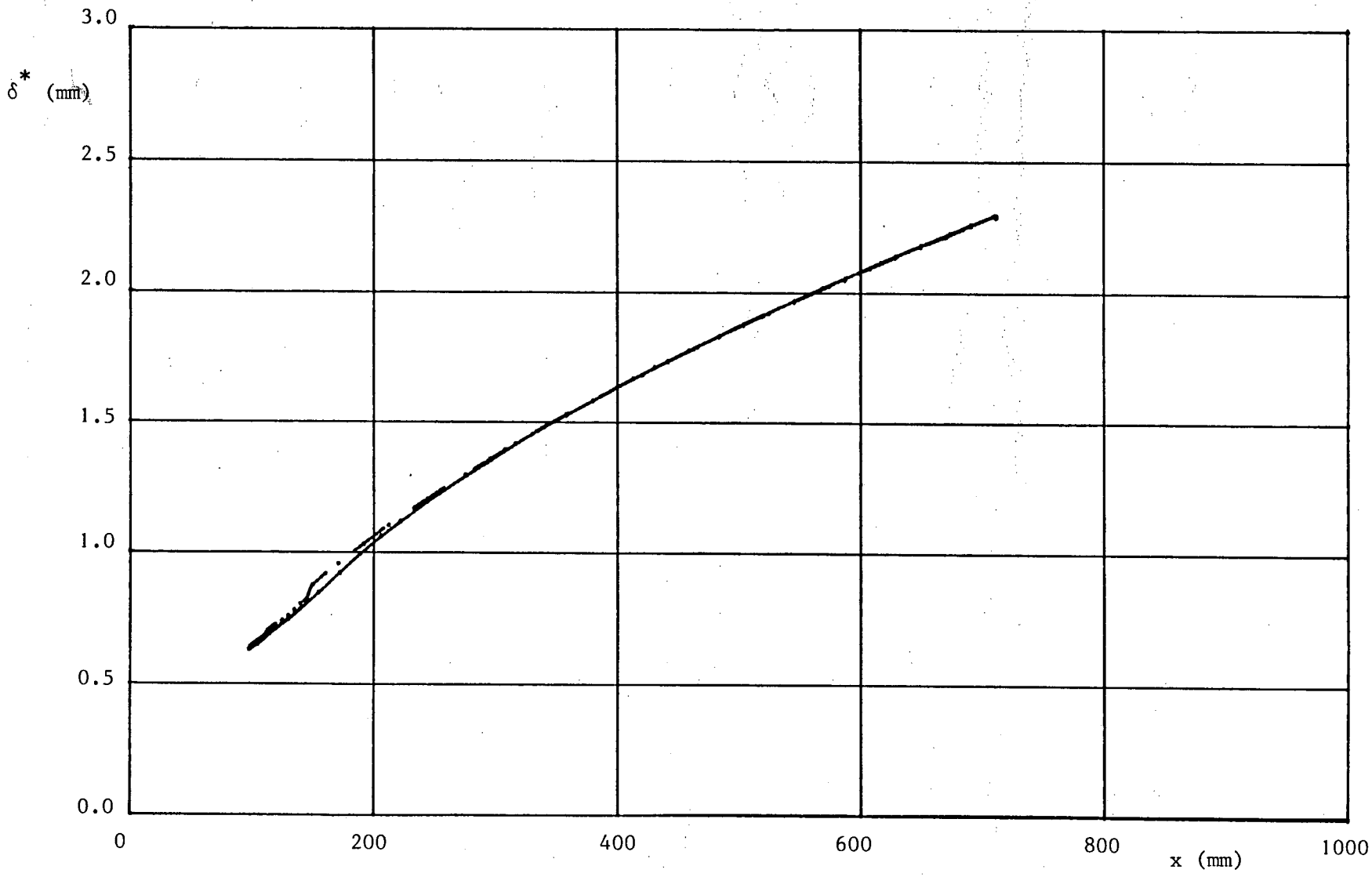

Figure 6.5a : Distribution of displacement thickness. (—) Bola results, (-·-) LSL program.

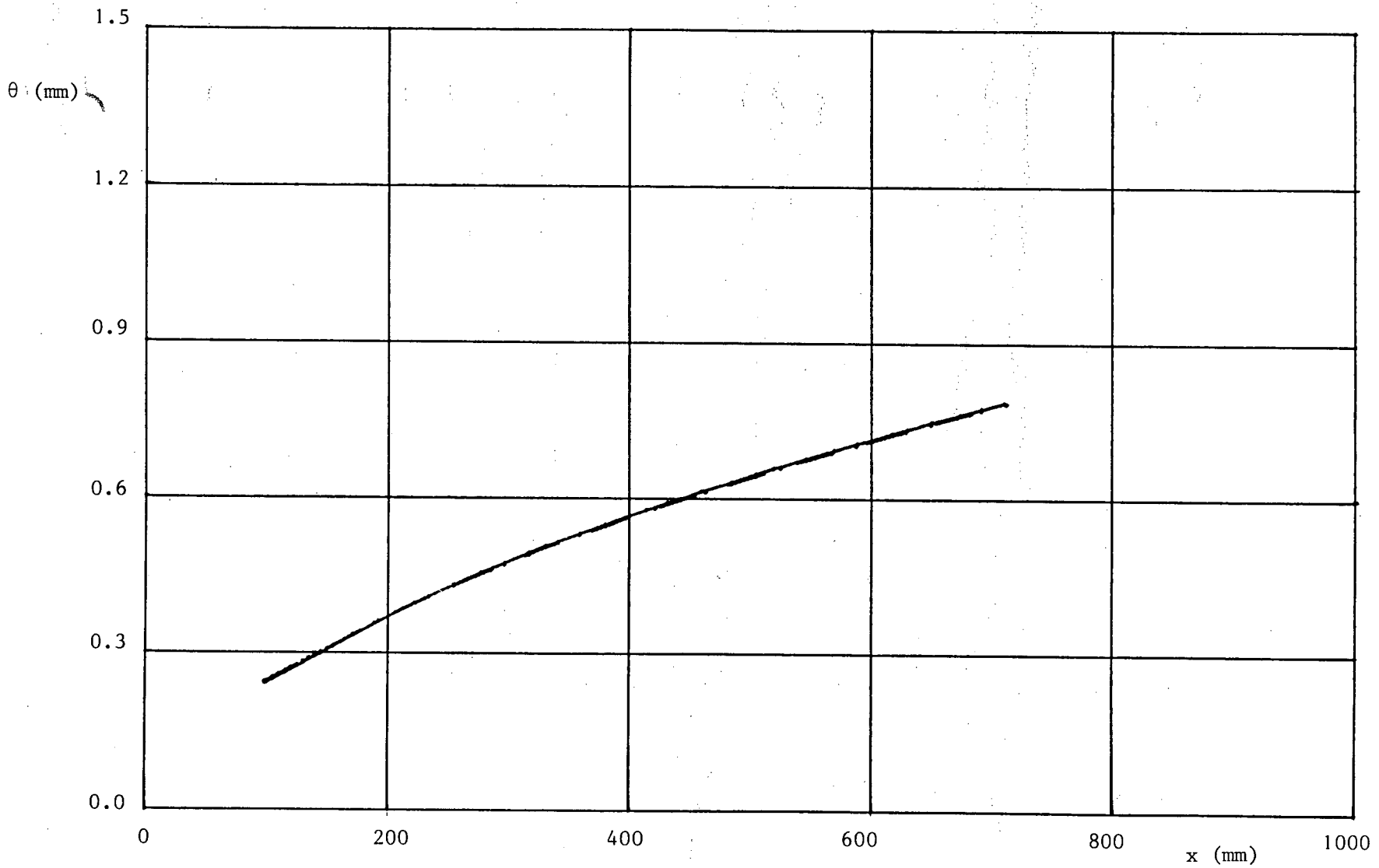

Figure 6.5b : Distribution of momentum thickness. (—) Bola results, (-·-) LSL program.

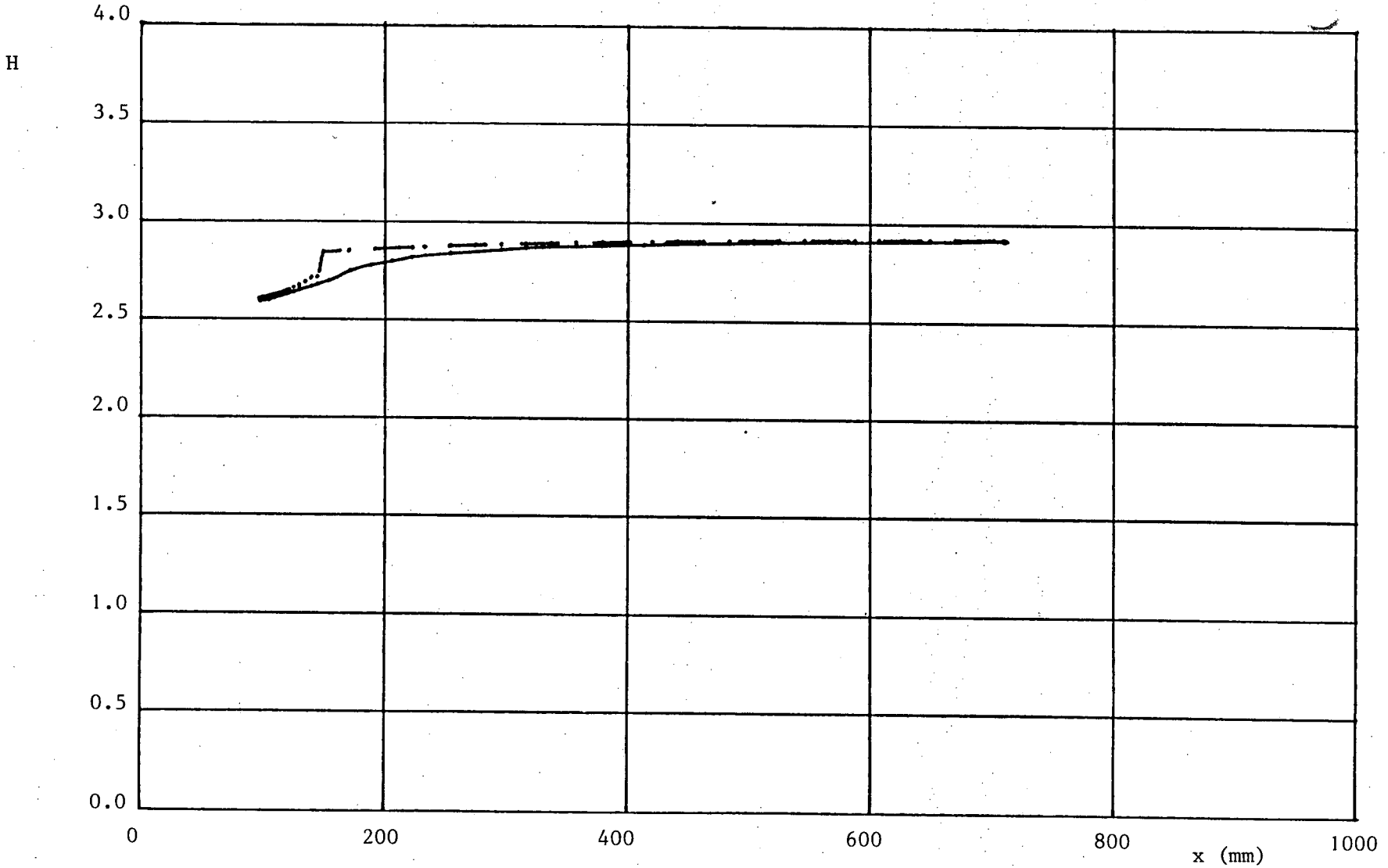

Figure 6.5c : Distribution of shape factor. (—) Bola results, (-·-) LSL program.

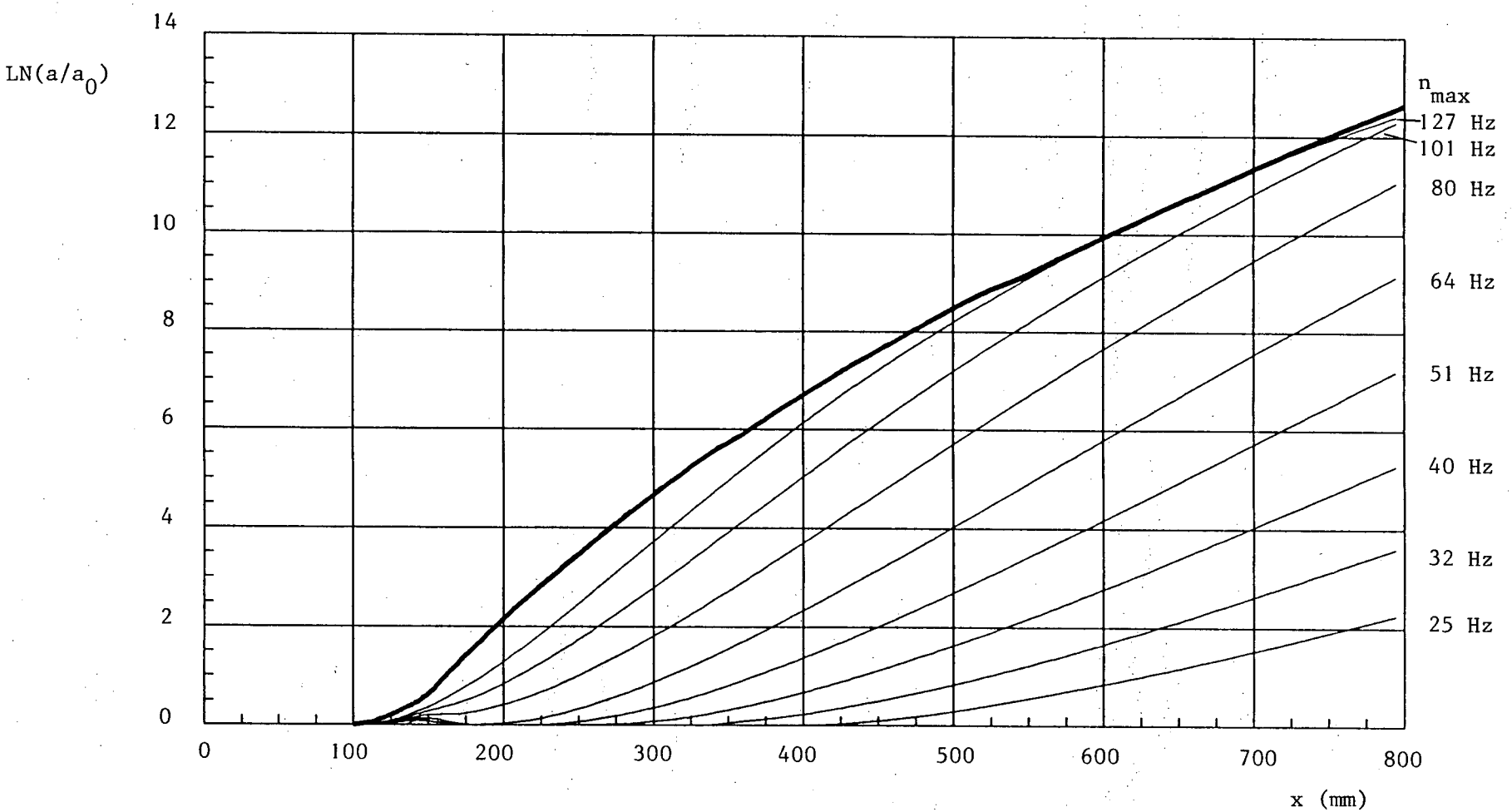

Figure 6.6a : Amplification curves for several frequencies as function of streamwise coordinate. Calculated with the LSL program. Maximum amplification curve included.

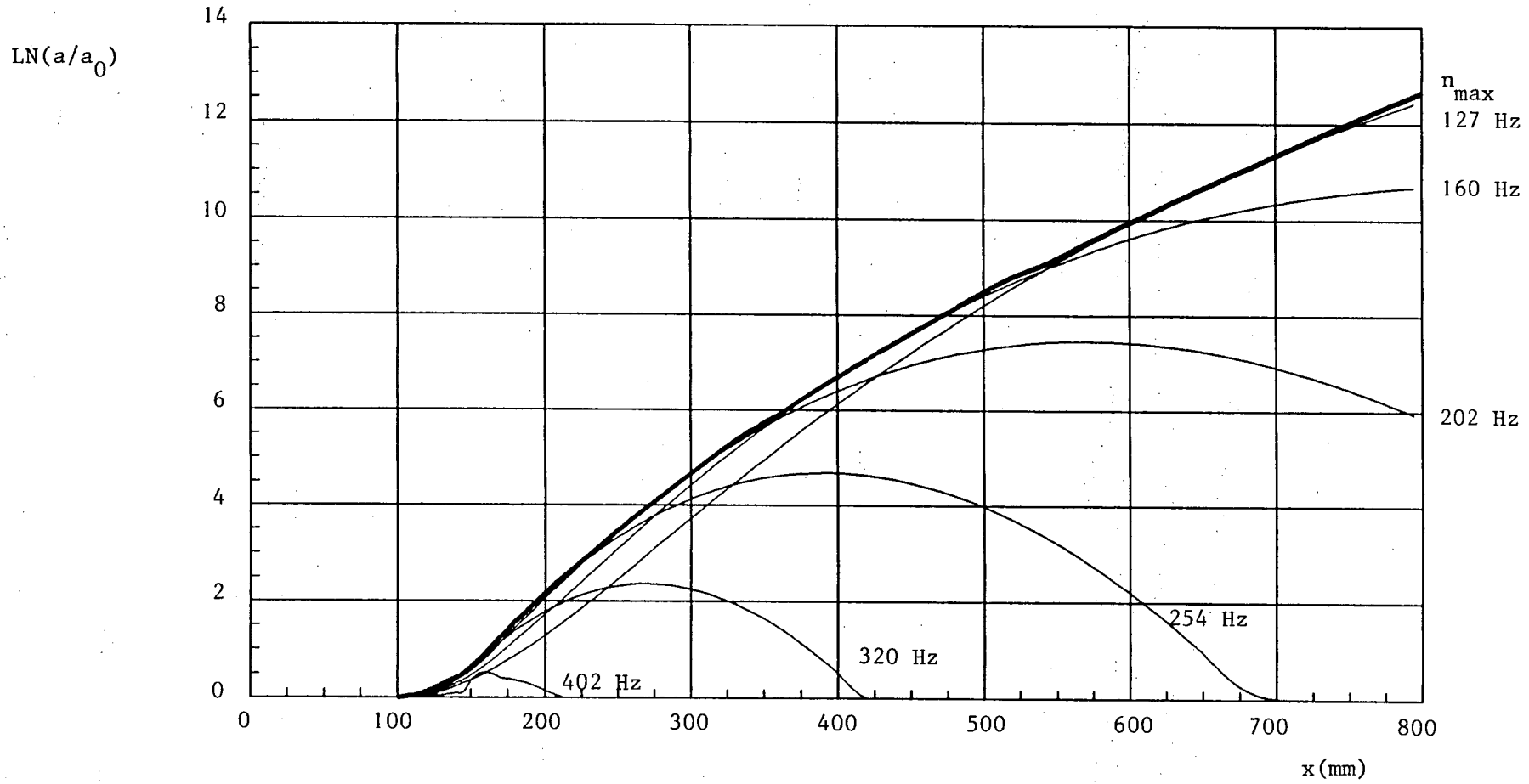

Figure 6.6b : Continued.

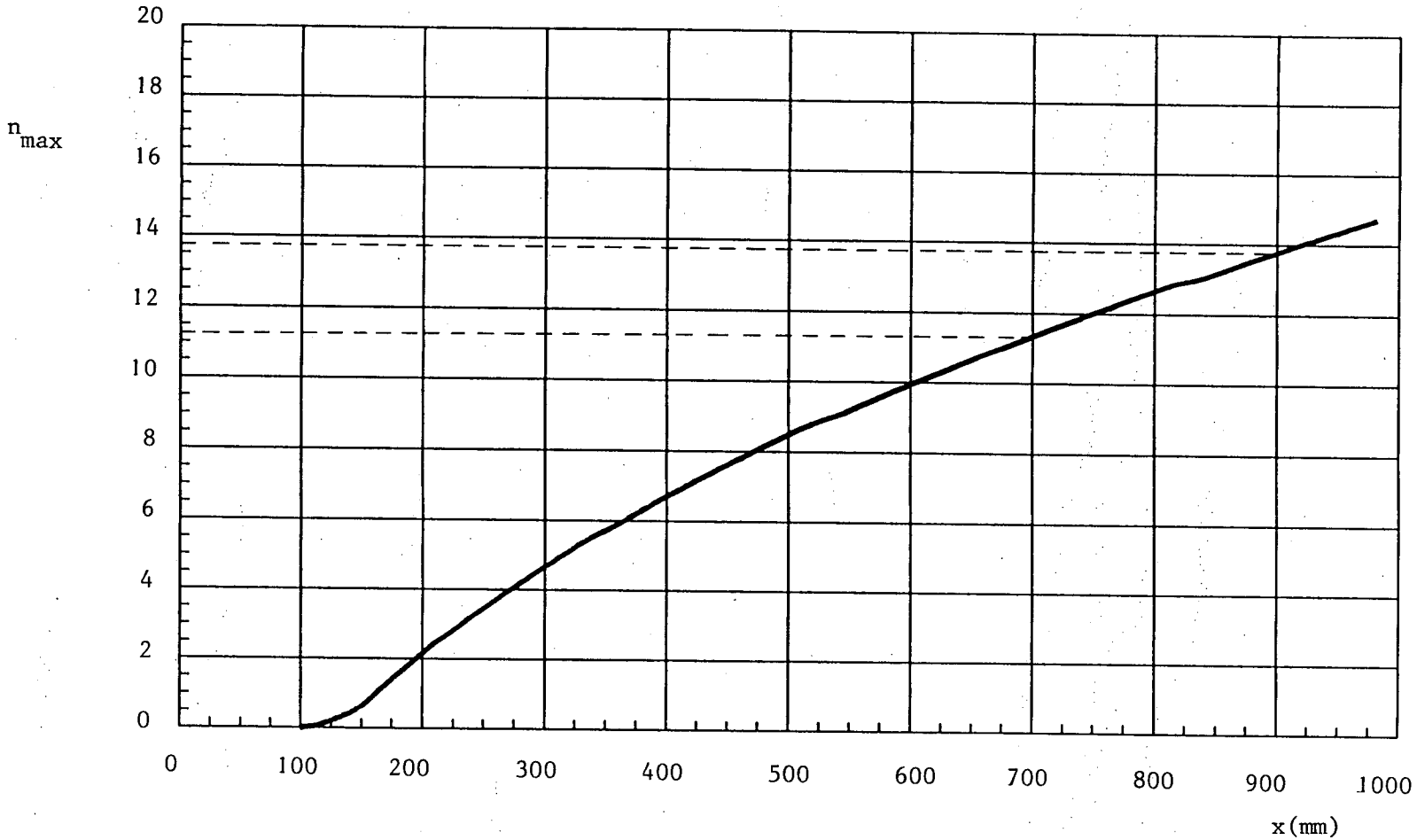

Figure 6.7 : Envelope curve of maximum amplification factor as function of streamwise coordinate.

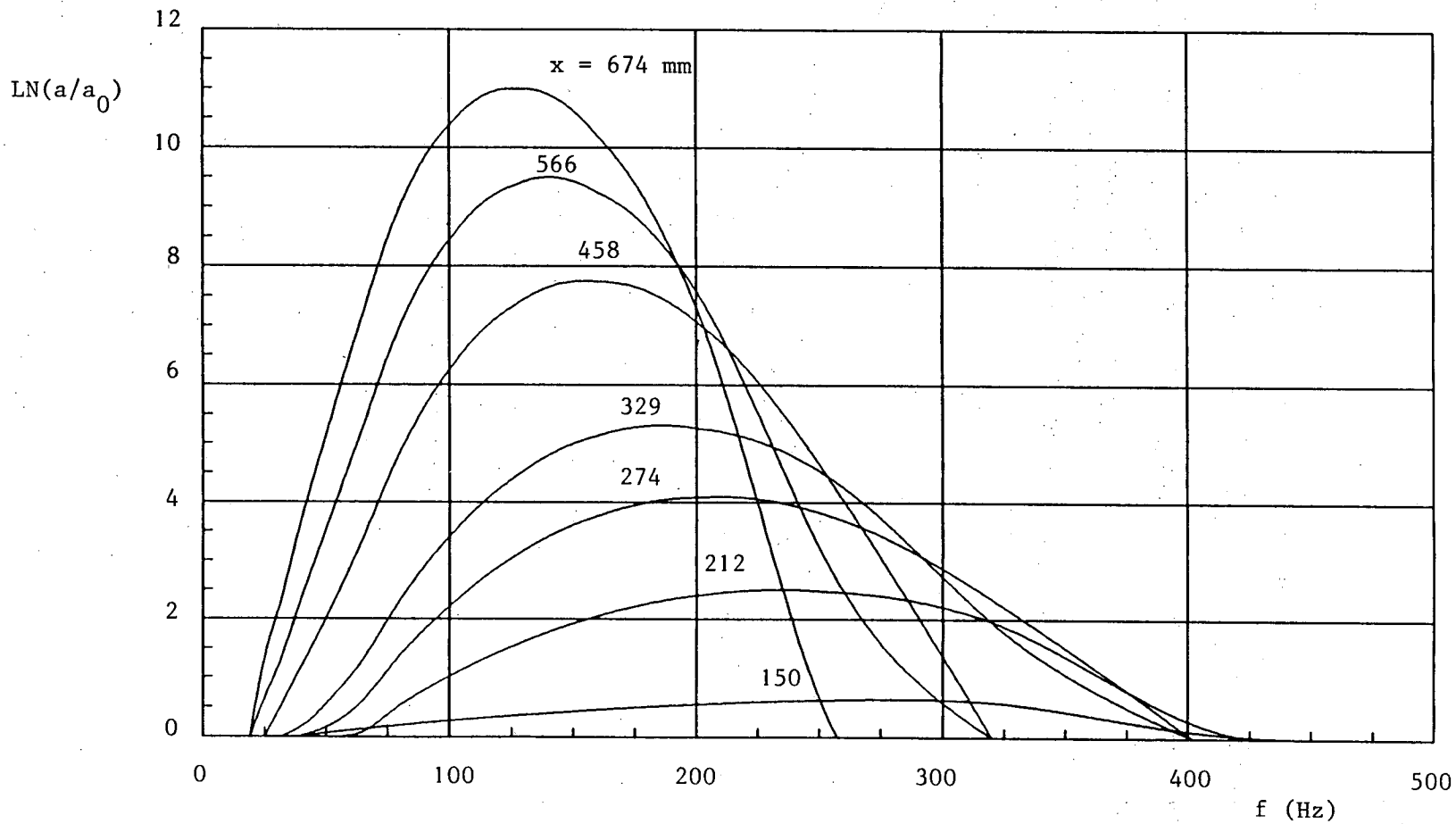

Figure 6.8 : Calculated amplification curves for several streamwise coordinates as function of frequency.

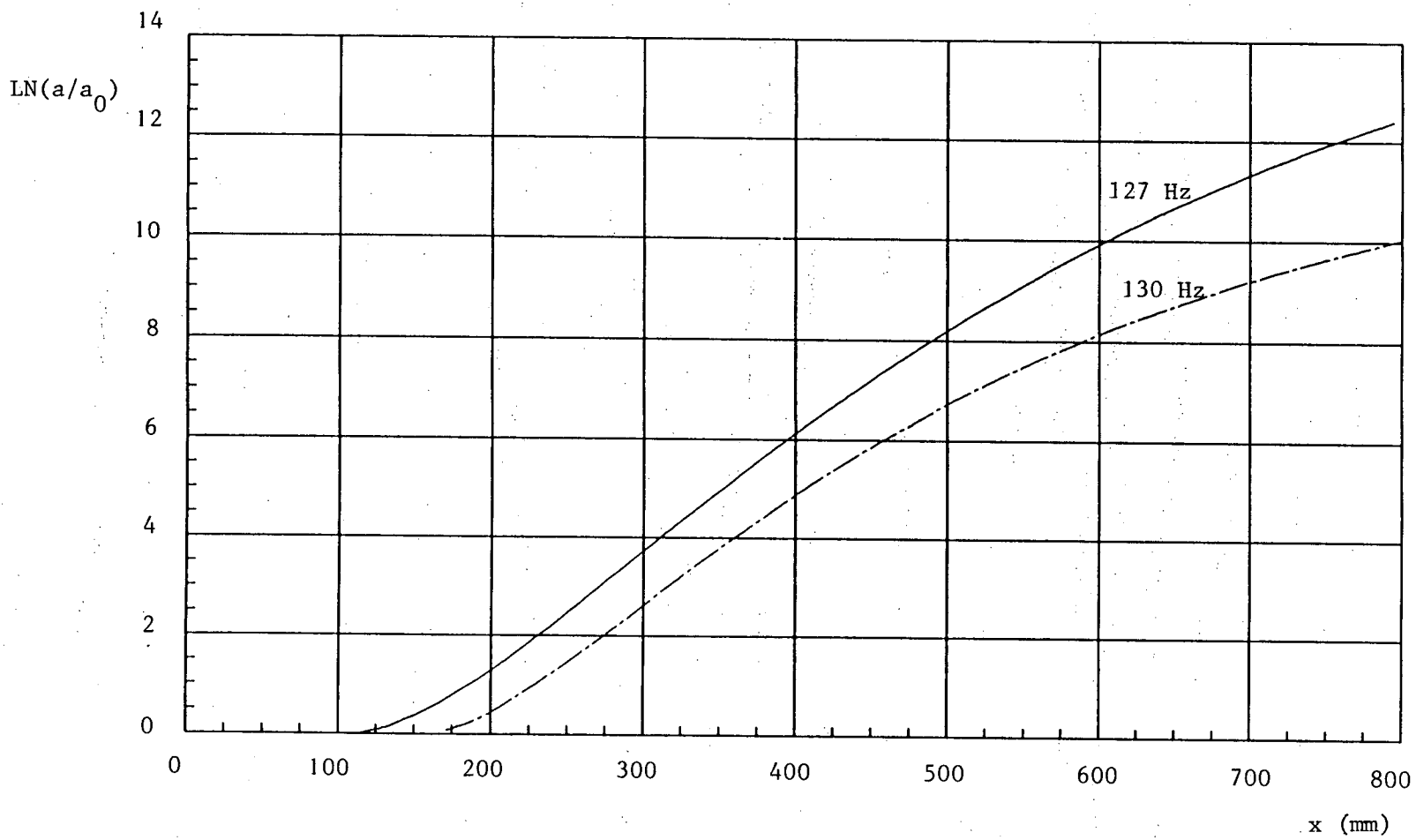

Figure 6.9 : Amplification curves calculated with Cosal (-·-) and the LSL program (——).

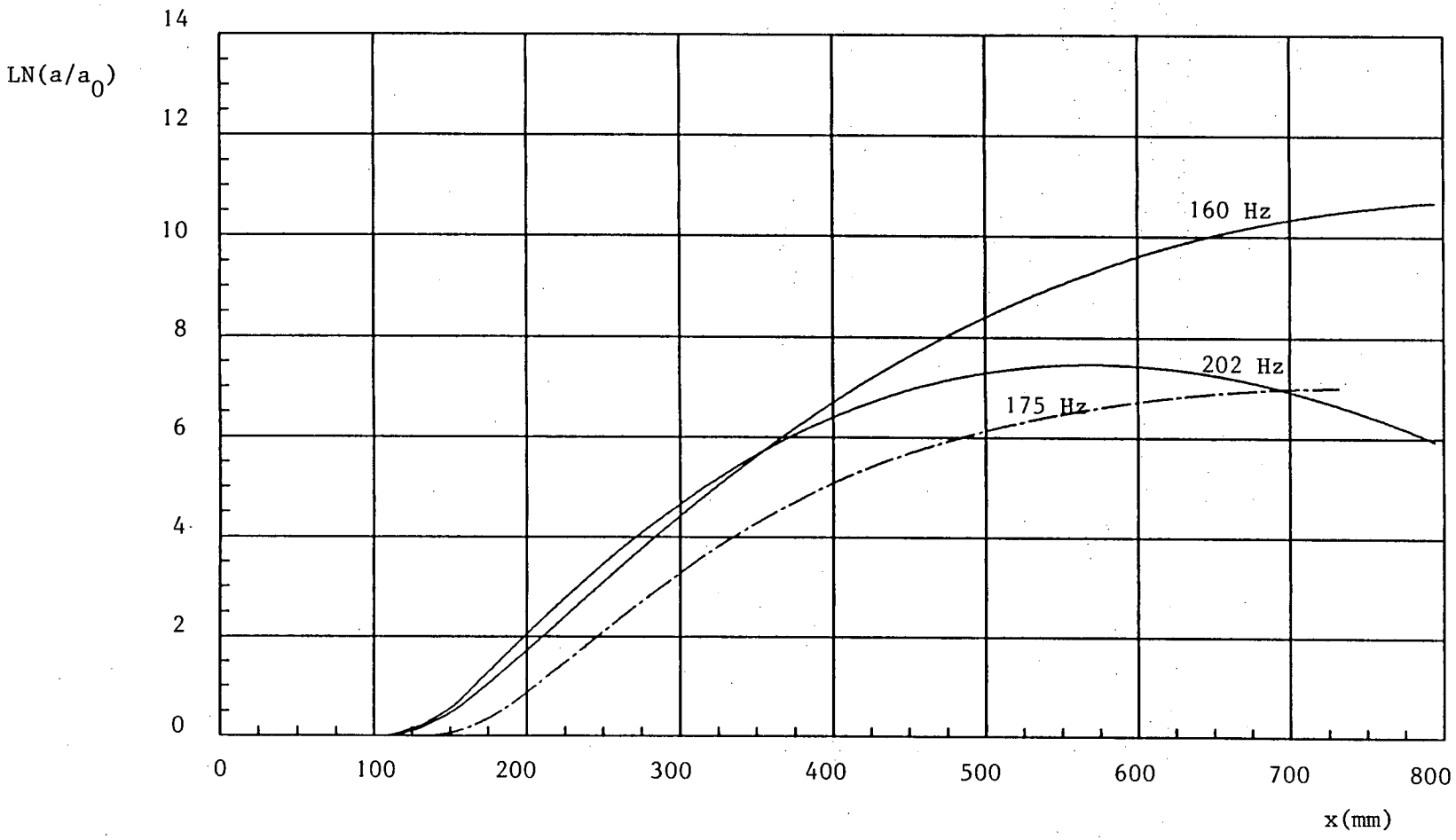

Figure 6.10 : Amplification curves calculated with Cosal (-·-) and the LSL program (——).

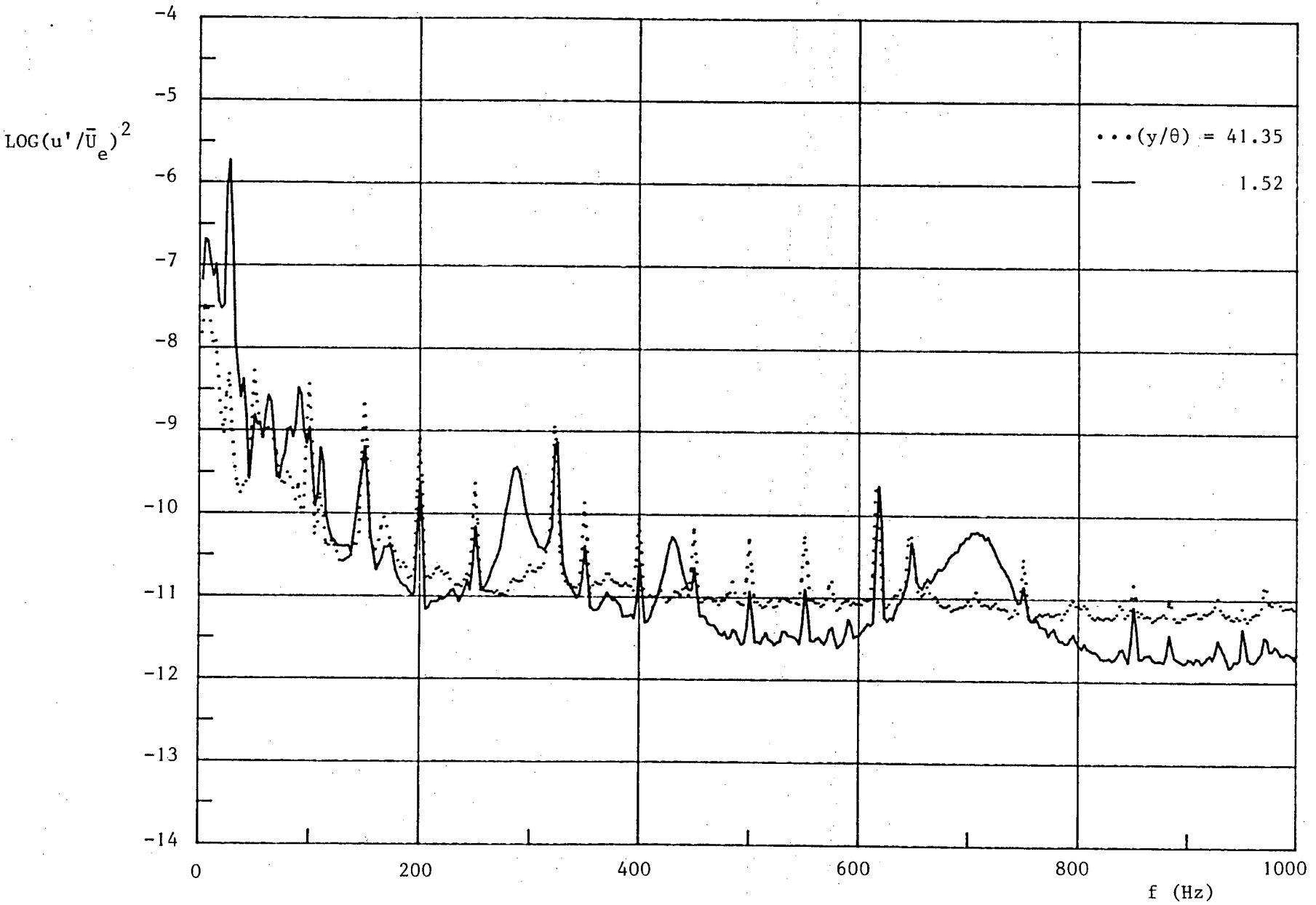

Figure 6.11a : Velocity power spectra across the boundary layer, x = 98 mm.

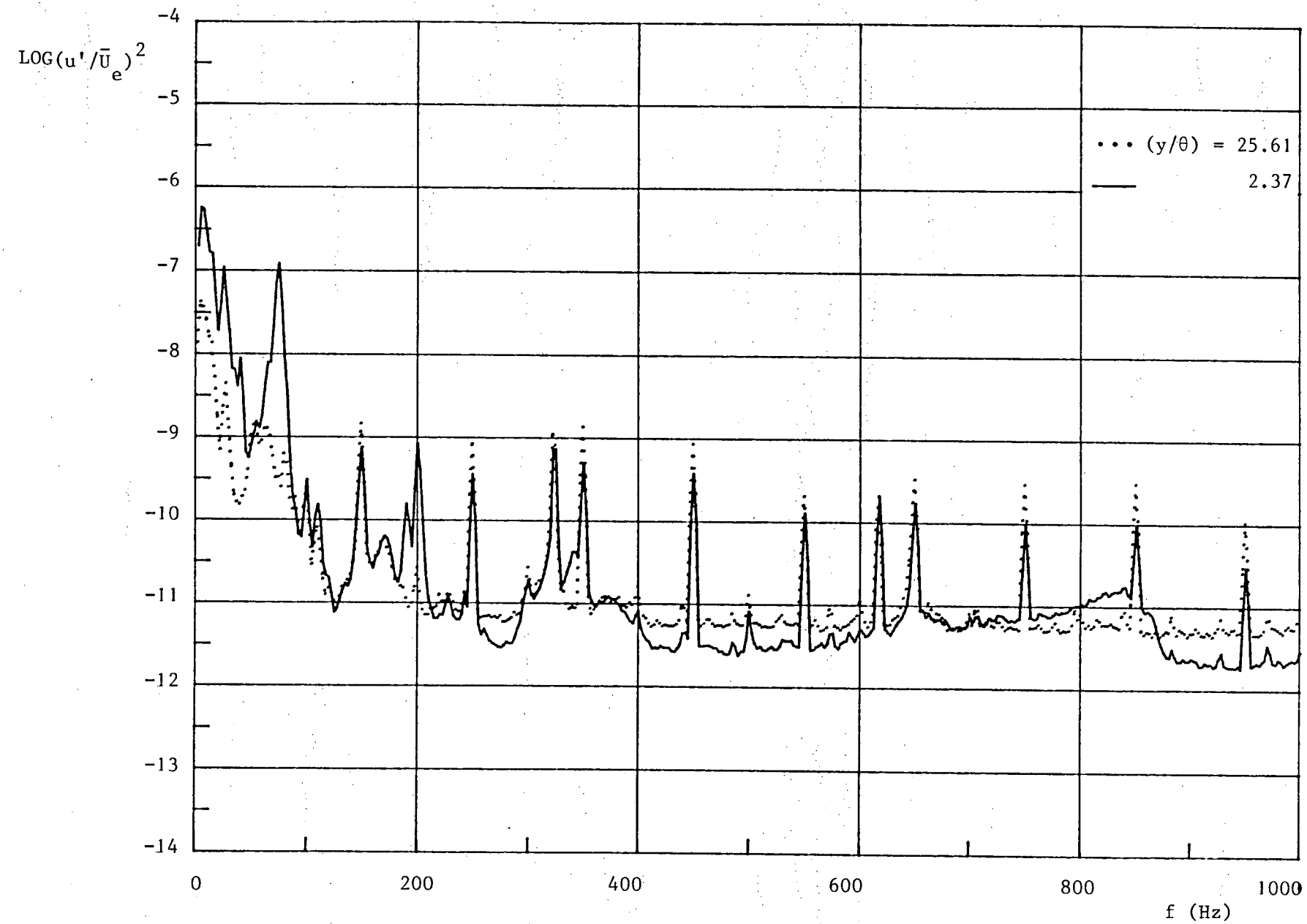

Figure 6.11b : Continued, x = 155^2 mm.

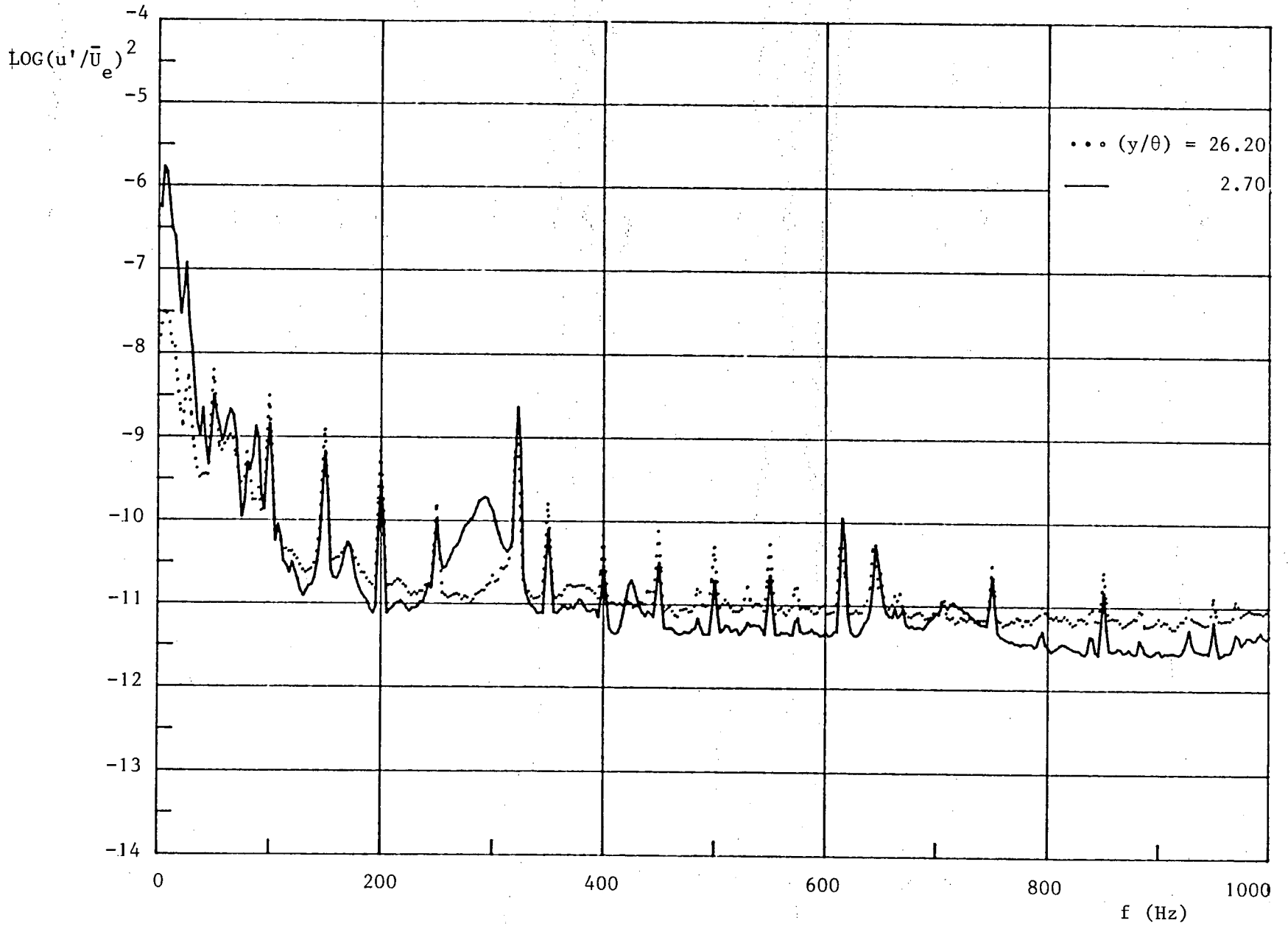

Figure 6.11c : Continued, x= 222 mm.

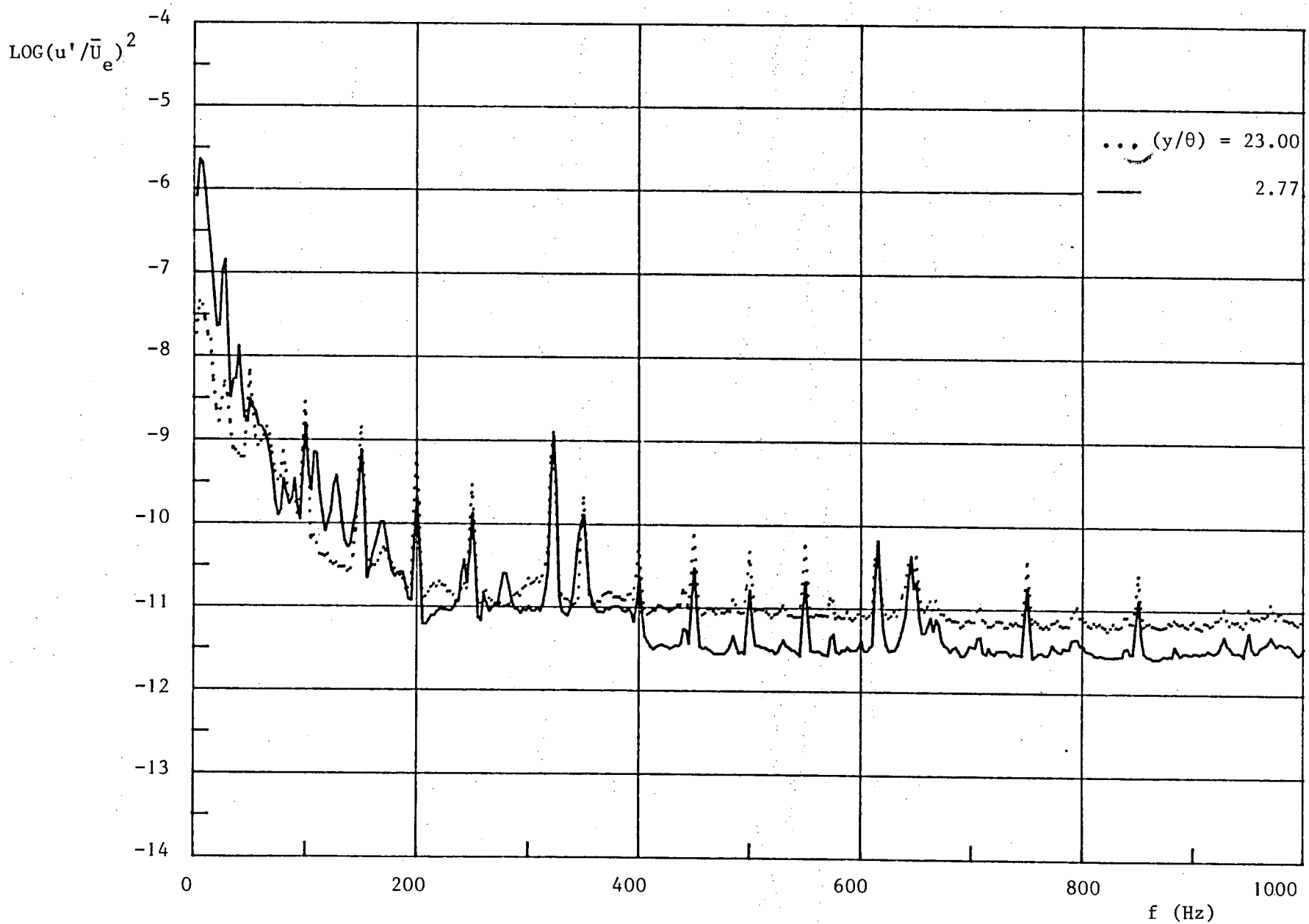

Figure 6.11d : Continued, x = 276 mm.

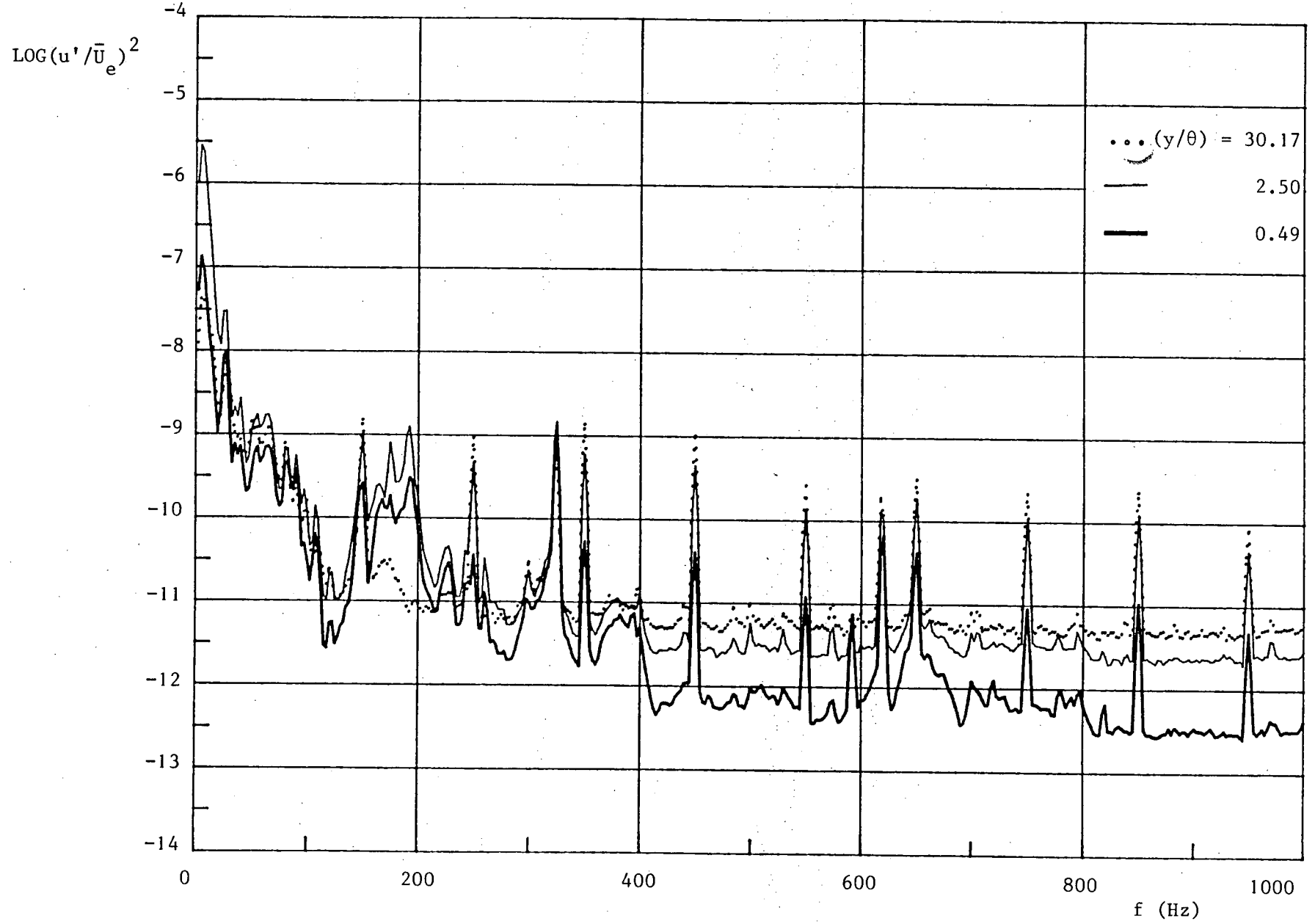

Figure 6.11e : Continued, x = 330[1] mm.

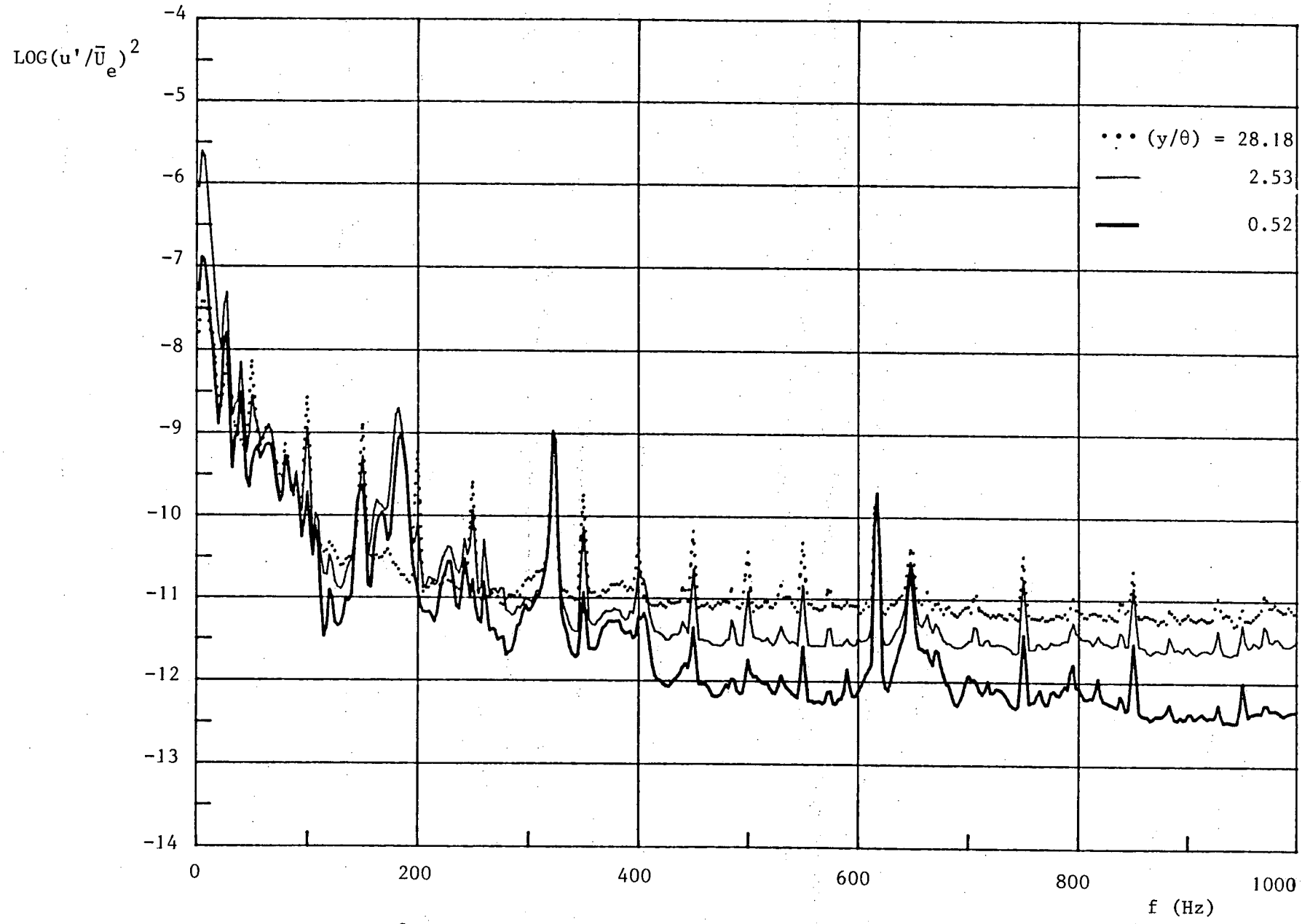

Figure 6.11f : Continued, x = 330^2 mm.

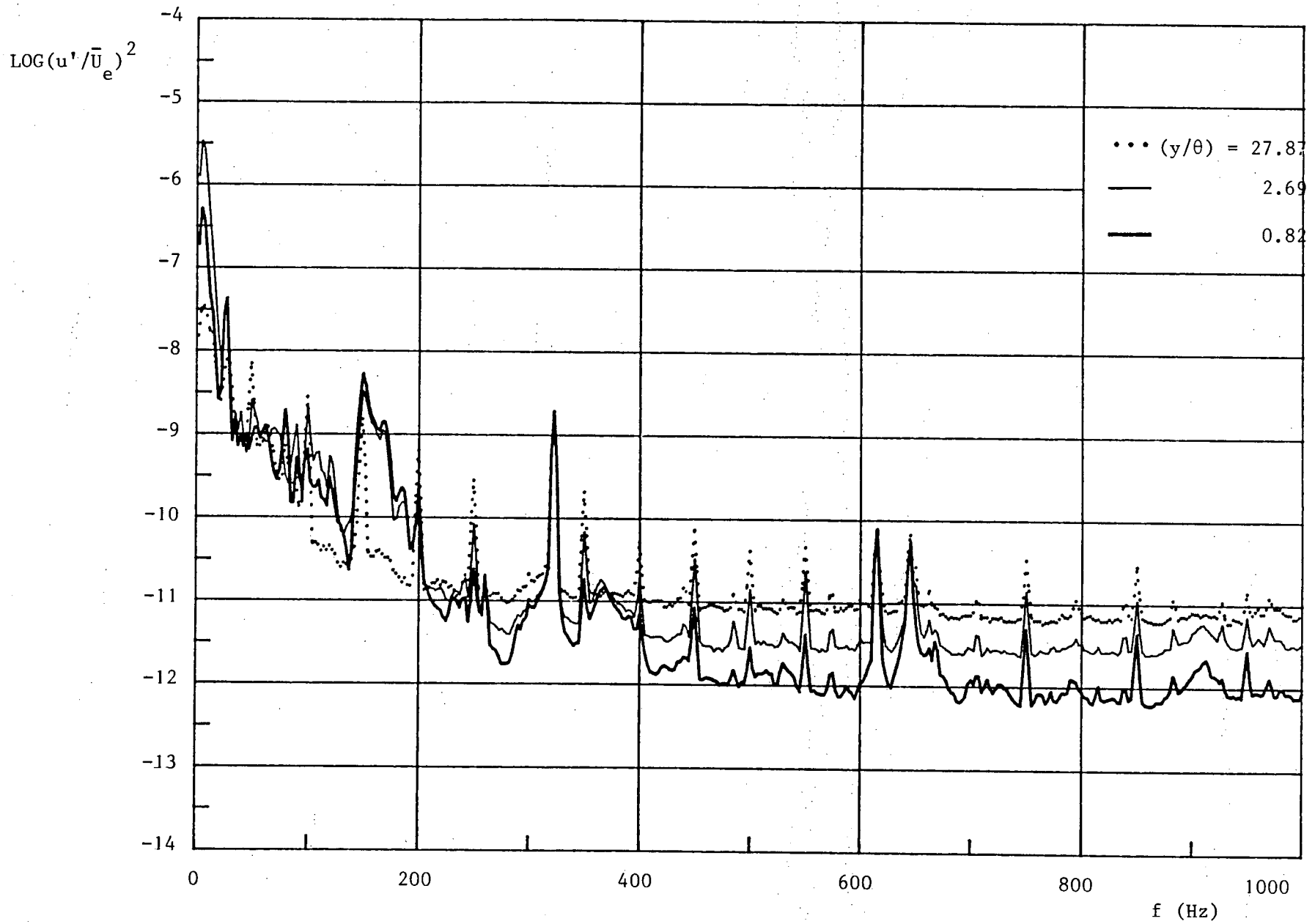

Figure 6.11g : Continued, x = 396^2 mm.

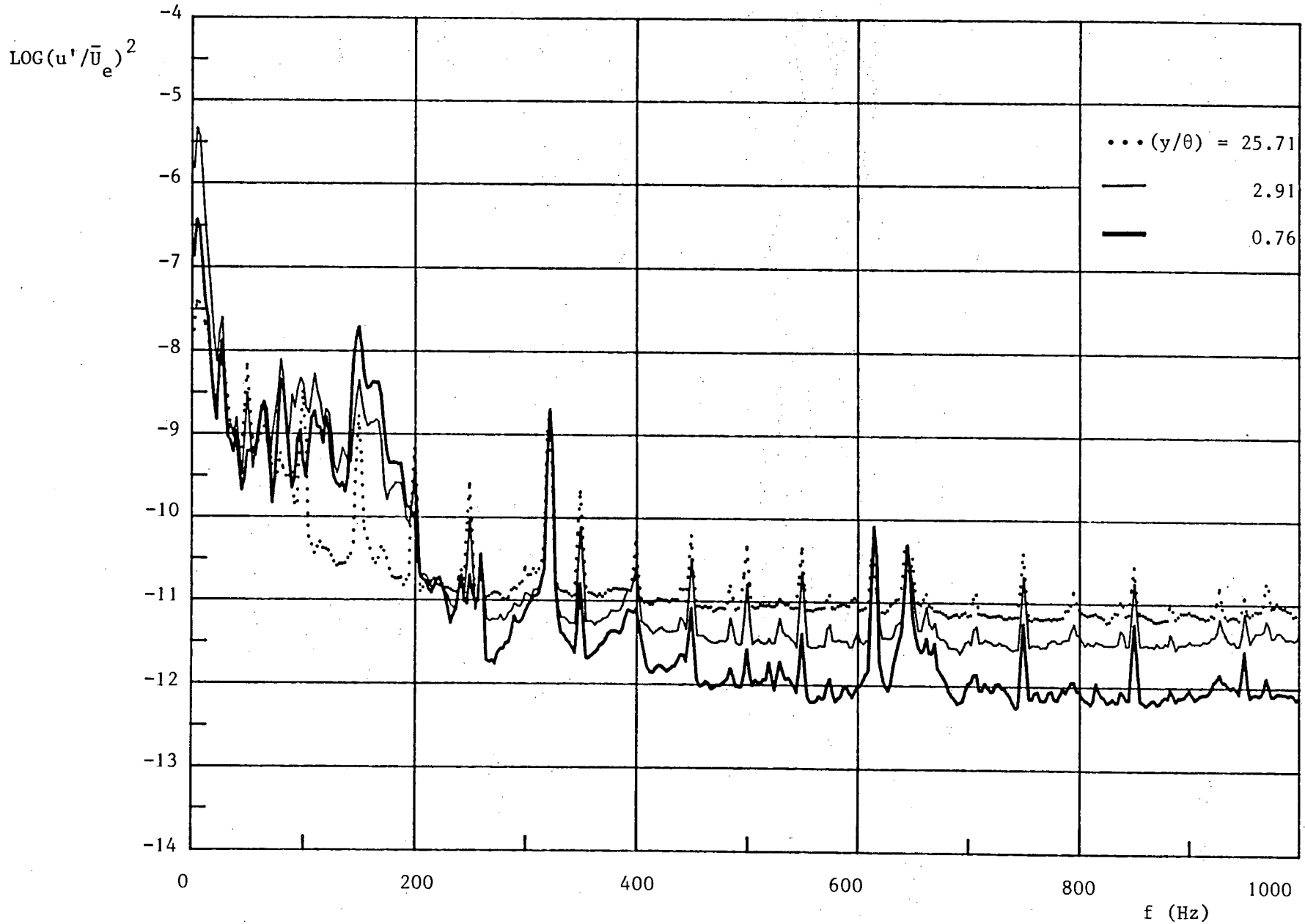

Figure 6.11h : Continued, x = 430 mm.

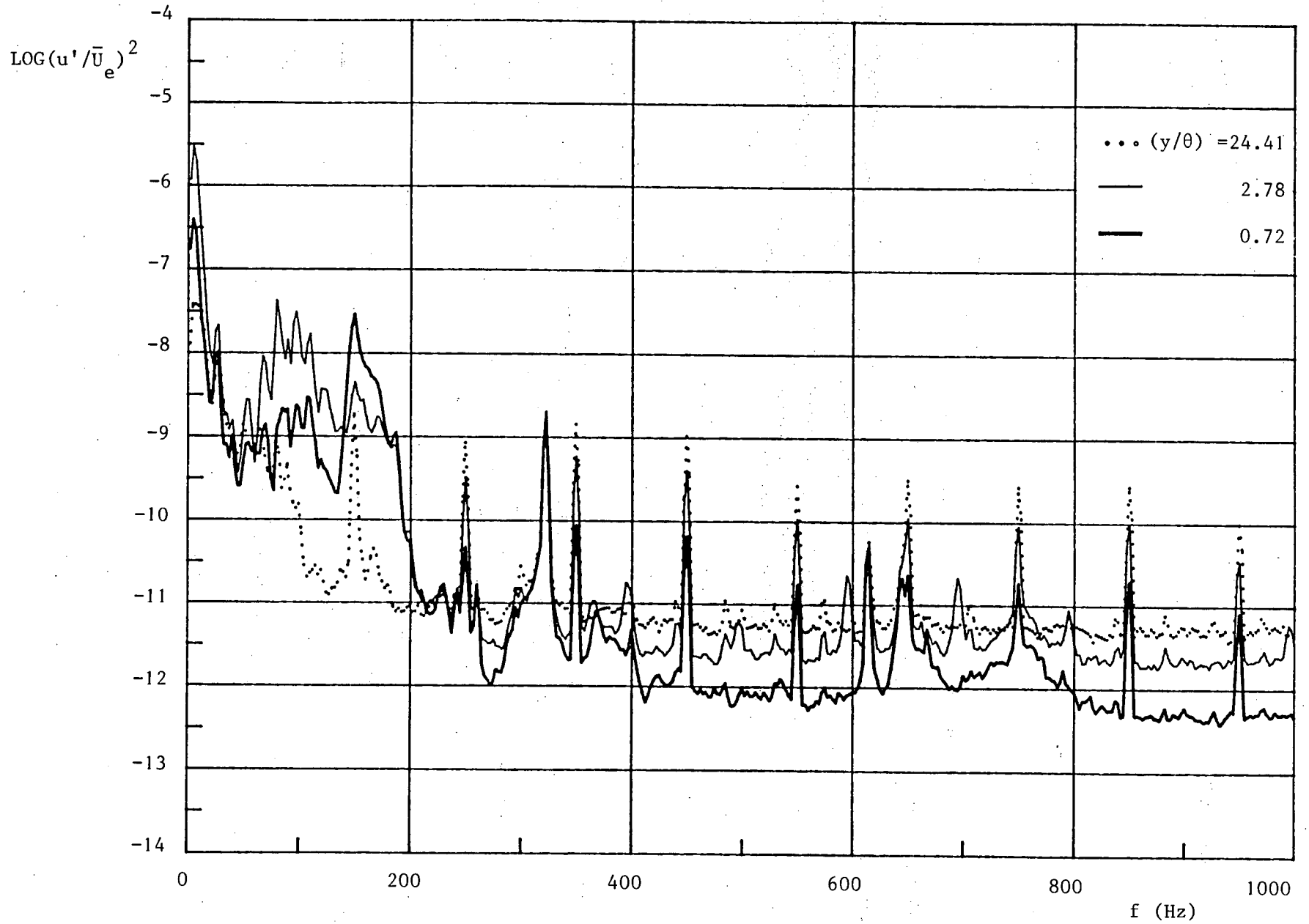

Figure 6.11 i : Continued, x = 458 mm.

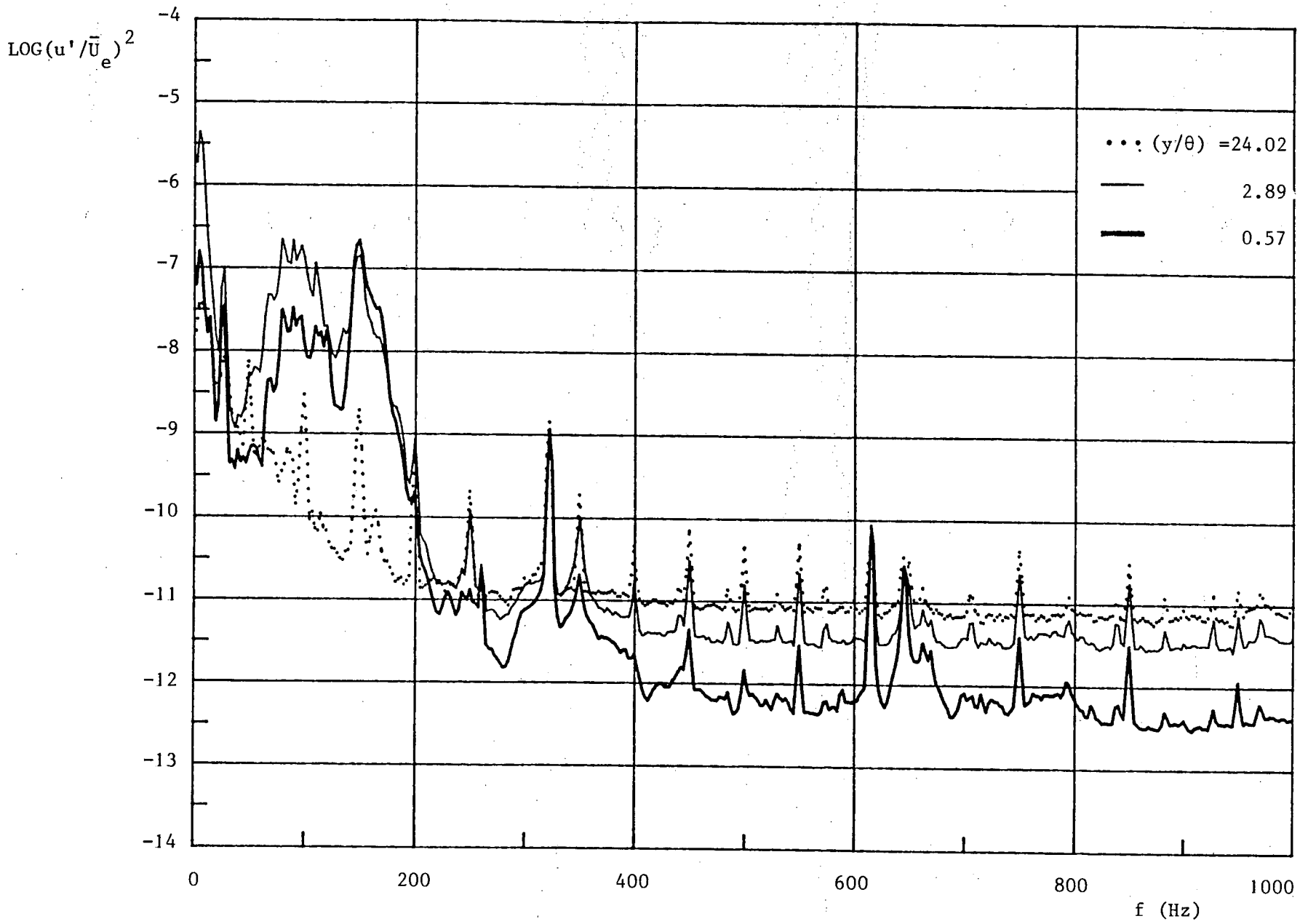

Figure 6.11j : Continued, x = 518 mm.

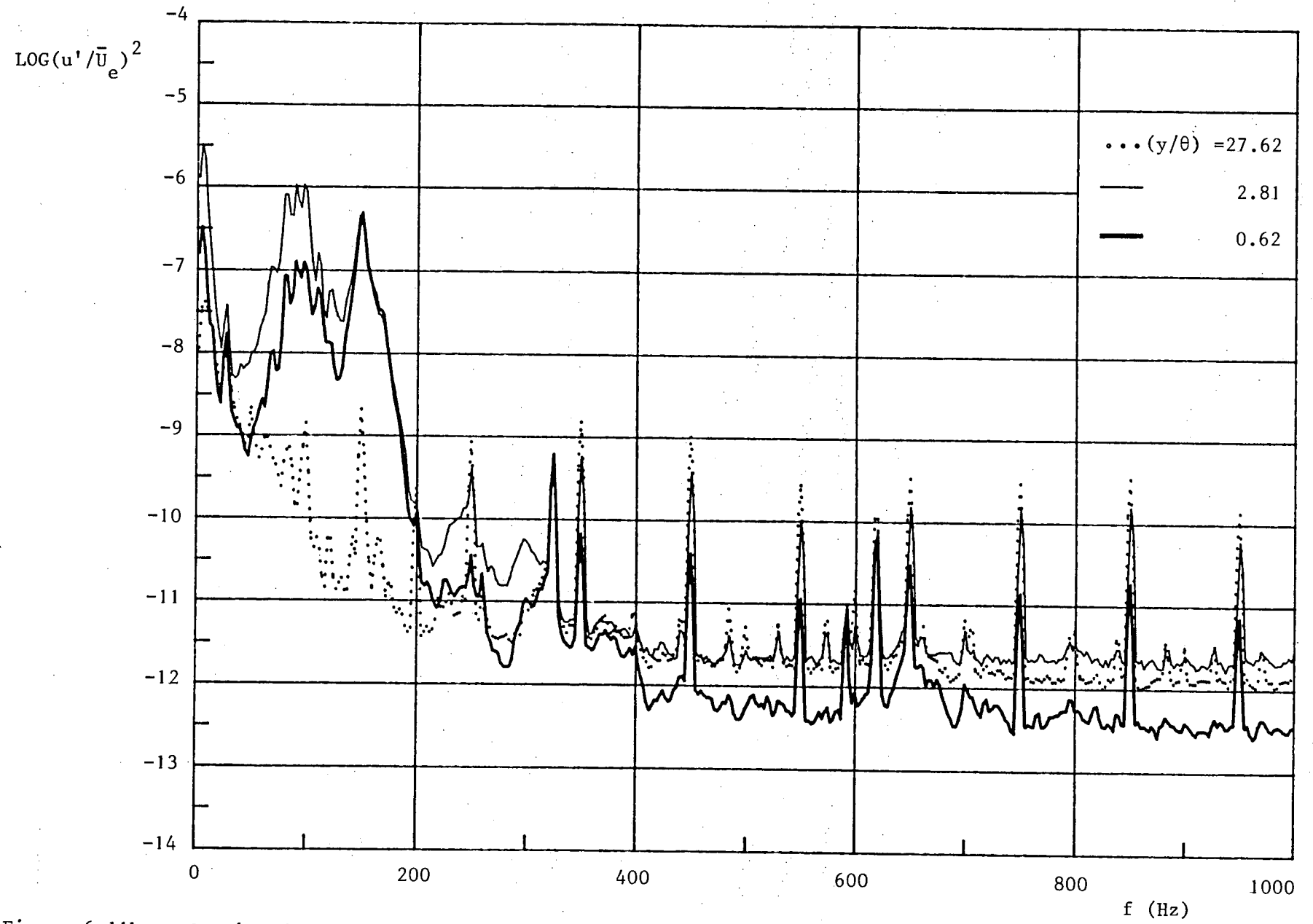

Figure 6.11k : Continued, x = 568 mm.

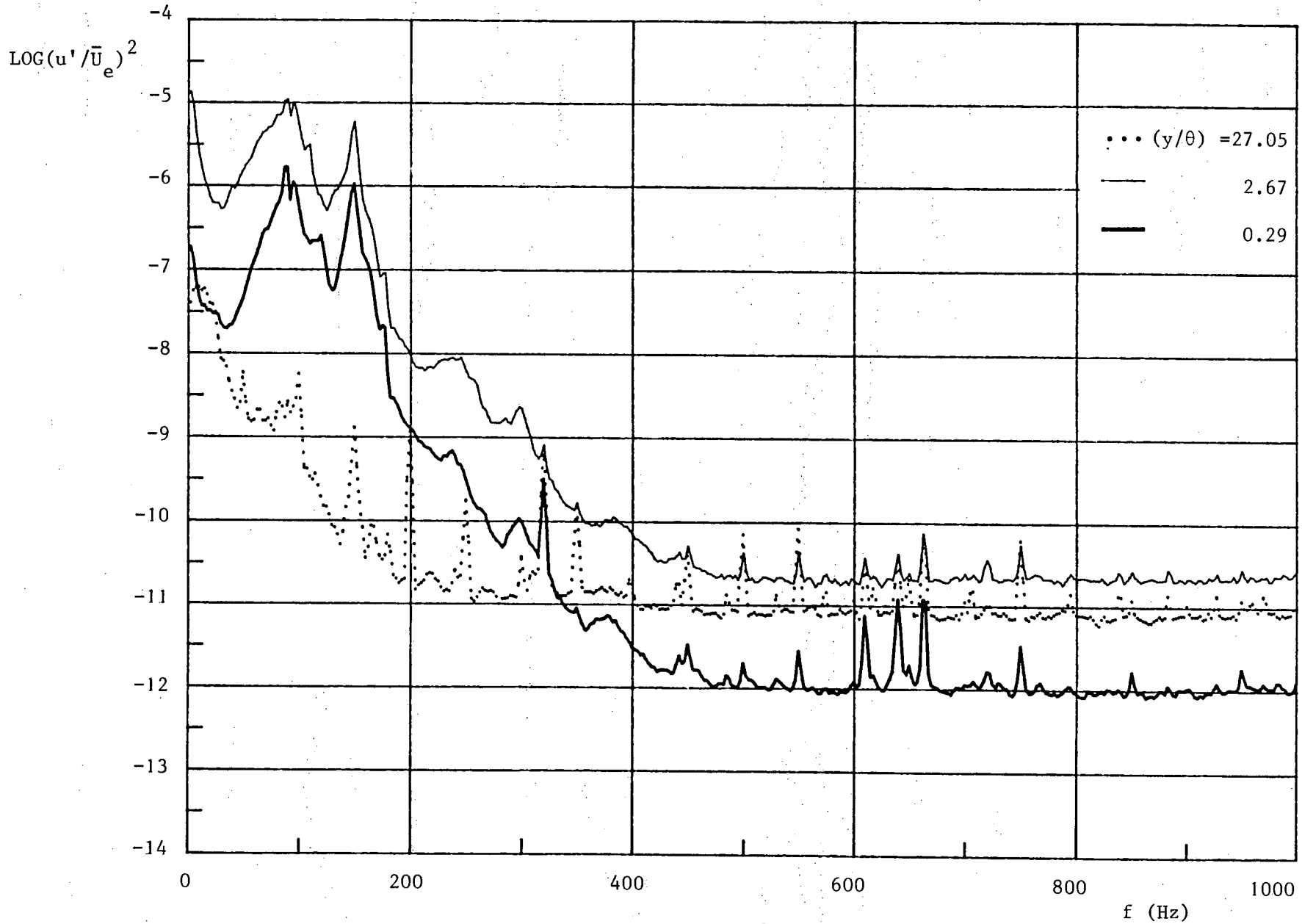

Figure 6.111 : Continued, x = 616 mm.

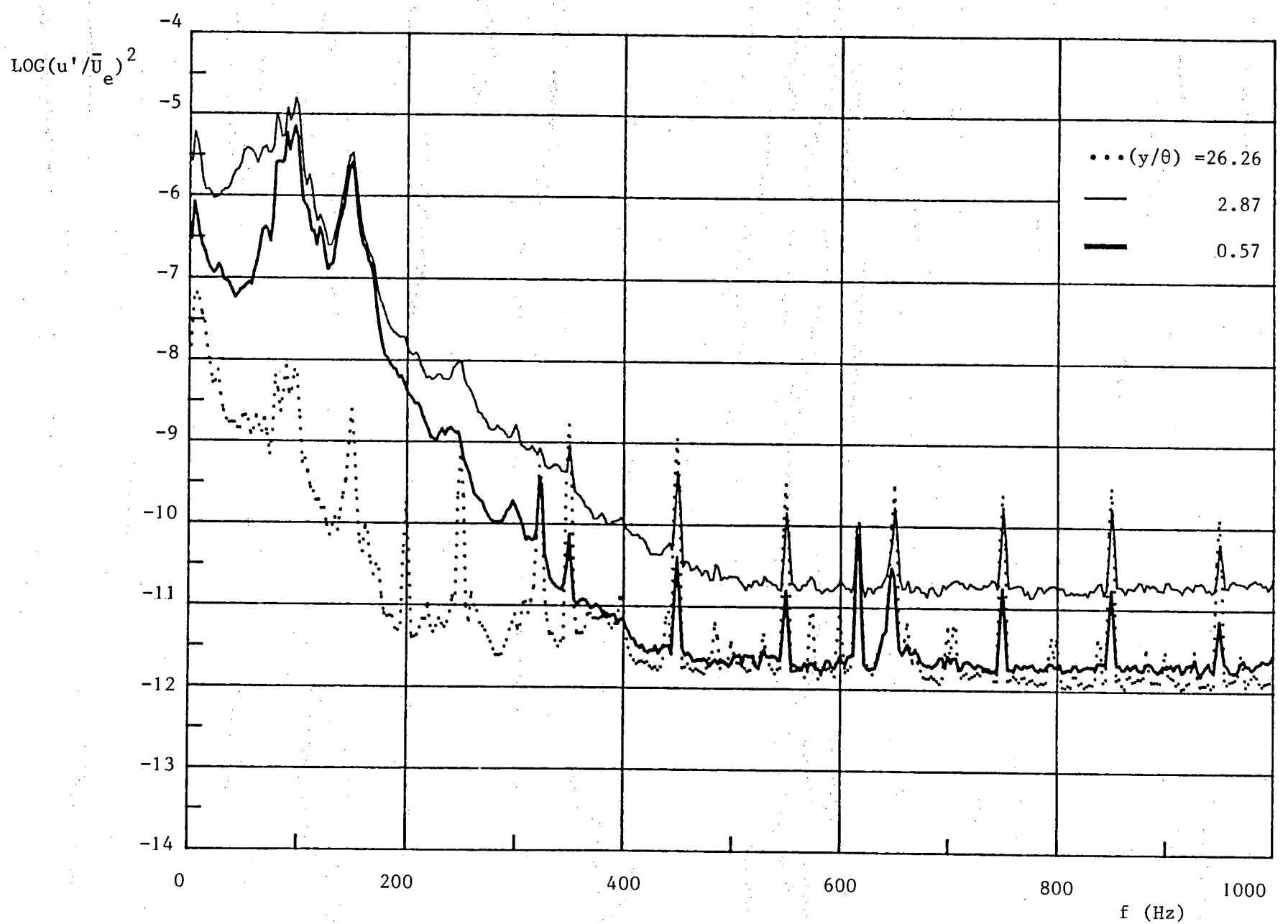

Figure 6.11.m : Continued, x = 673 mm.

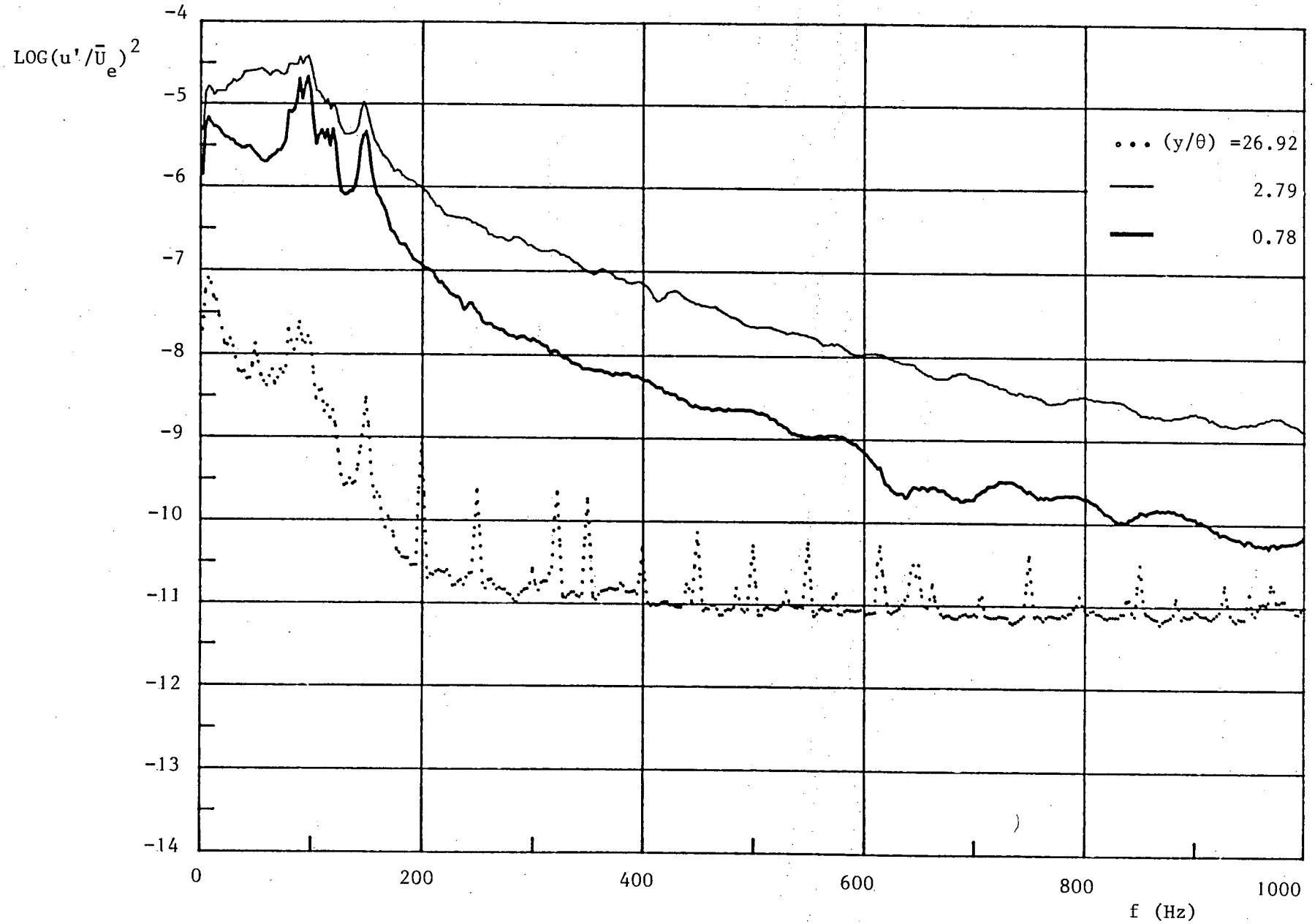

Figure 6.11n : Continued, x = 709 mm.

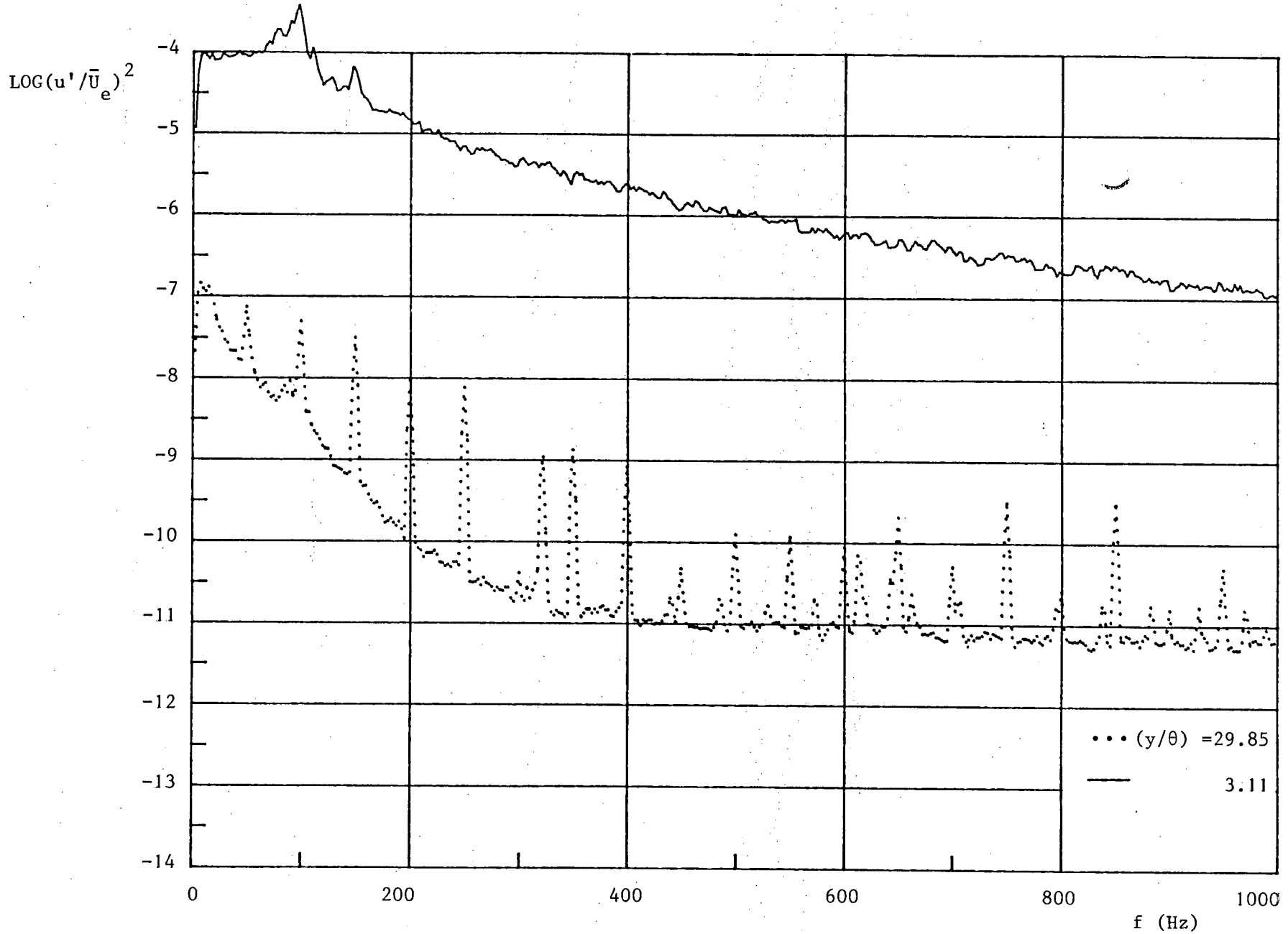

Figure 6.11o : Continued, x = 741^2 mm.

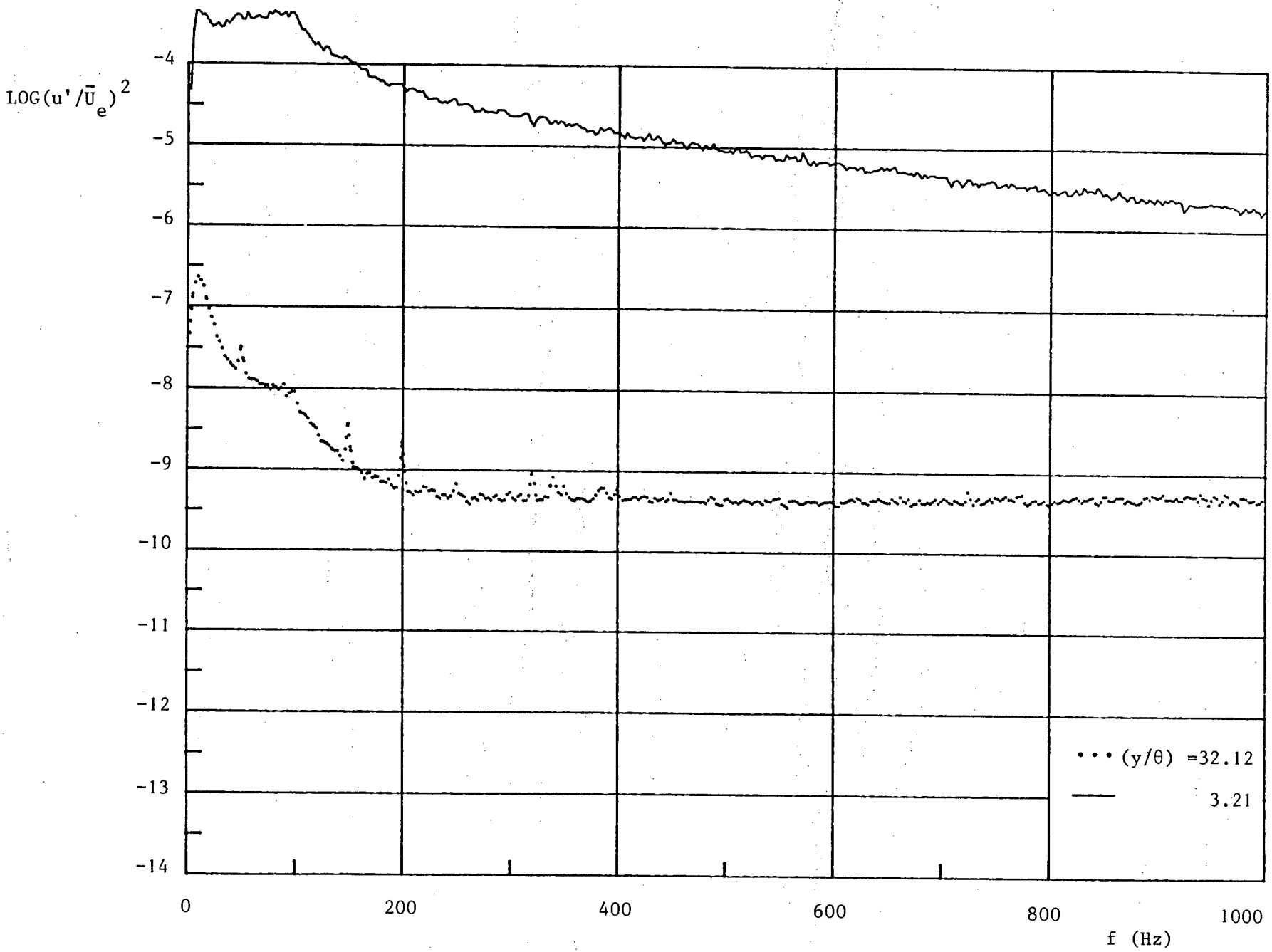

Figure 6.11p : Continued, x = 804 mm.

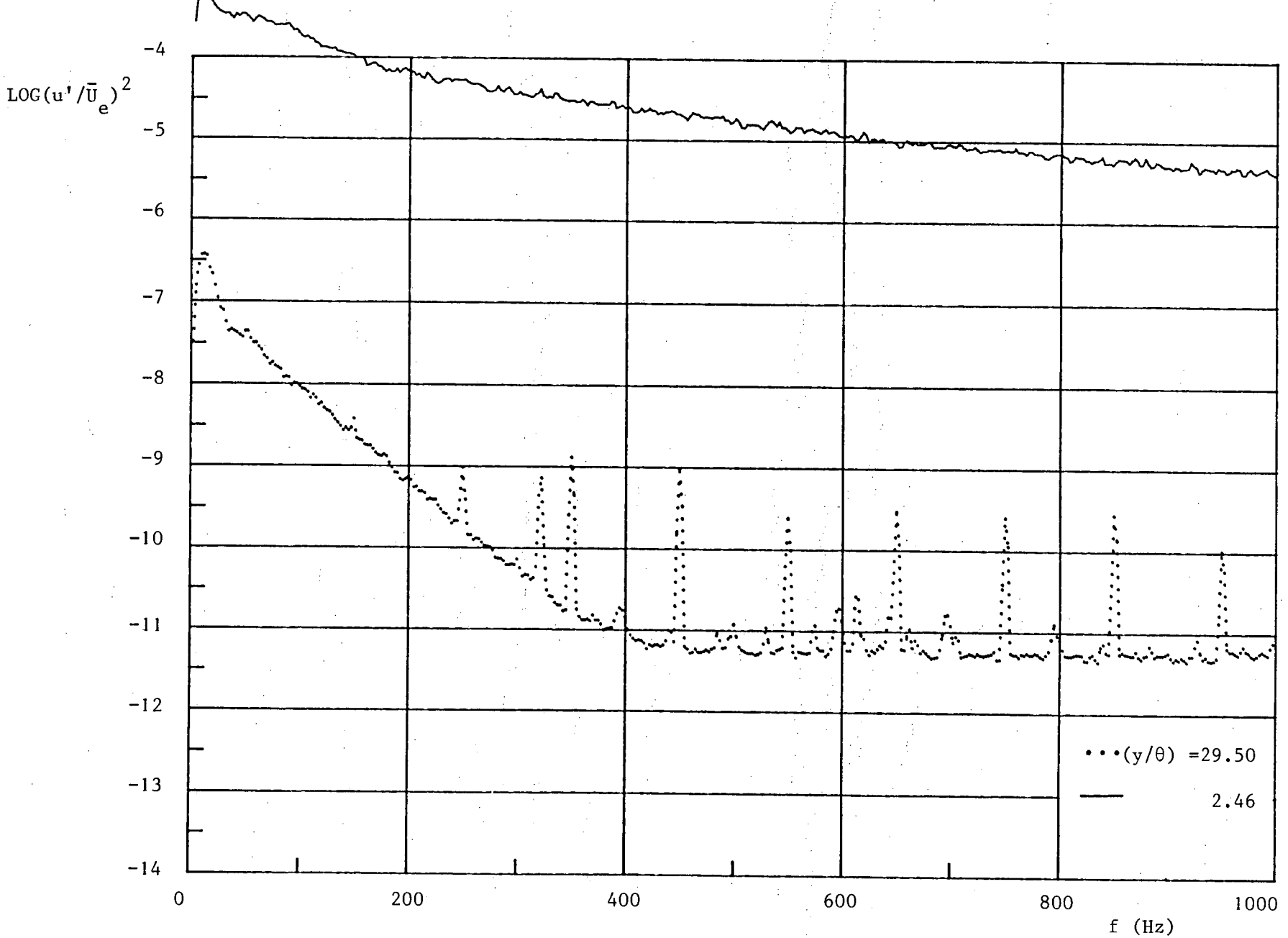

Figure 6.11q : Continued, x = 854 mm.

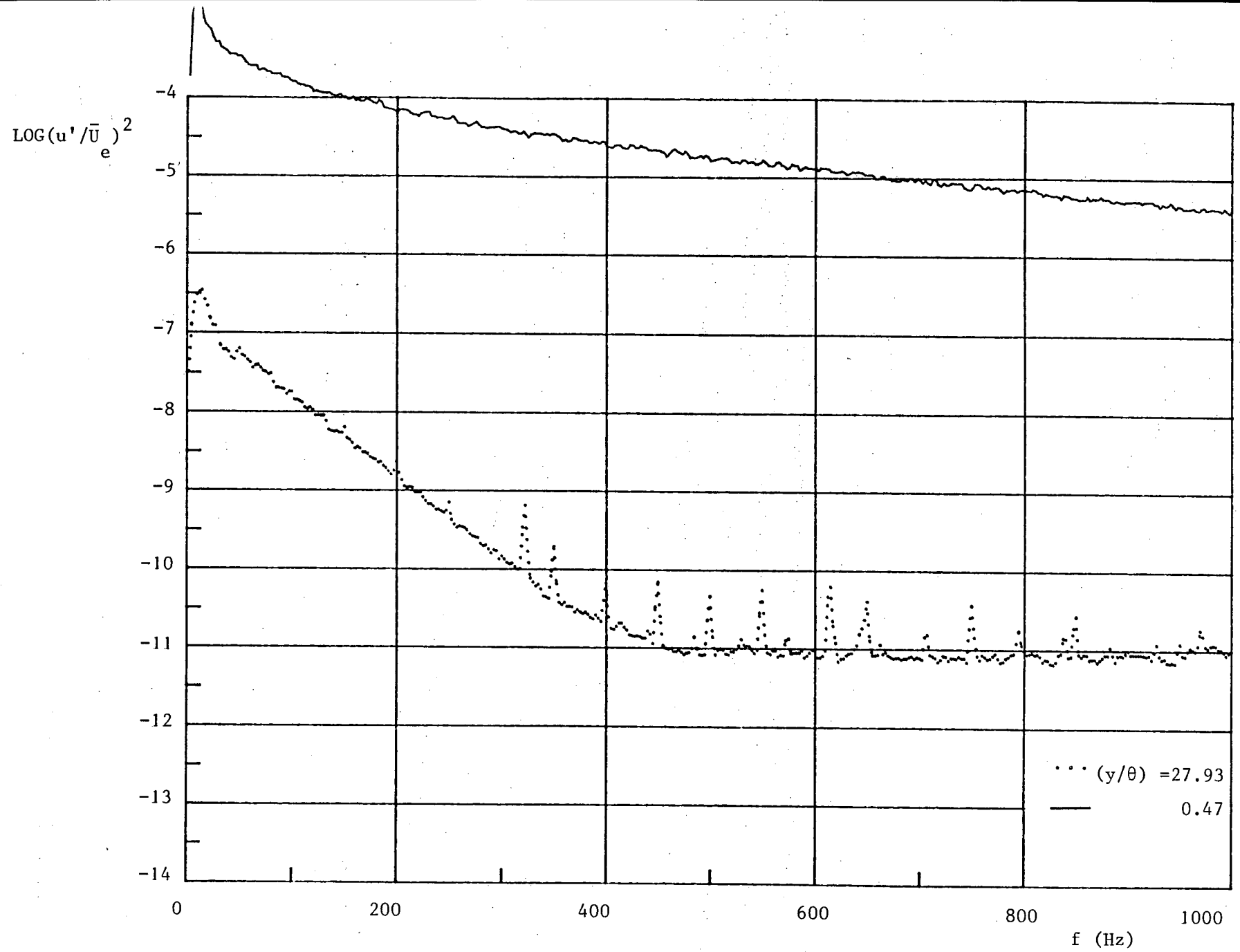

Figure 6.11r : Continued, x = 872 mm.

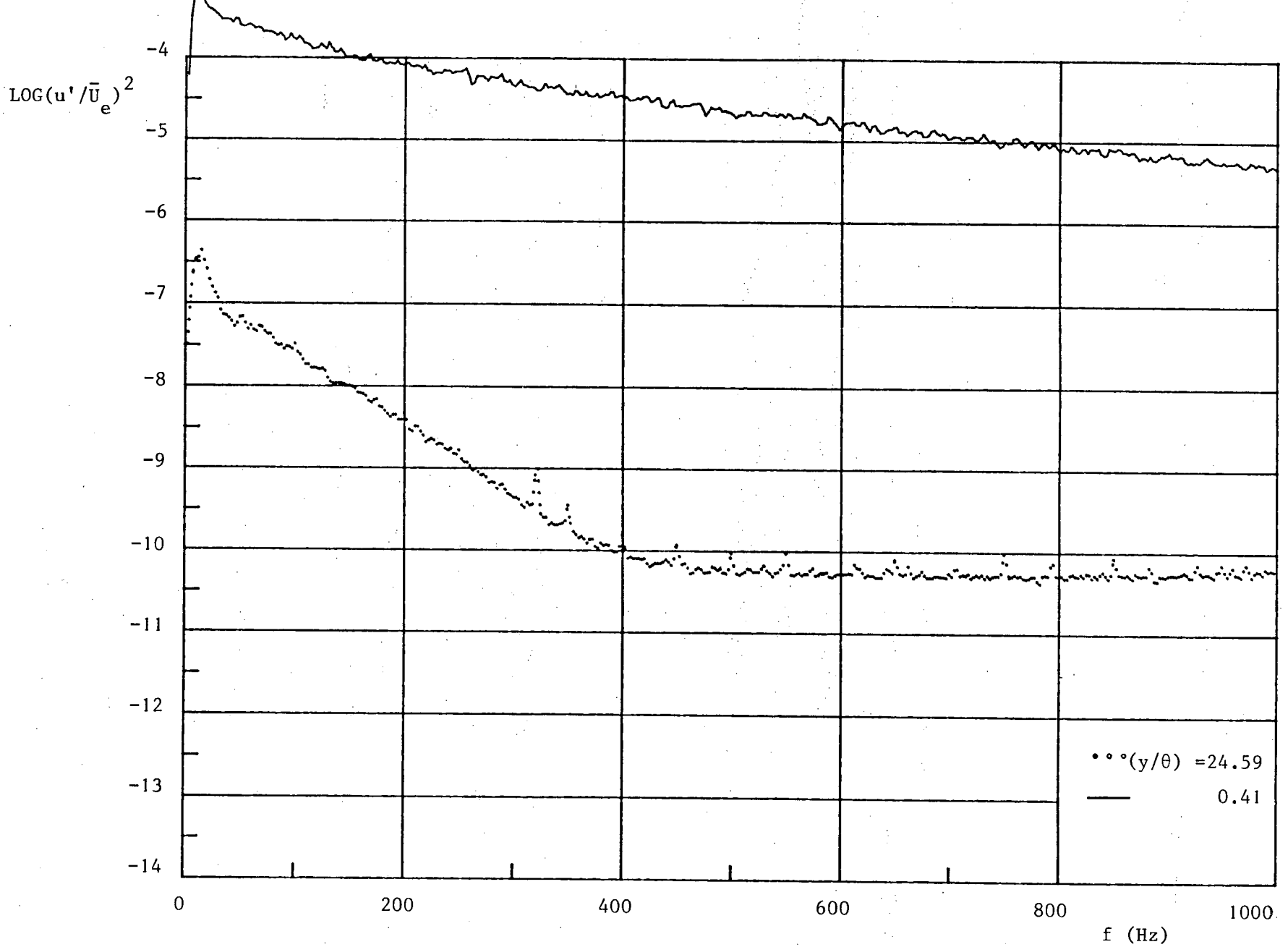

Figure 6.11s : Continued, x = 931 mm.

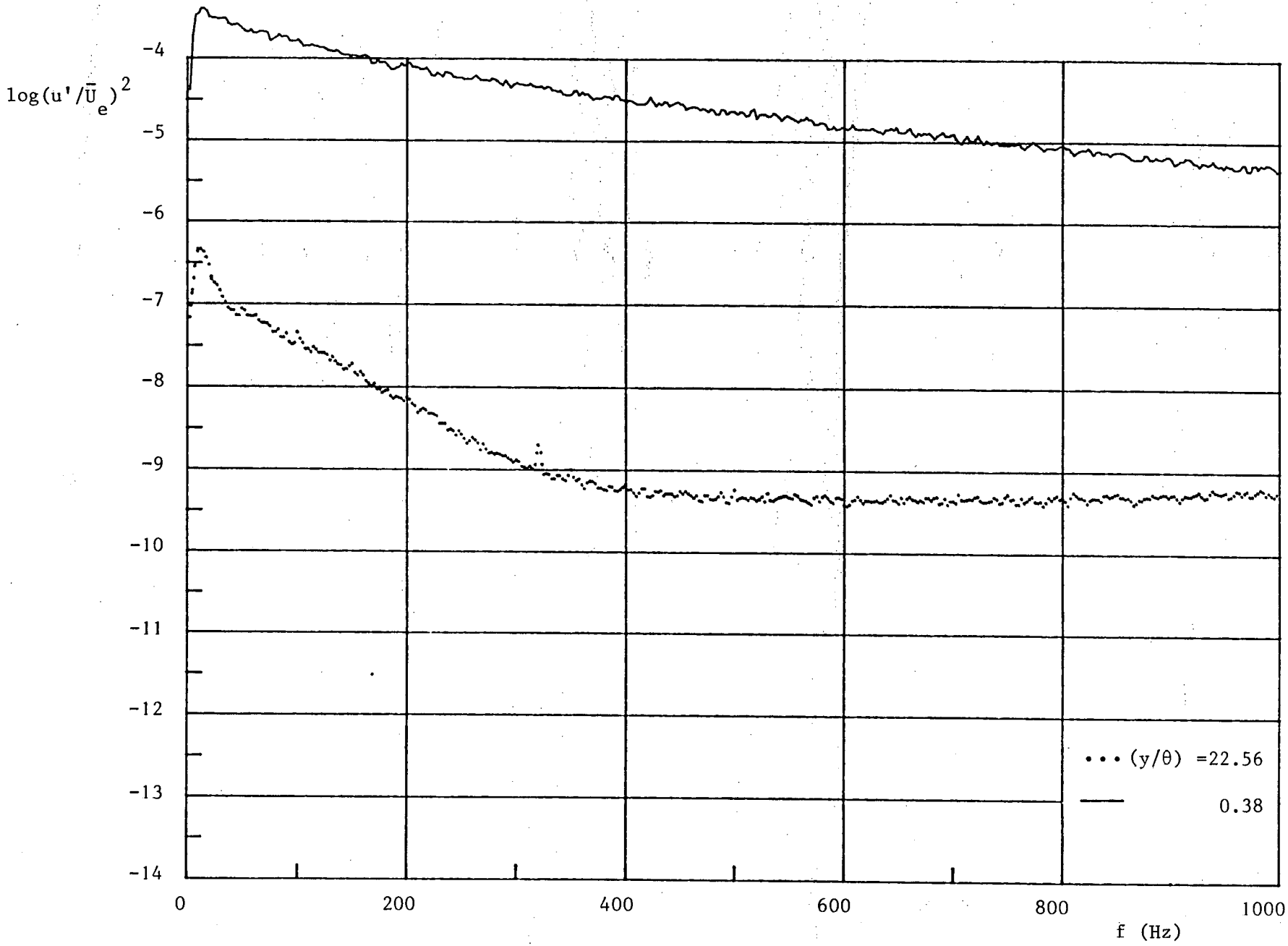

Figure 6.11t : Continued, x = 966 mm.

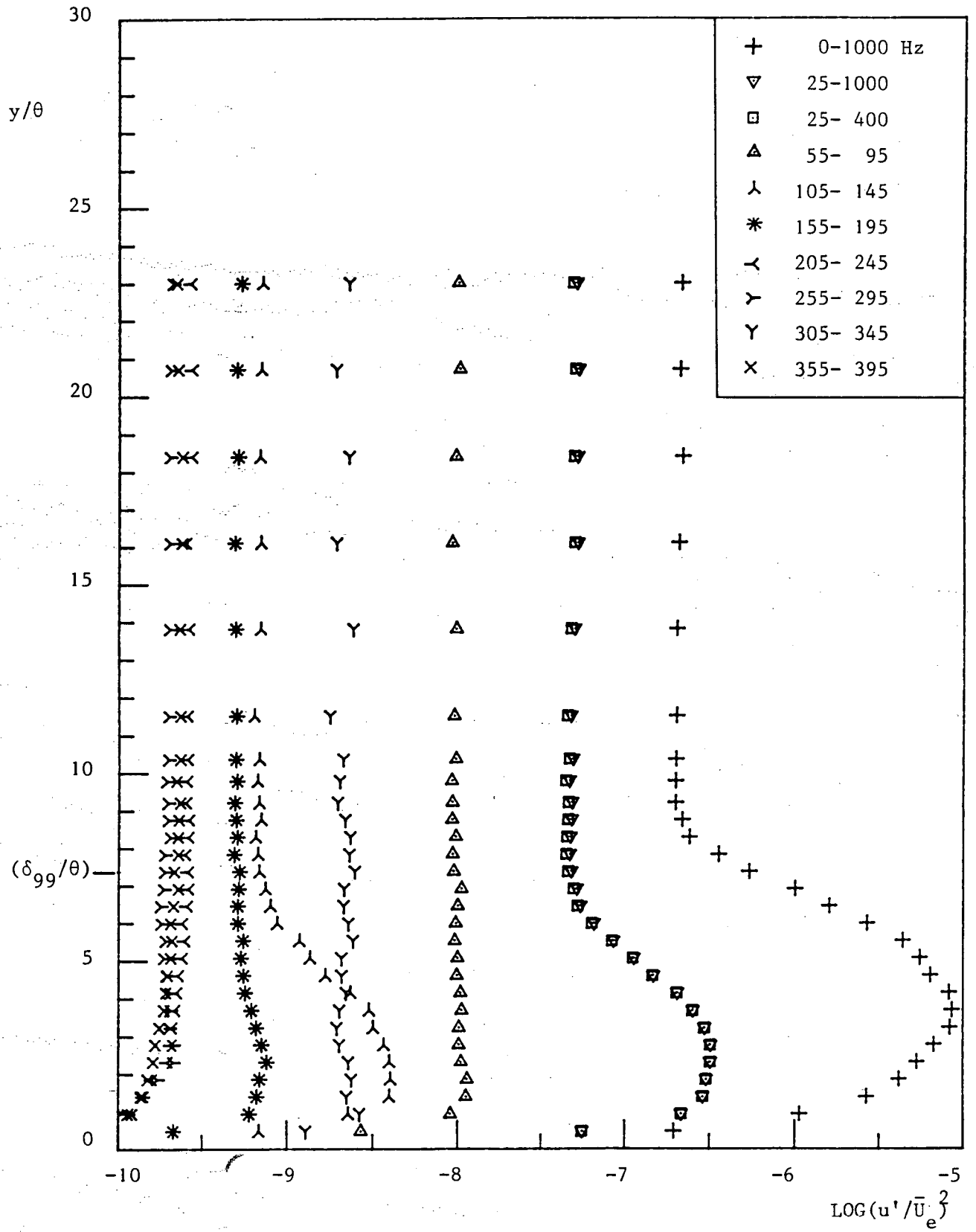

Figure 6.12 : Power distributions across the boundary layer in several frequency bands, x = 276 mm.

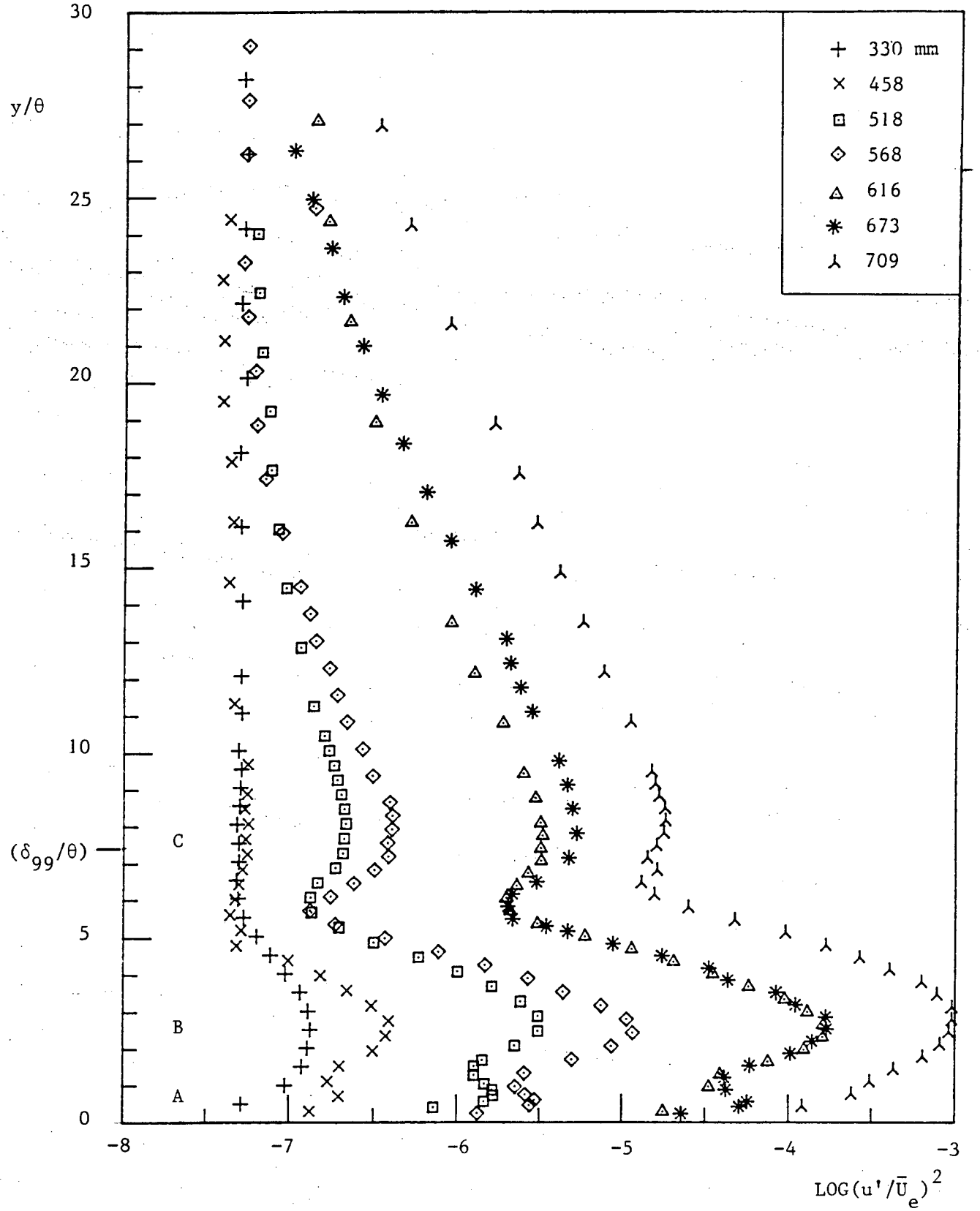

Figure 6.13 : Power distributions across the boundary layer at several streamwise stations, in the frequency band 25-200 Hz.

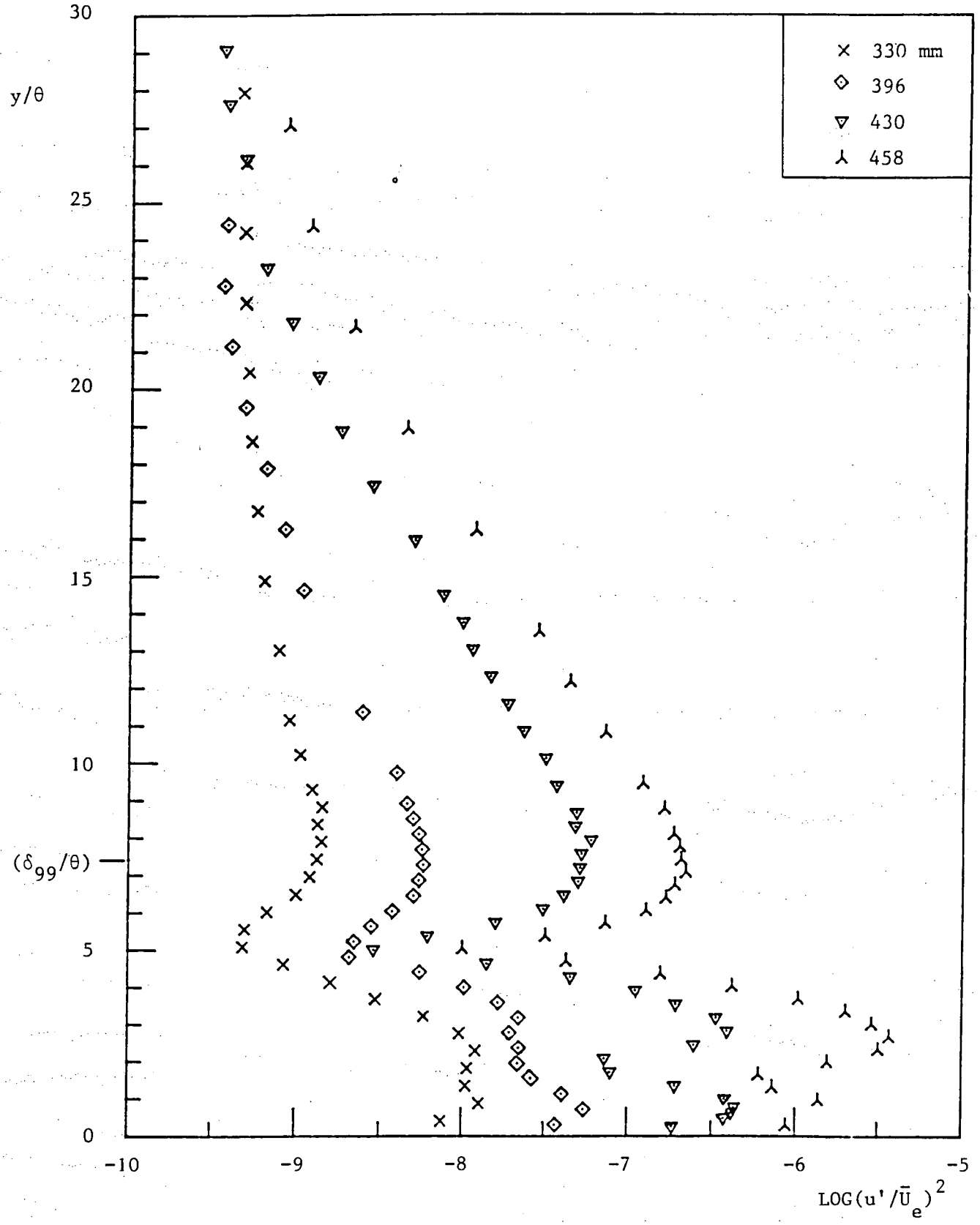

Figure 6.14a : Power distributions across the boundary layer at several streamwise stations, in the frequency band 155-195 Hz.

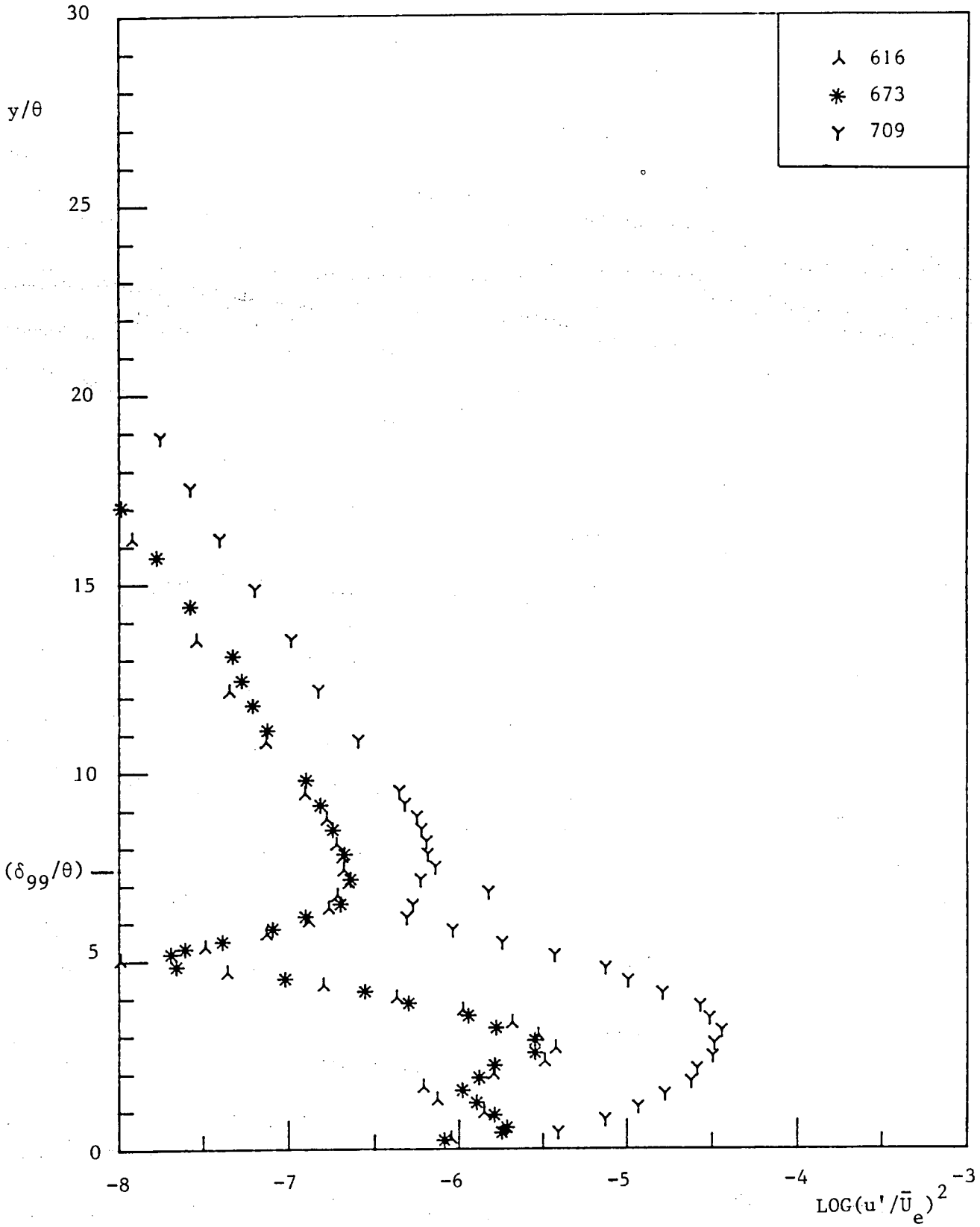

Figure 6.14b : Continued.

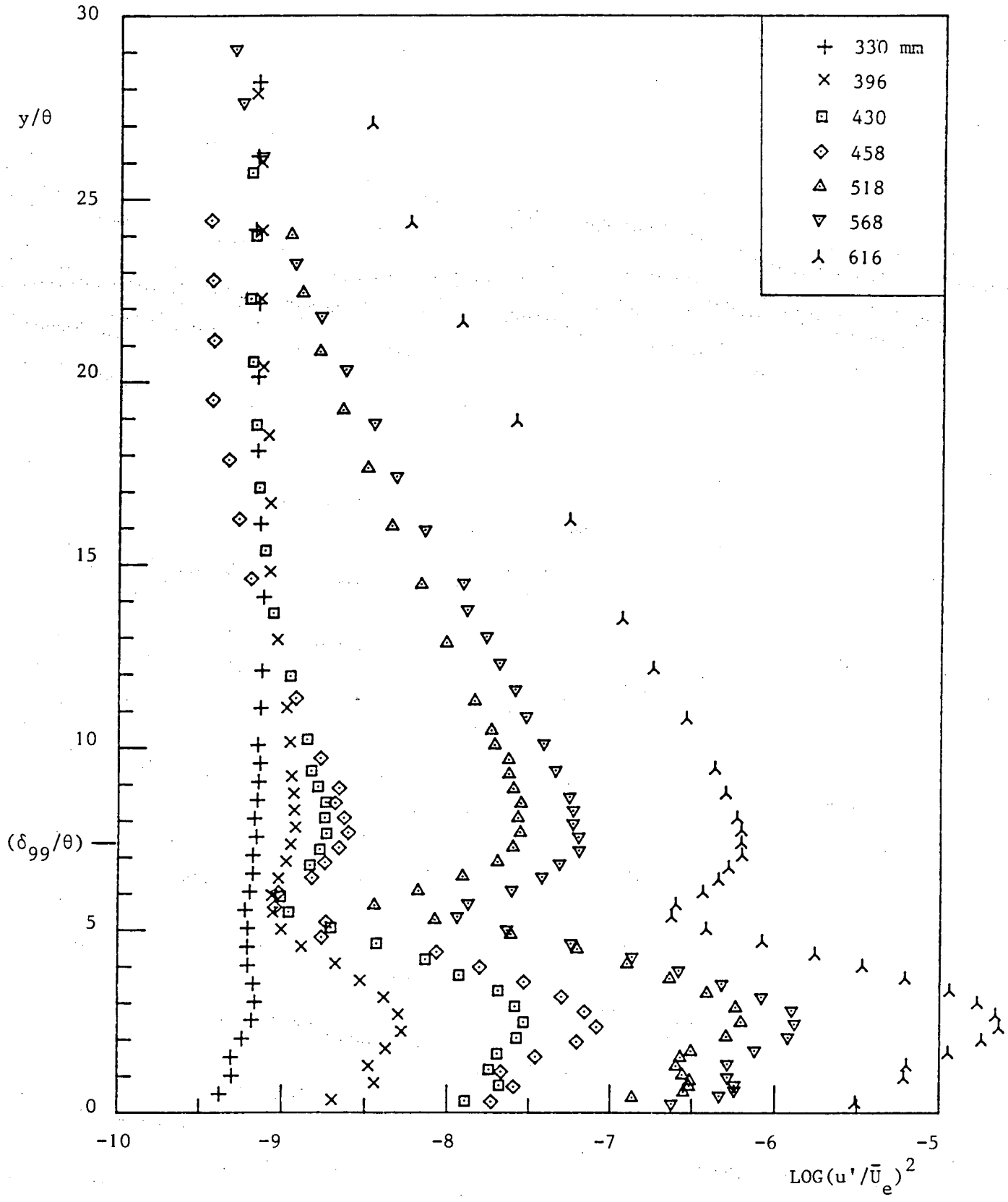

Figure 6.15a : Power distributions across the boundary layer at several streamwise stations, in the frequency band 105-145 Hz.

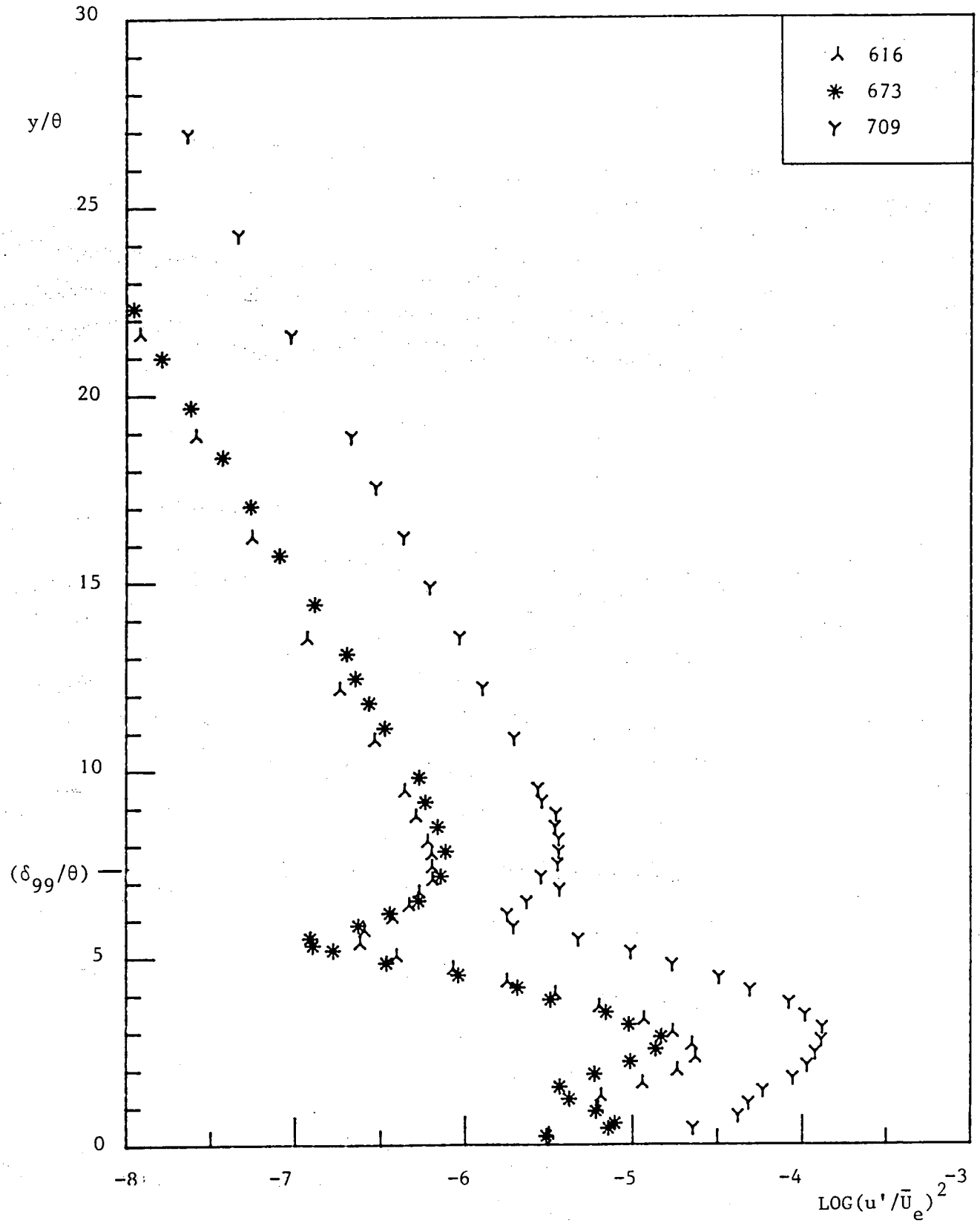

Figure 6.15b : Continued.

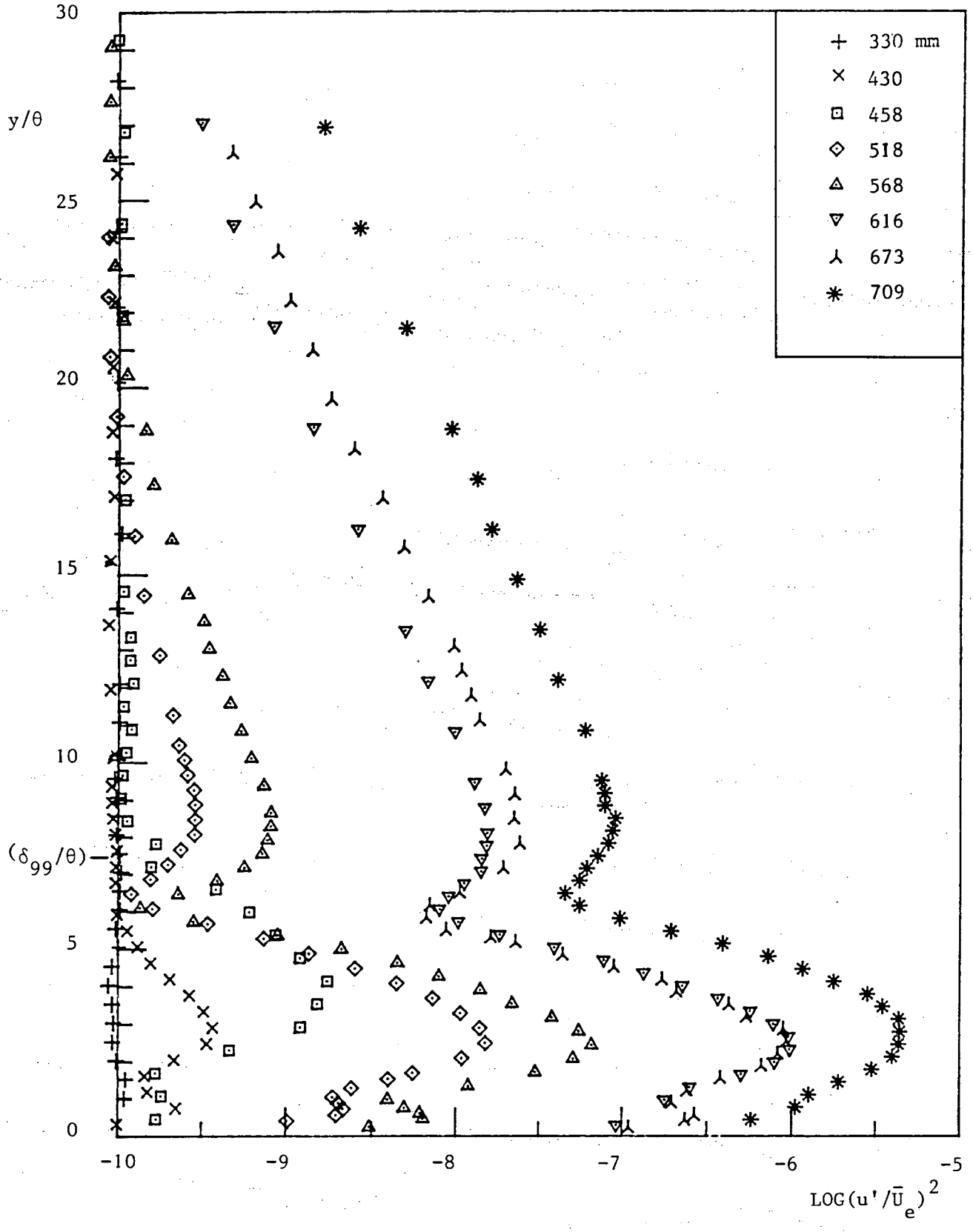

Figure 6.16 : Power distributions across the boundary layer at several streamwise stations, in the frequency band 55-95 Hz.

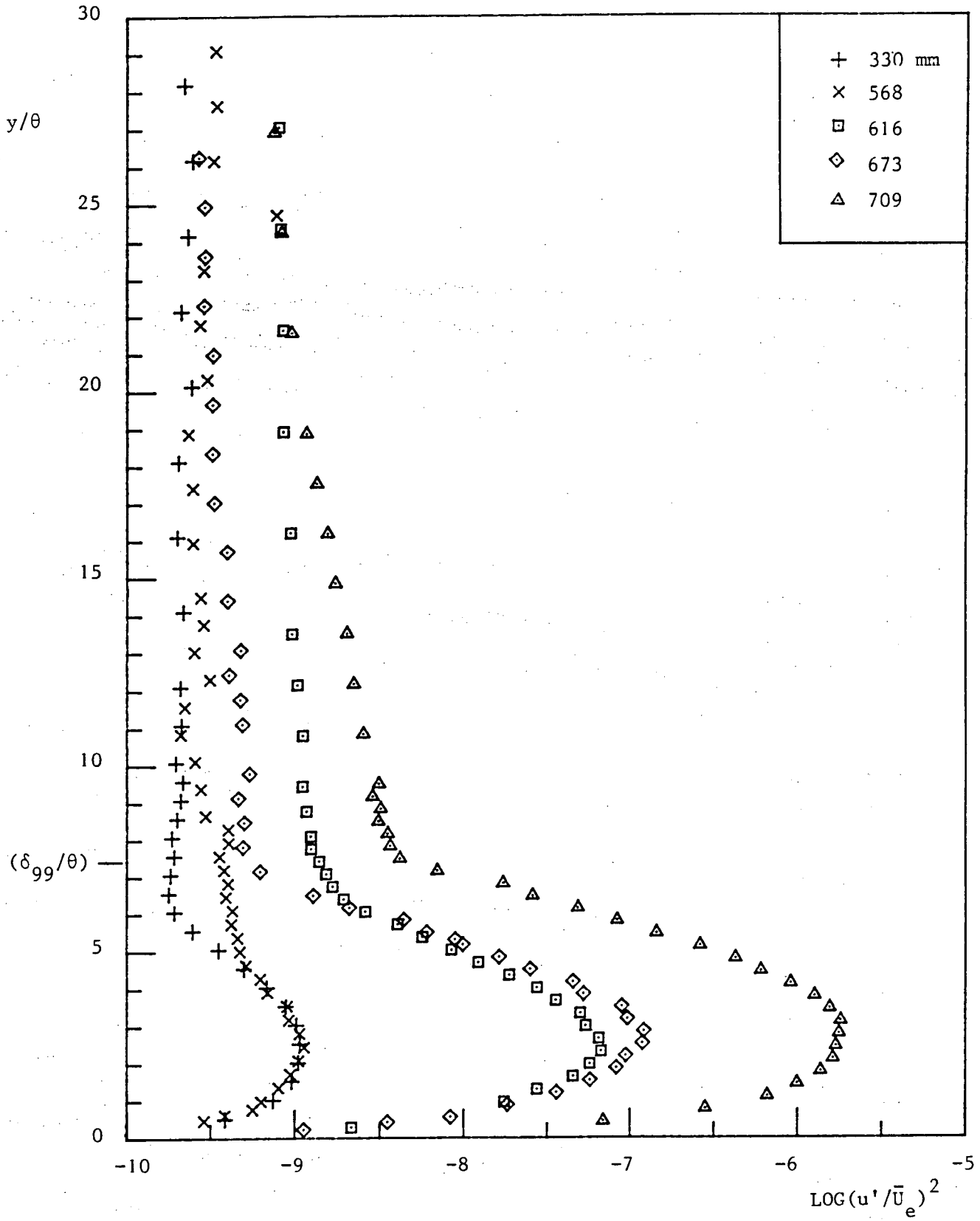

Figure 6.17 : Power distributions across the boundary layer at several streamwise stations, in the frequency band 25-45 Hz.

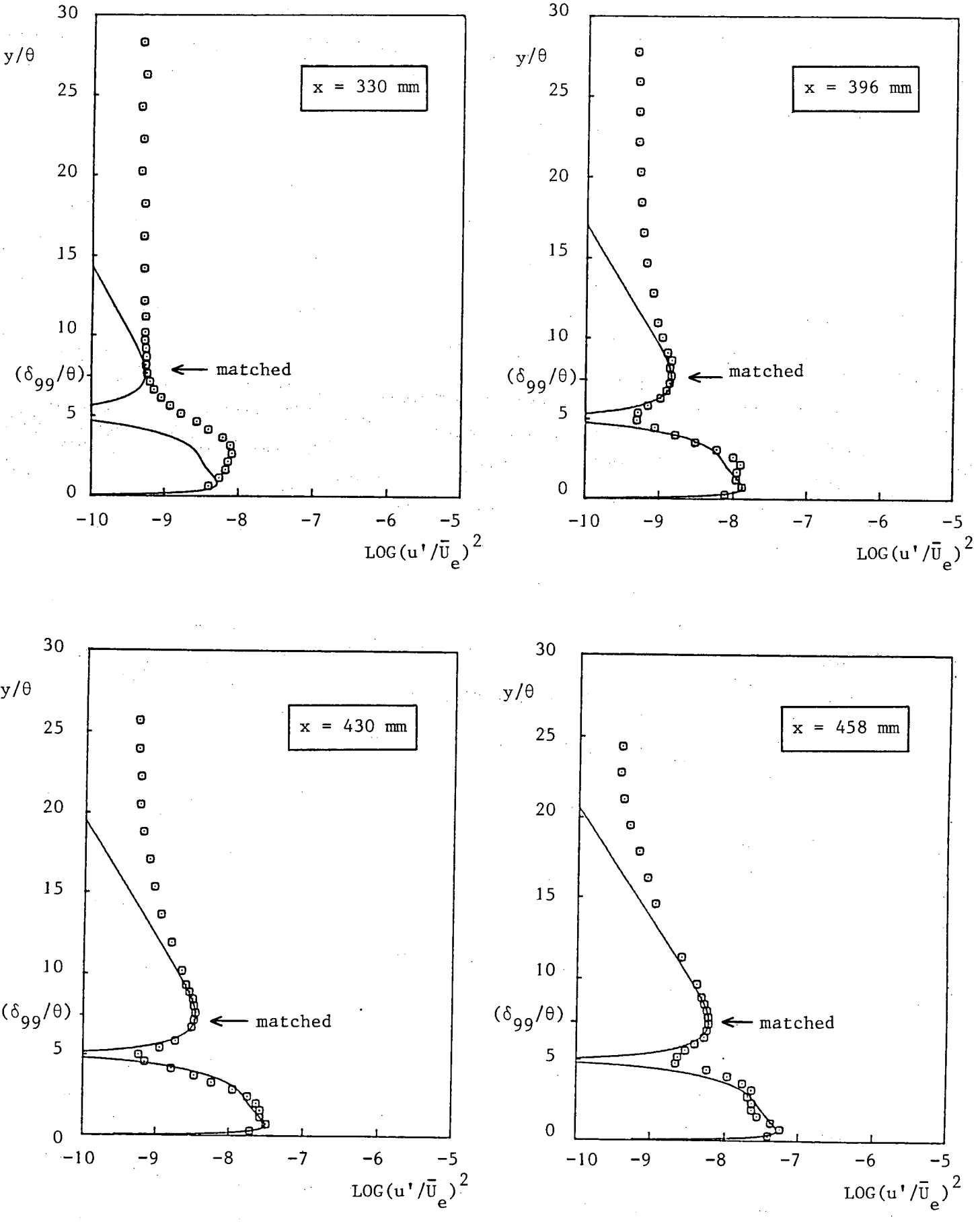

Figure 6.18a : Development of experimental power distribution (⊙,155-195 Hz) compared with matched Cosal results (—,175 Hz).

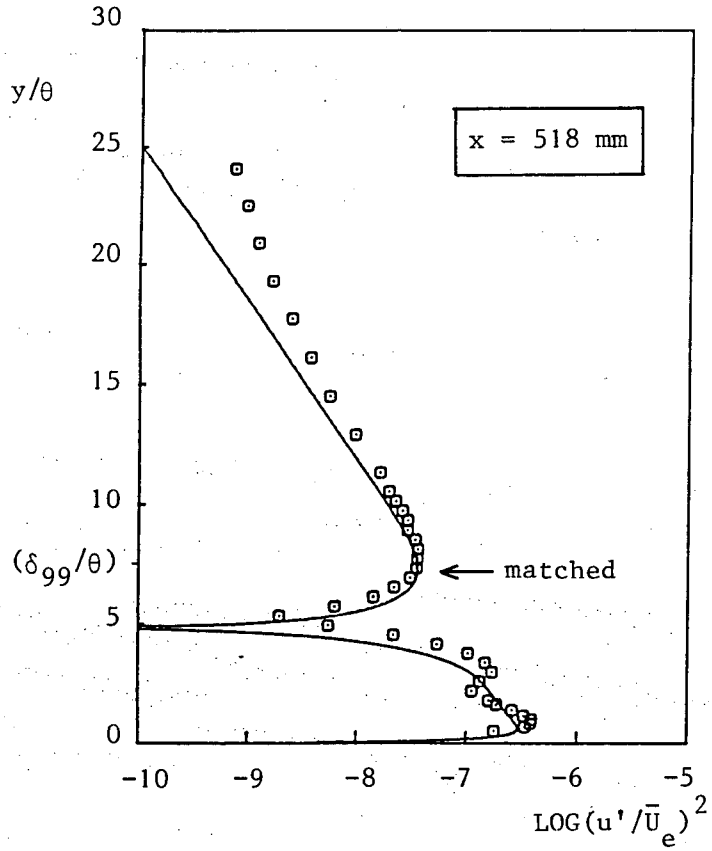

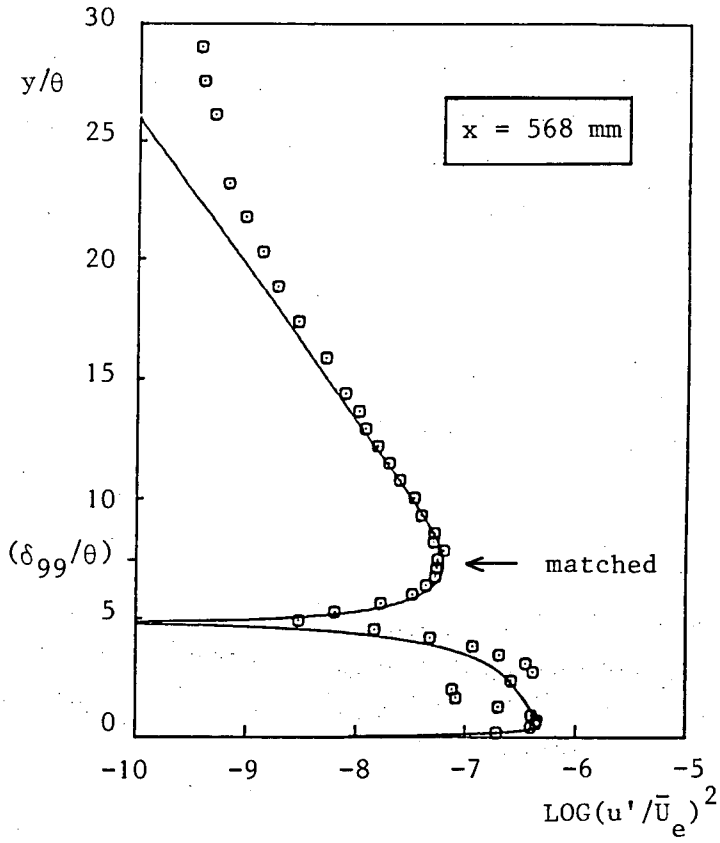

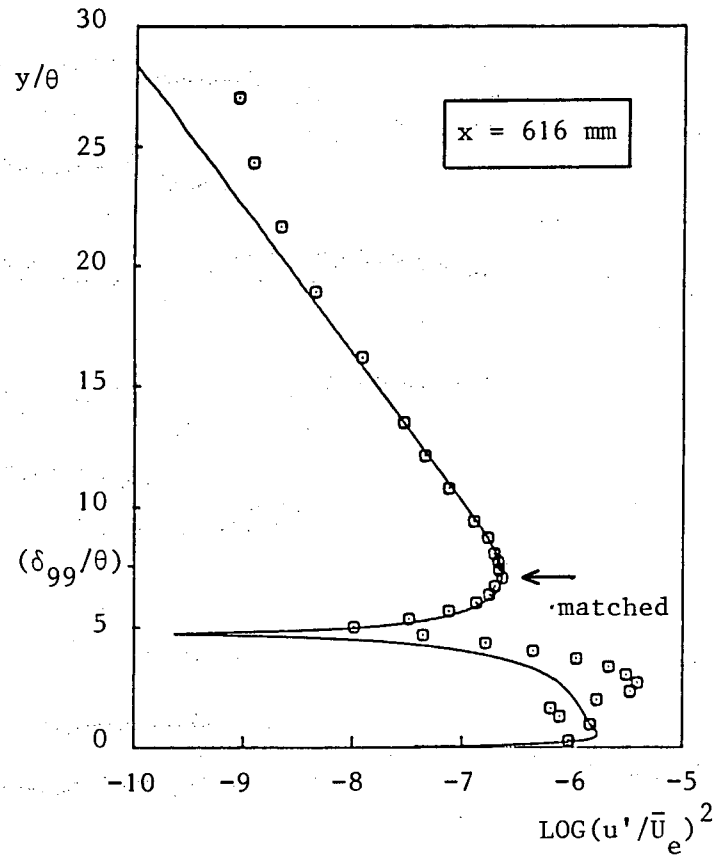

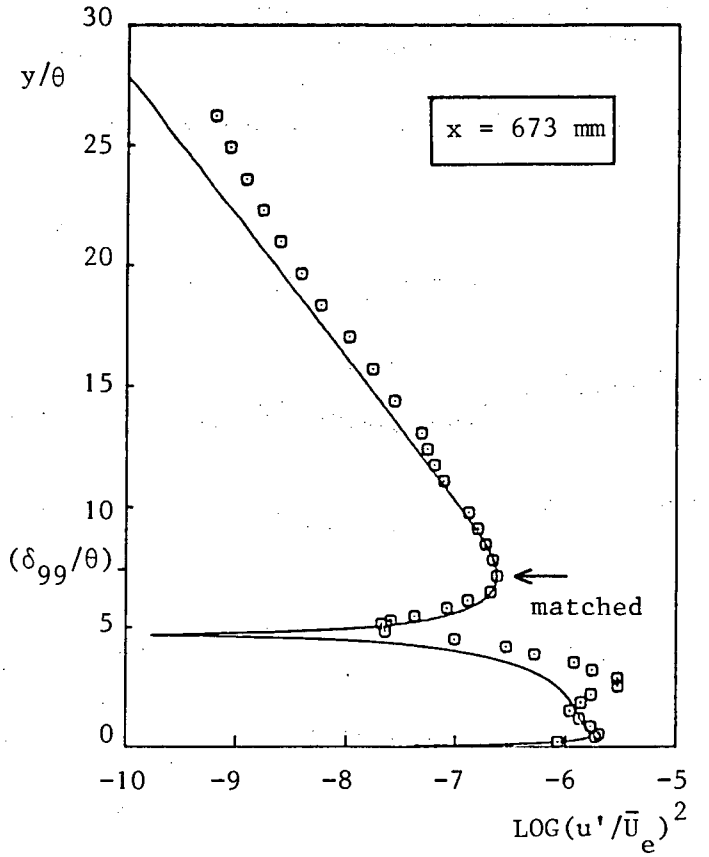

Figure 6.18b : Continued.

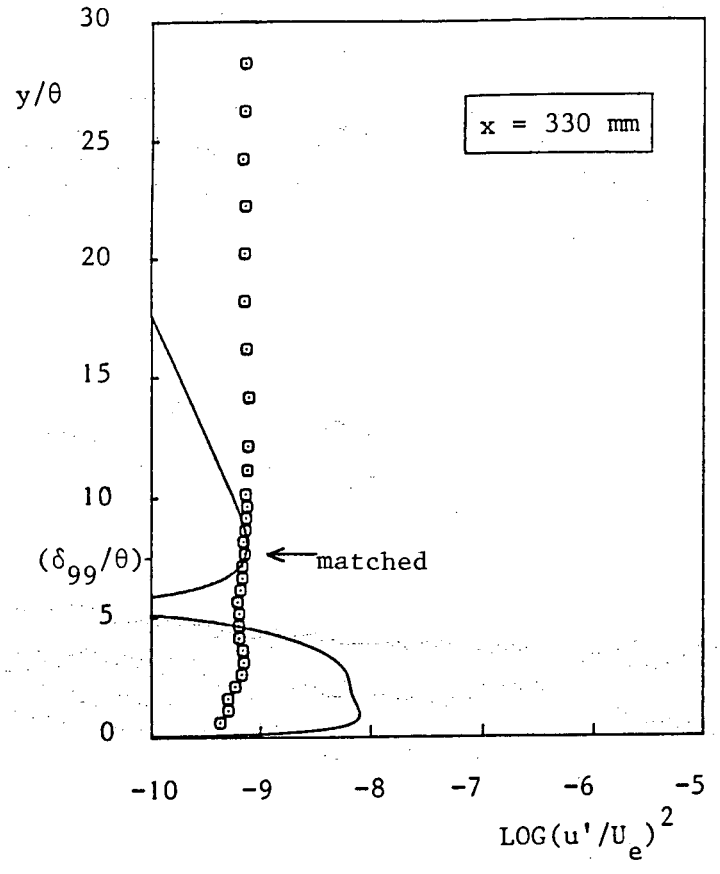

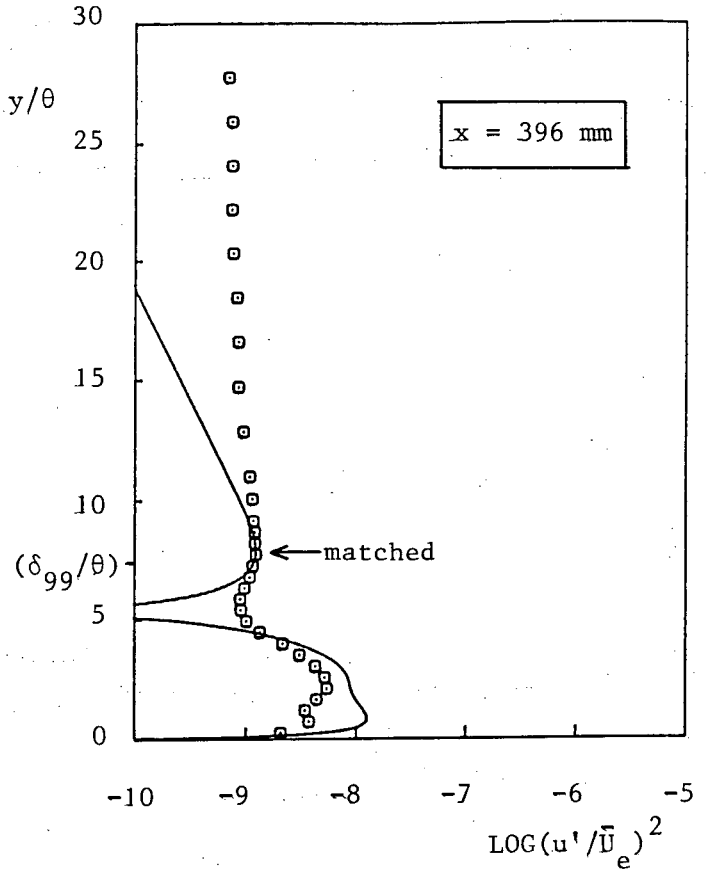

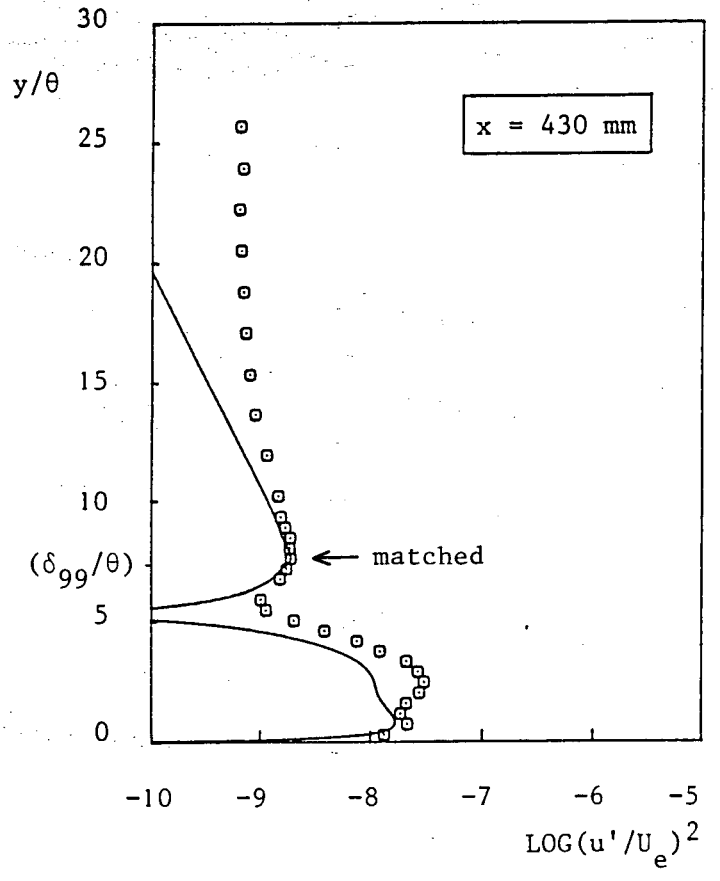

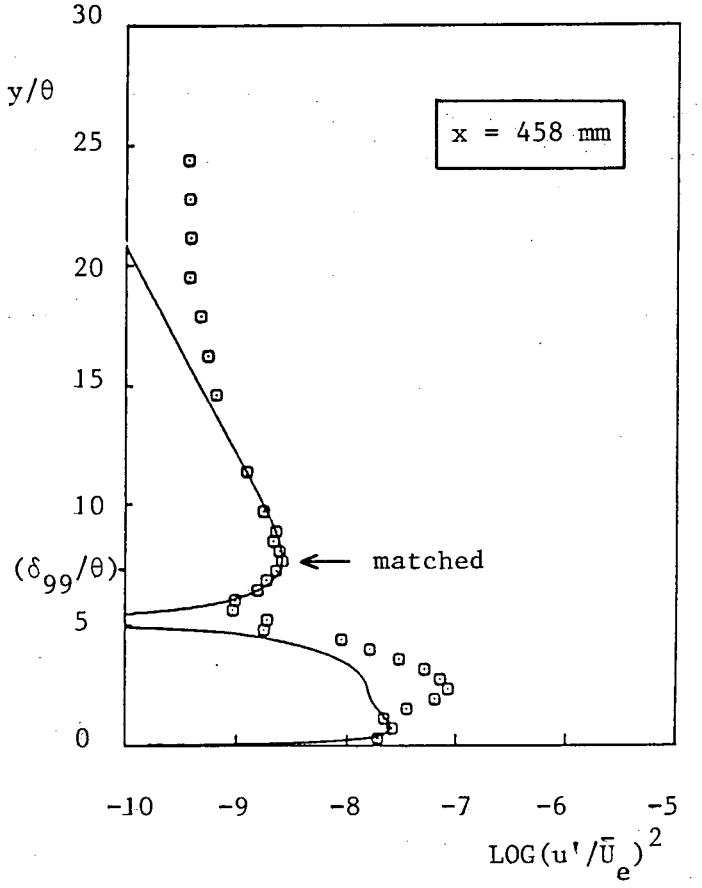

Figure 6.19a : Development of experimental power distribution (⊙,105-145 Hz) compared with matched Cosal results (—,130 Hz)

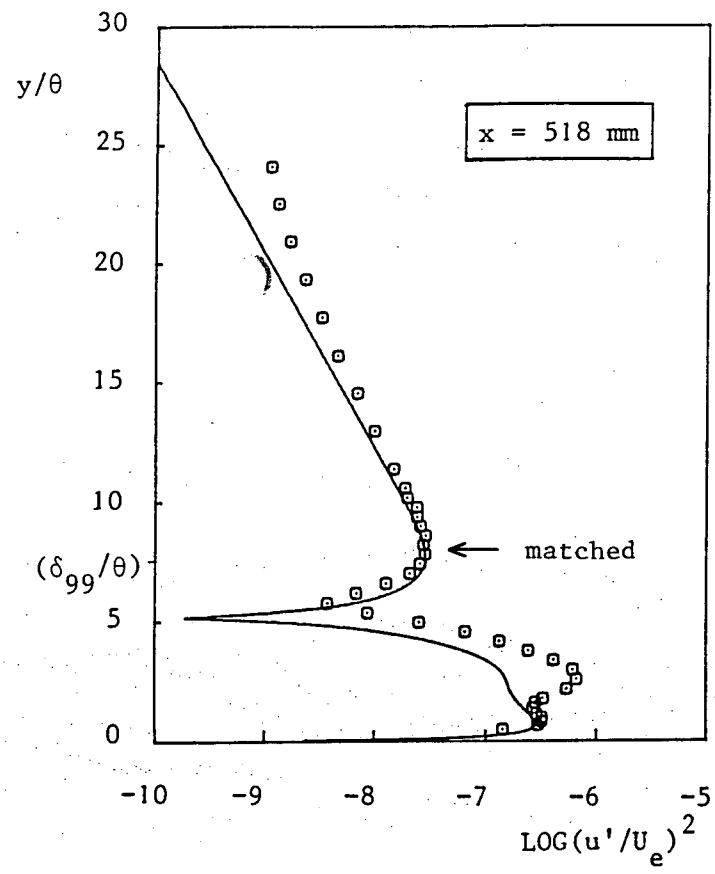

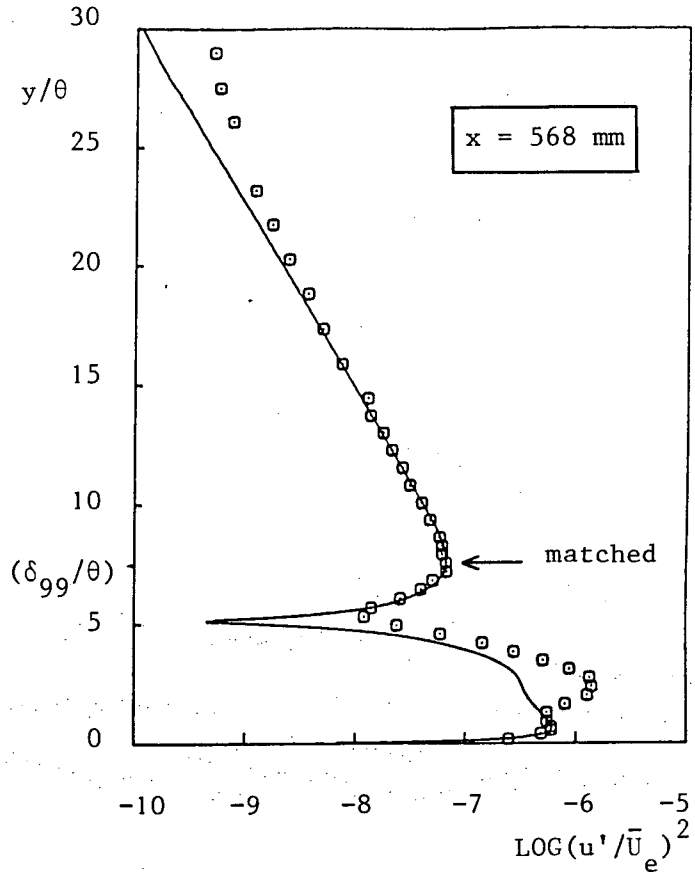

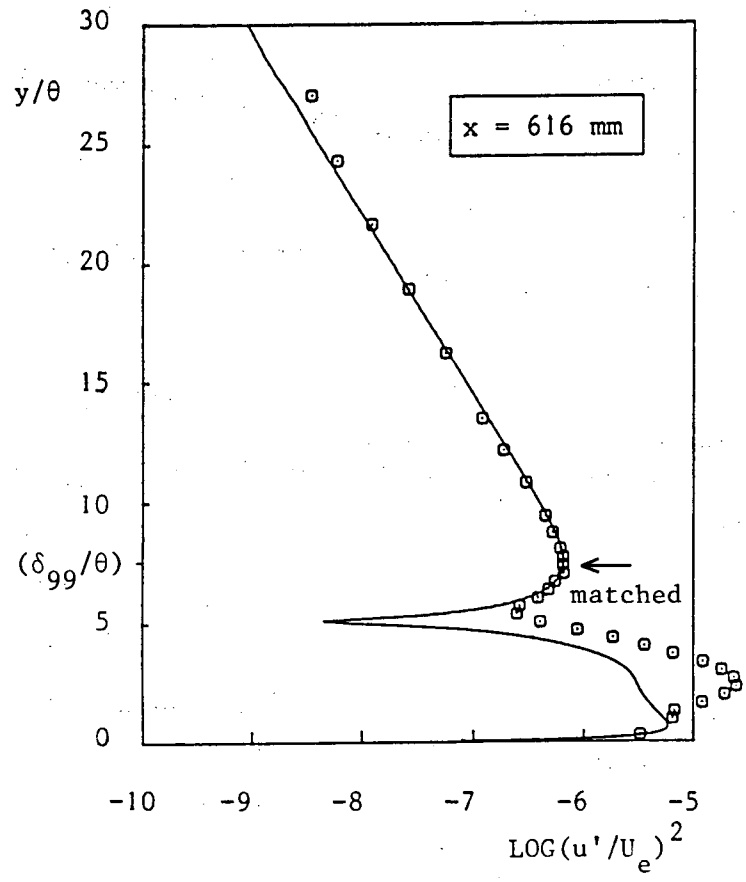

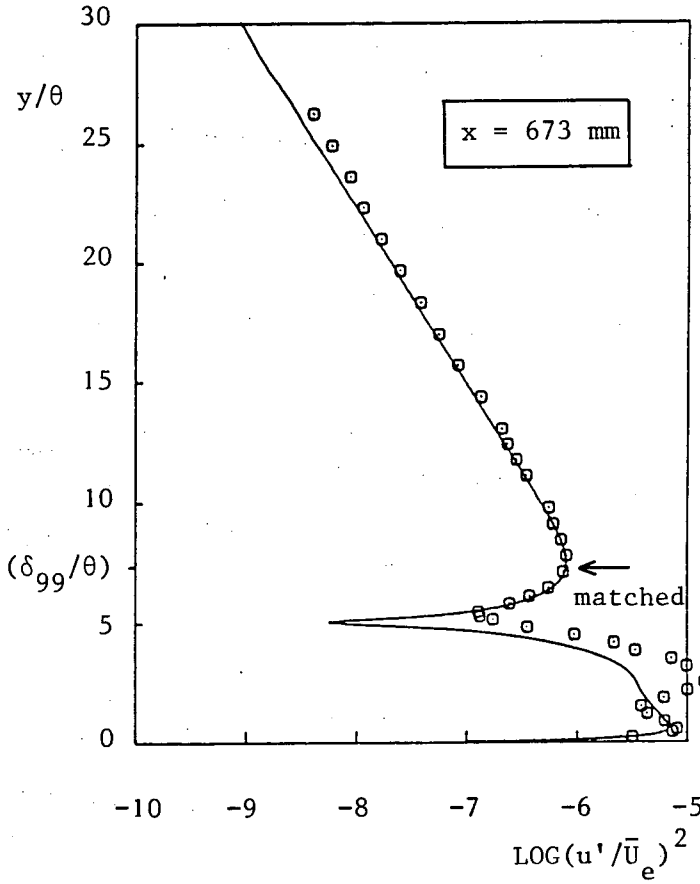

Figure 6.19b : Continued.

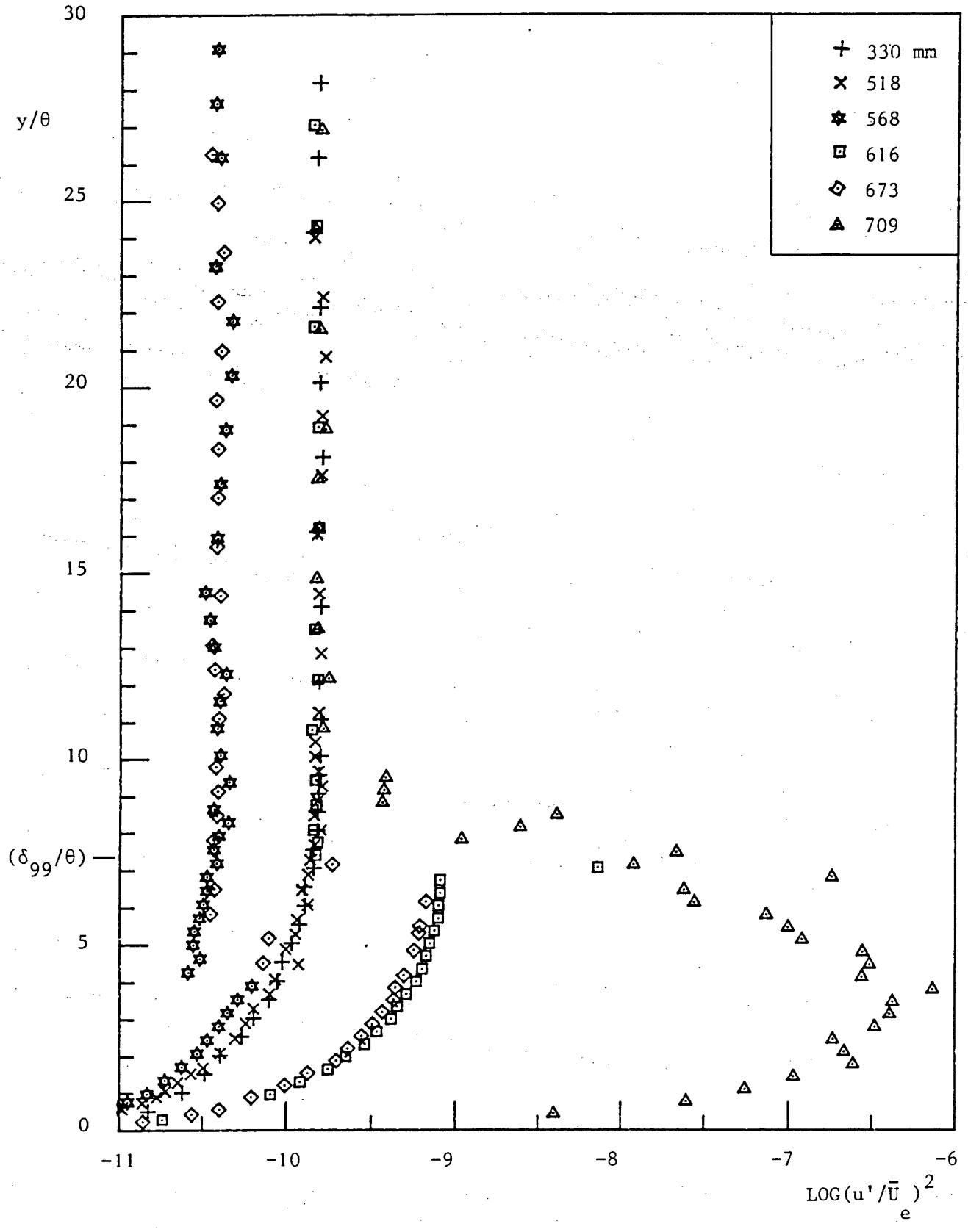

Figure 6.20 : Development of experimental power distribution (505-545 Hz).

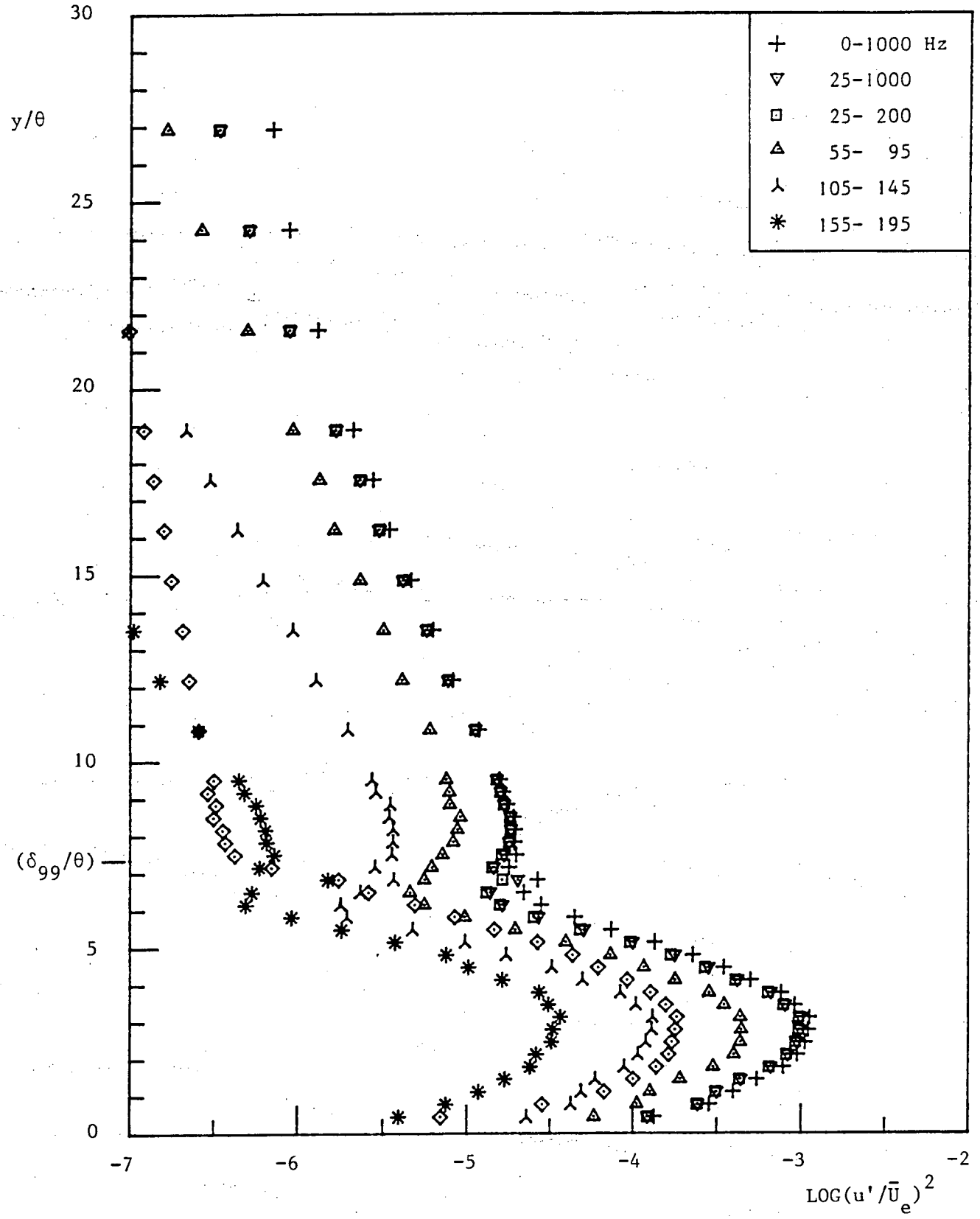

Figure 6.21a : Power distributions across the boundary layer in several frequency bands, x = 709 mm.

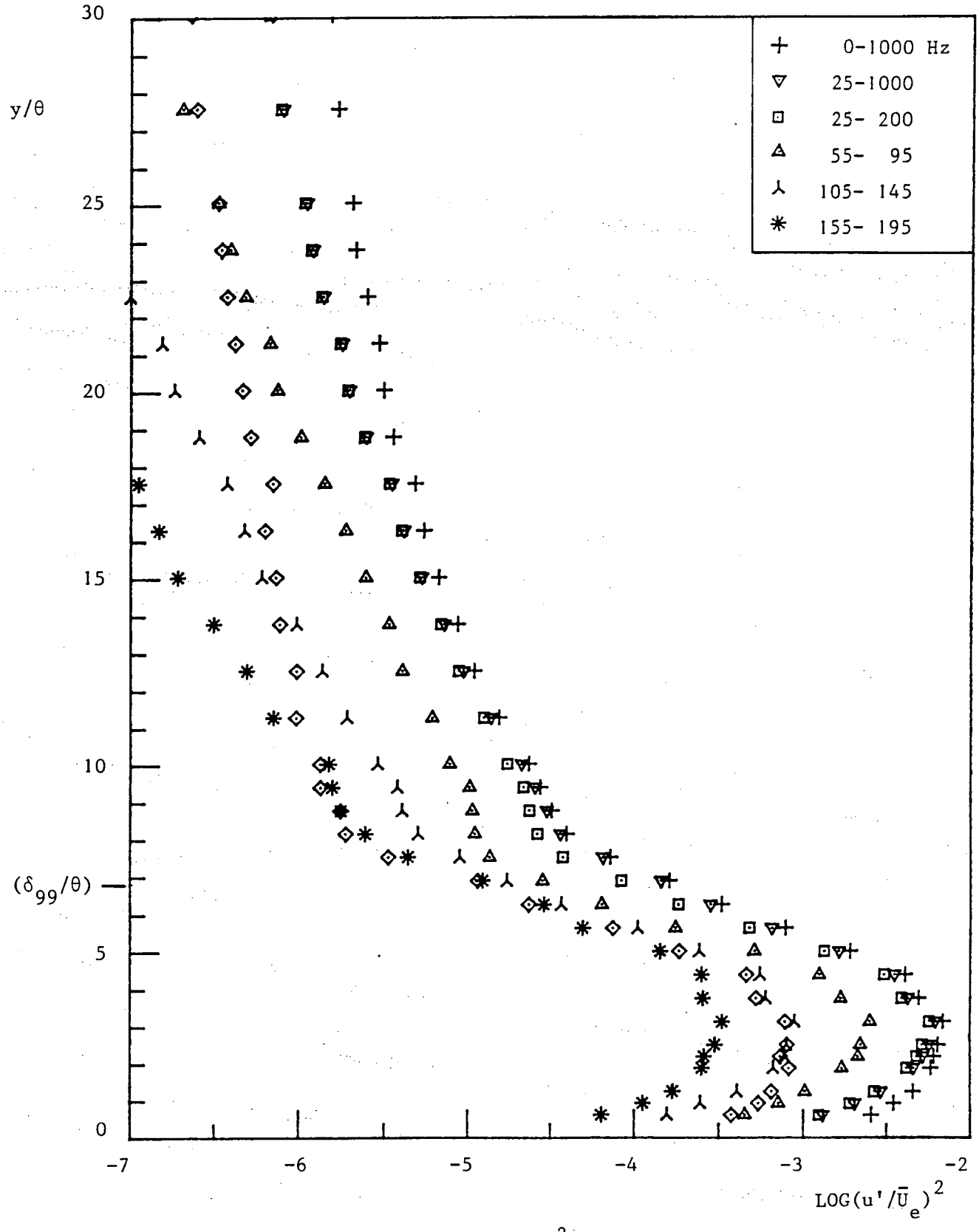

Figure 6.21b : Continued, x = 741^2 mm.

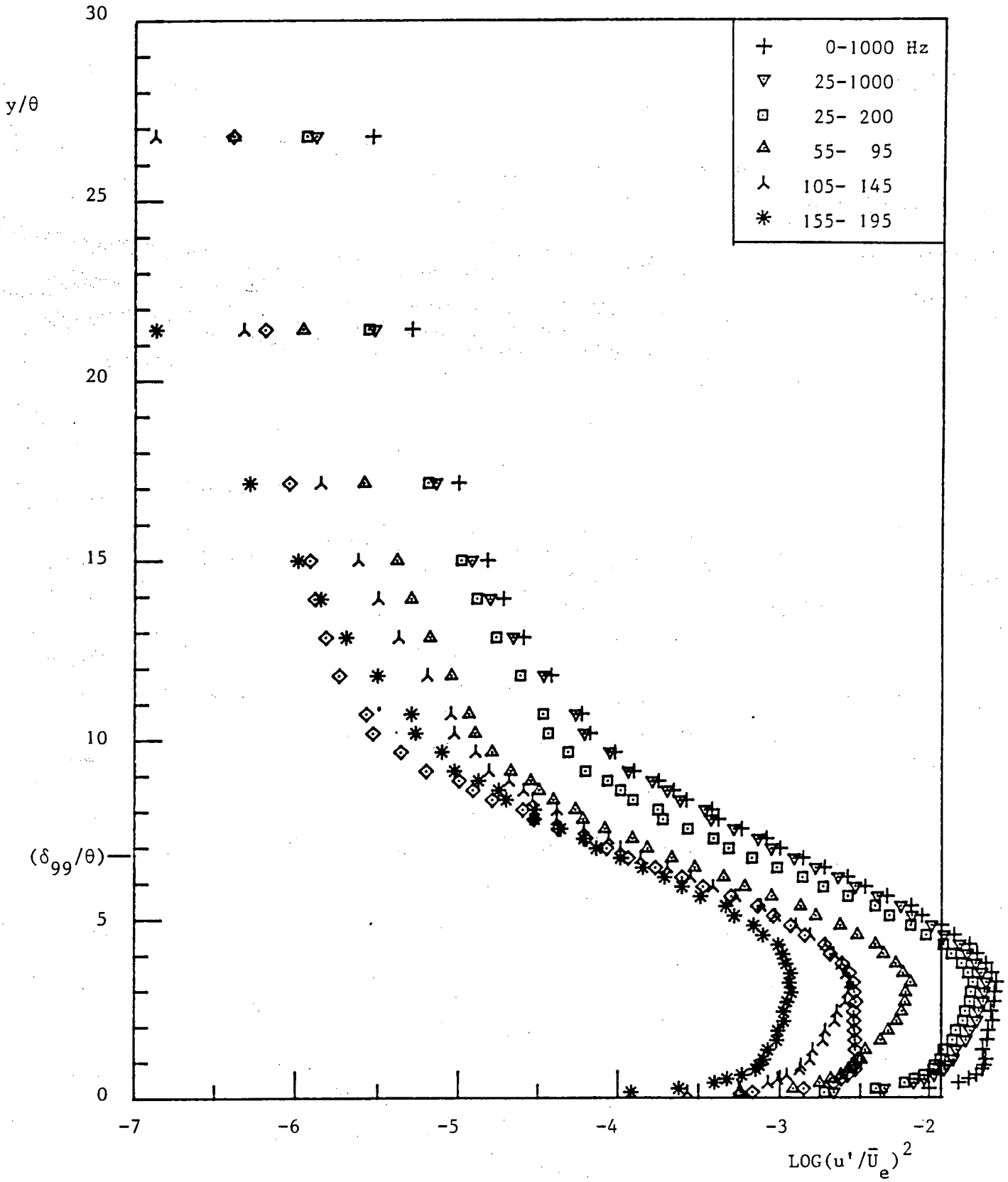

Figure 6.21c : Continued, x = 804 mm.

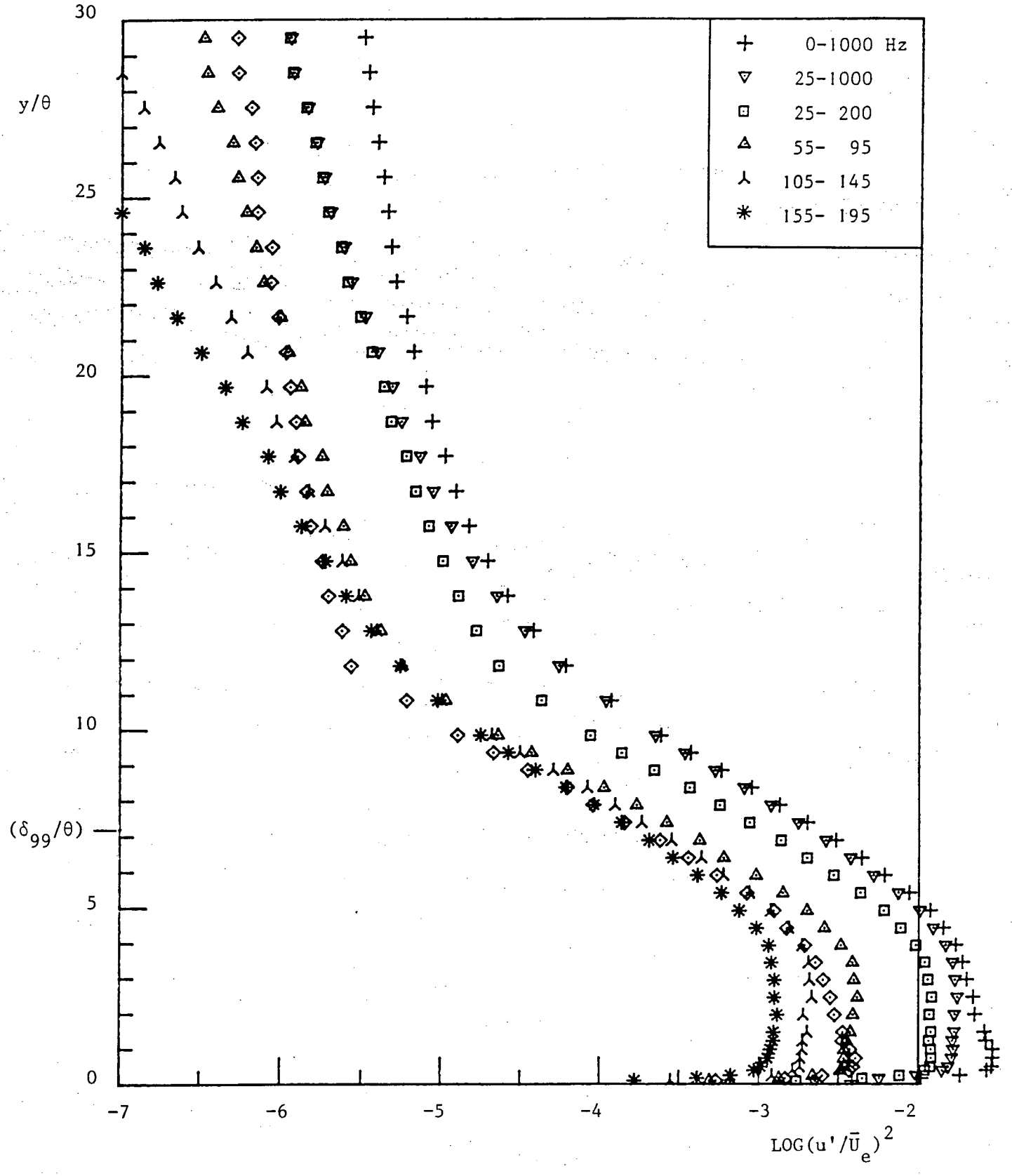

Figure 6.21d : Continued, x = 854 mm.

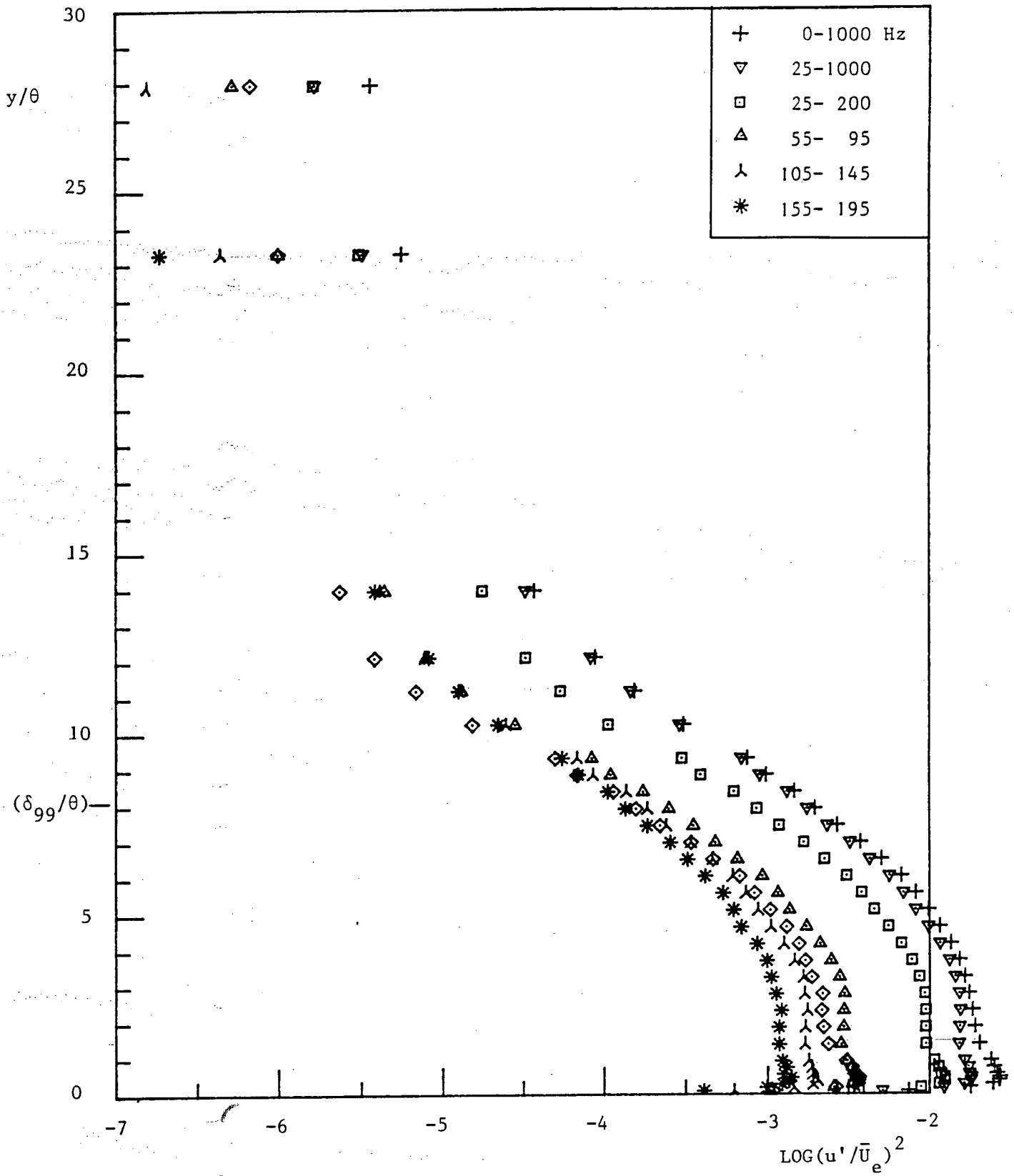

Figure 6.21e : Continued, x = 872 mm.

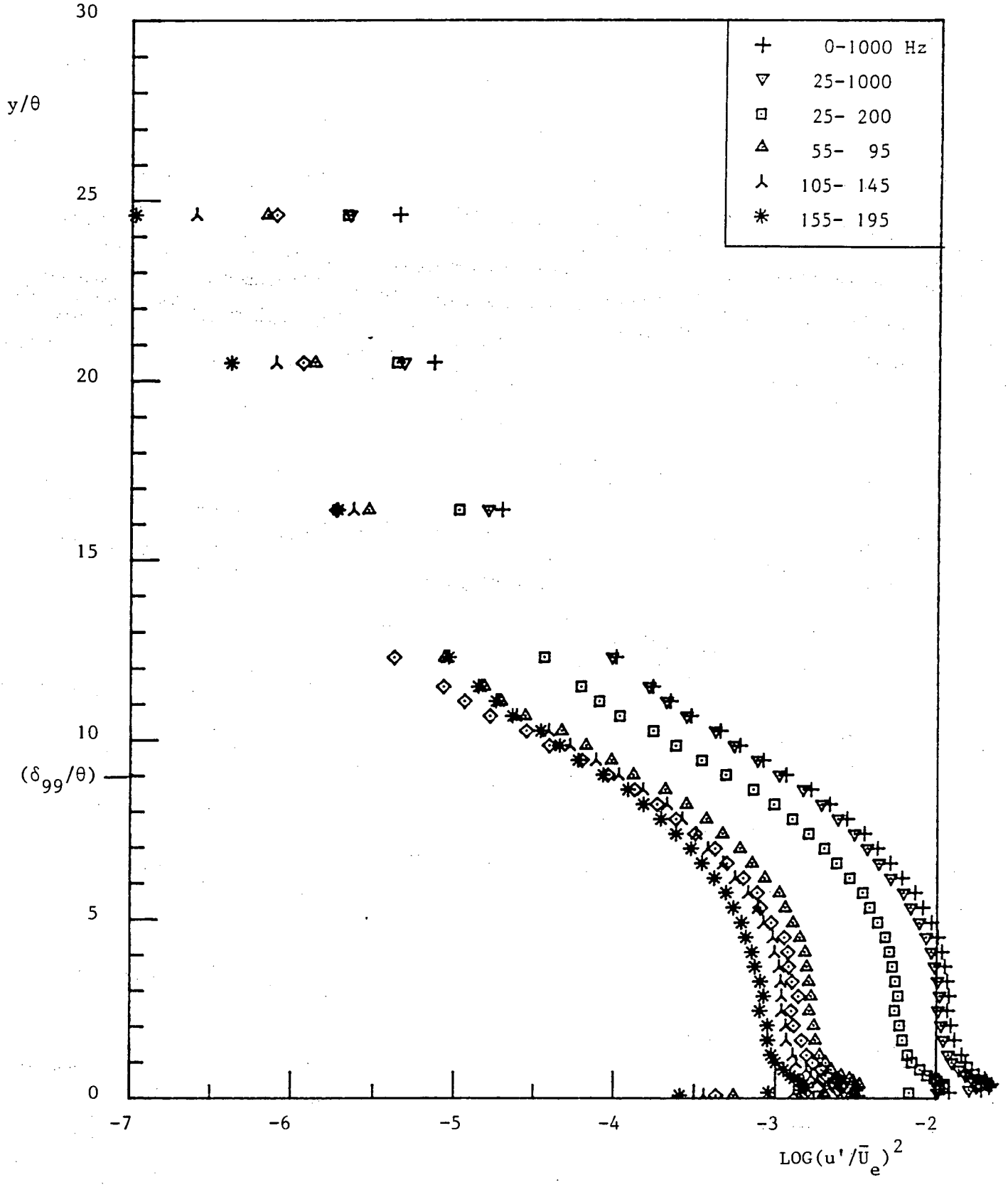

Figure 6.21f : Continued, x = 931 mm.

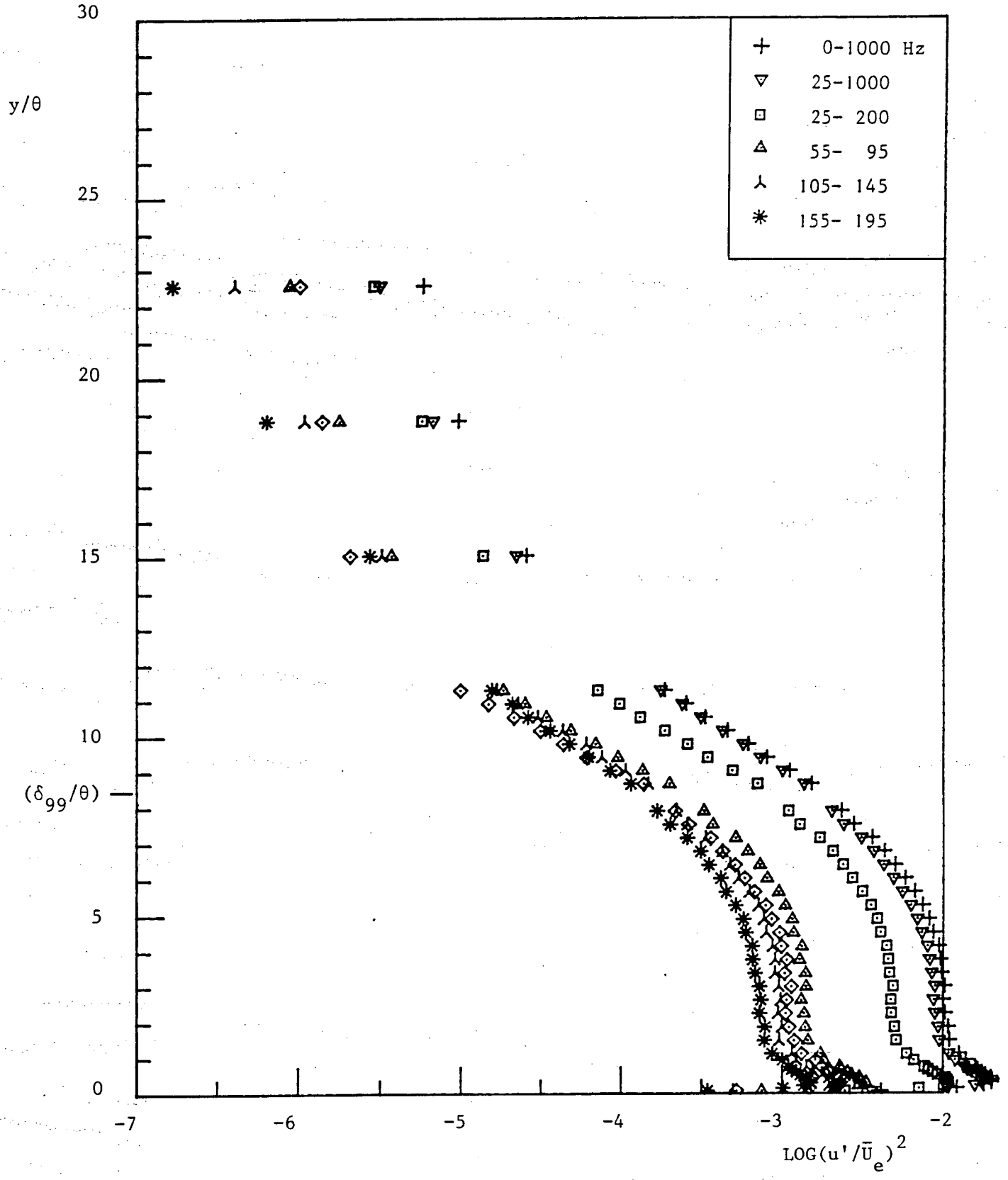

Figure 6.21g : Continued, x = 966 mm.

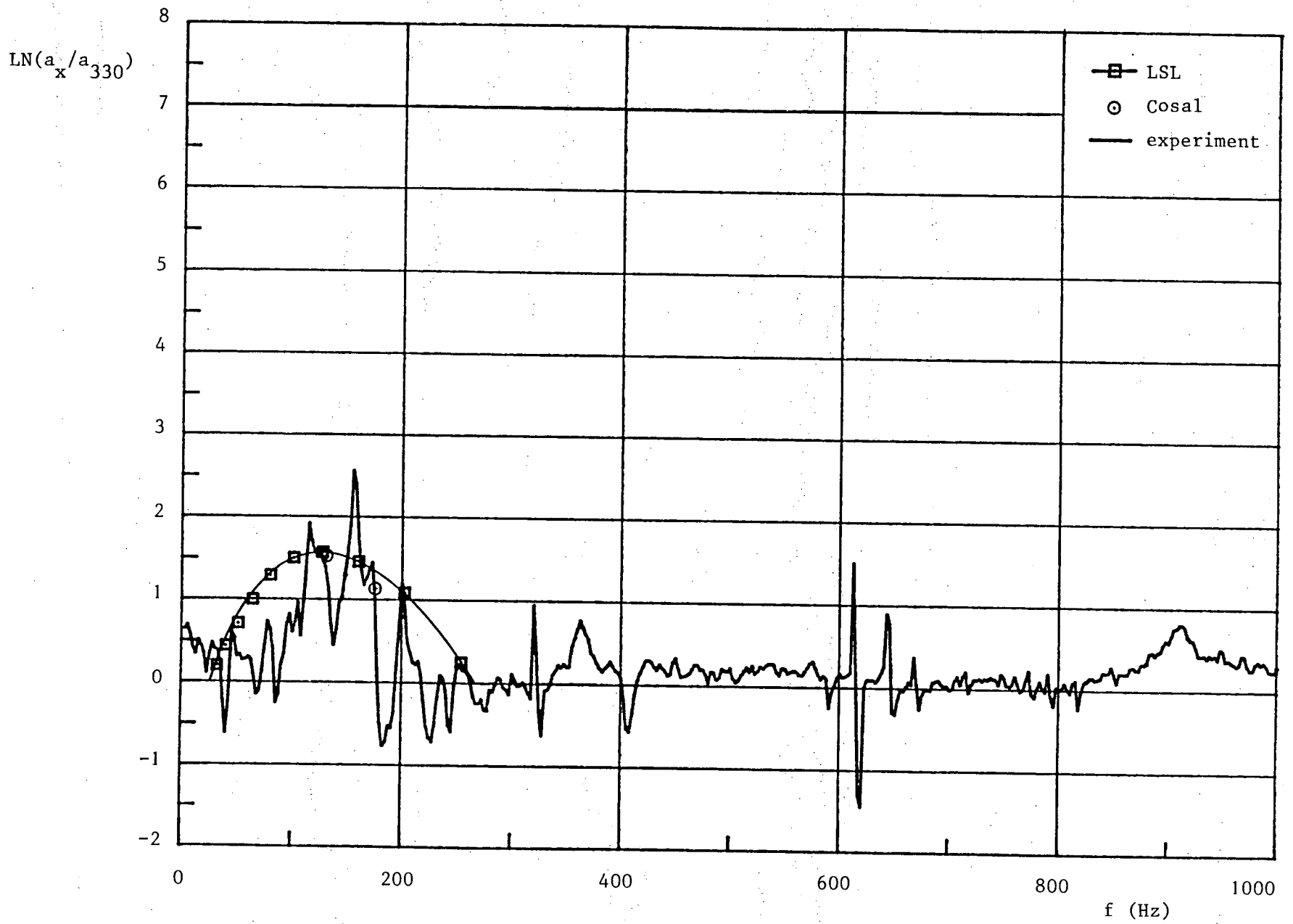

Figure 6.22a : Experimental amplification, compared with Cosal and LSL data, between x = 330^2 mm (y/θ = 0.52) and x = 396^2 mm (y/θ = 0.82). At x =330 mm, a calculated "n_{max}" value of 5 is found already.

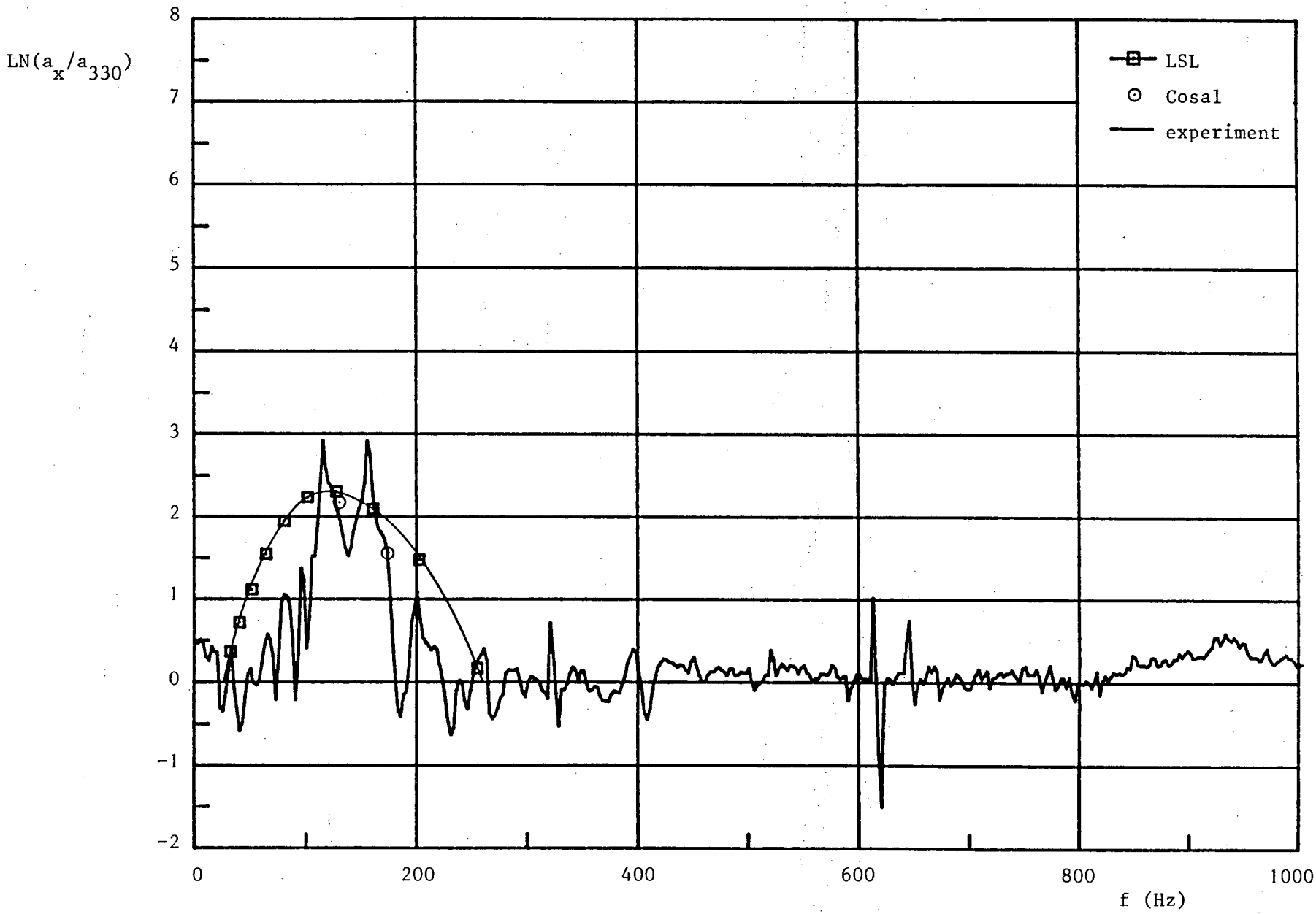

Figure 6.22b : Experimental amplification, compared with Cosal and LSL data, between x = 330^2 mm (y/θ = 0.52) and x = 430 mm (y/θ = 0.76).

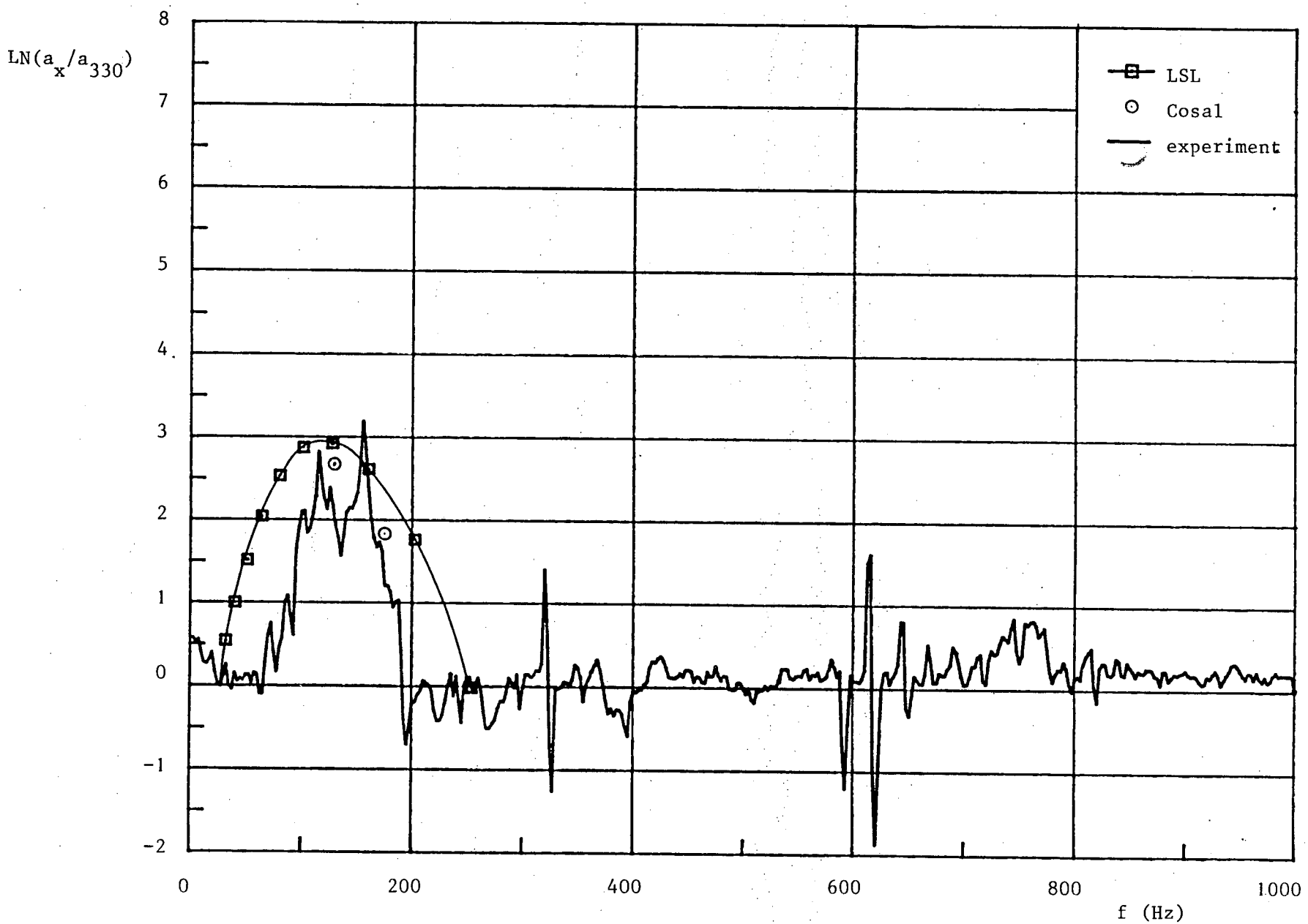

Figure 6.22c : Experimental amplification, compared with Cosal and LSL data, between x = 330[1] mm (y/θ = 0.49) and x = 458 mm (y/θ = 0.72).

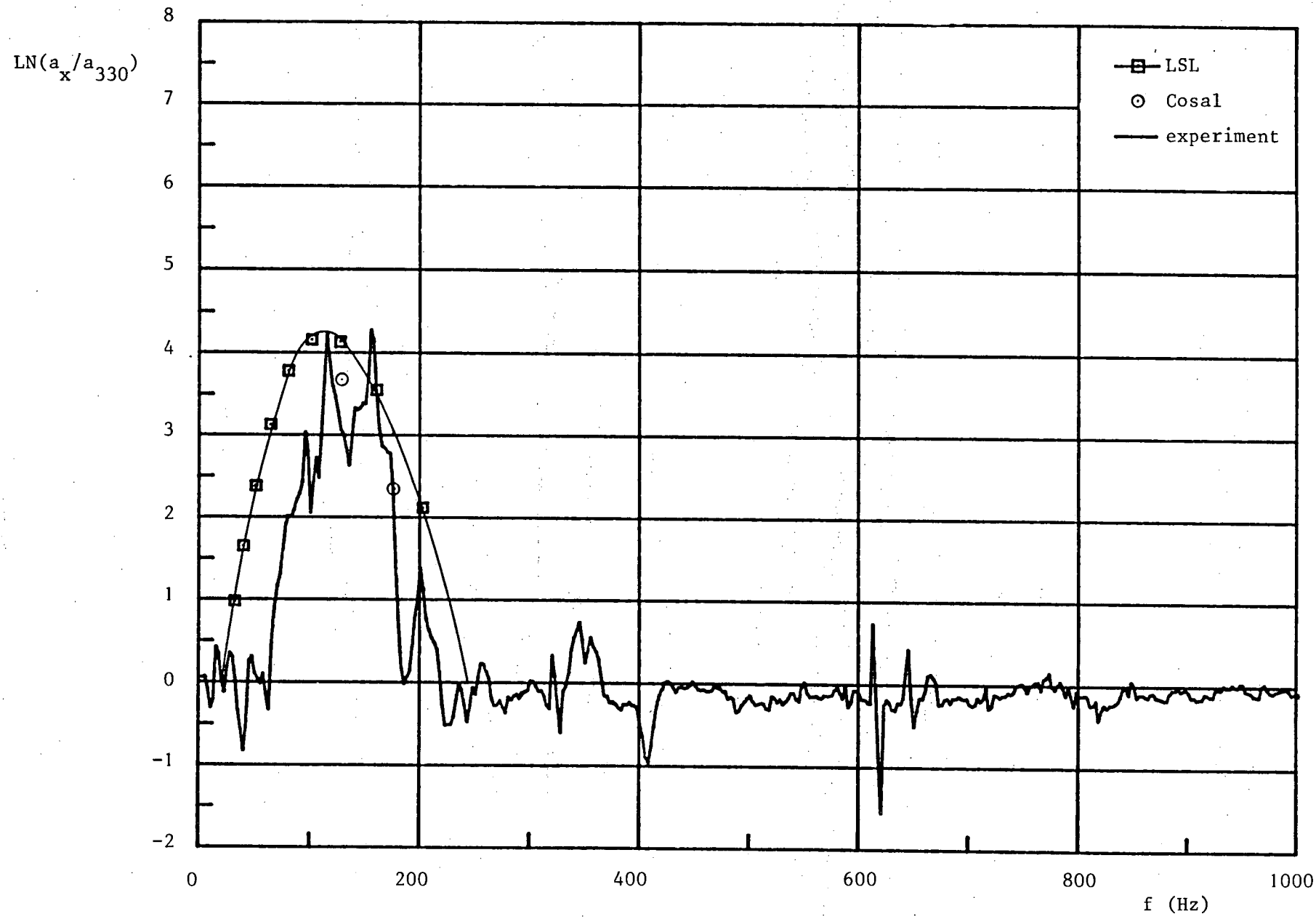

Figure 6.22d : Experimental amplification, compared with Cosal and LSL data, between $x = 330^2$ mm ($y/\theta = 0.52$) and x = 518 mm ($y/\theta = 0.57$).

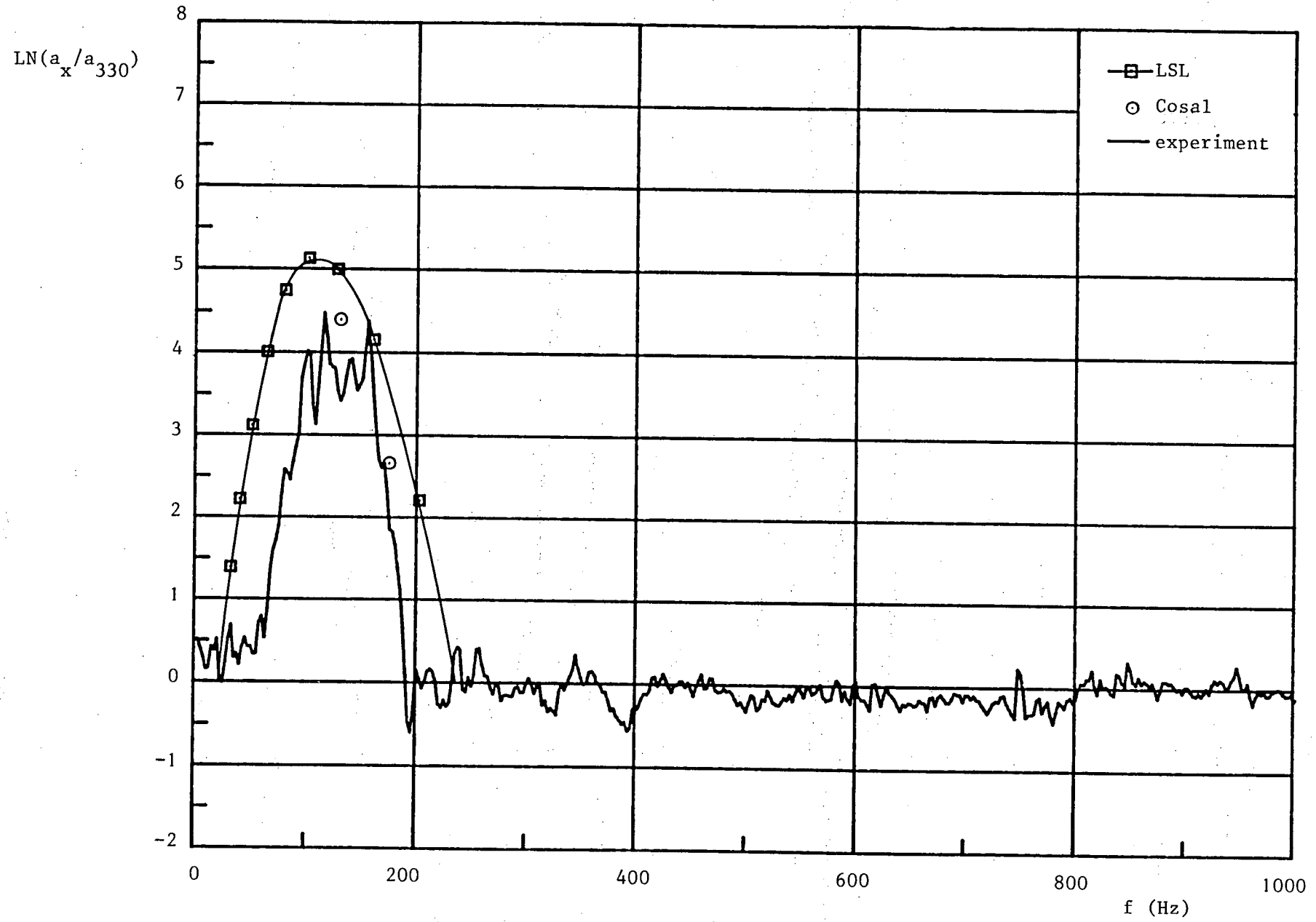

Figure 6.22e : Experimental amplification, compared with Cosal and LSL data, between x = 330[1] mm (y/θ = 0.49) and x = 568 mm (y/θ = 0.62).

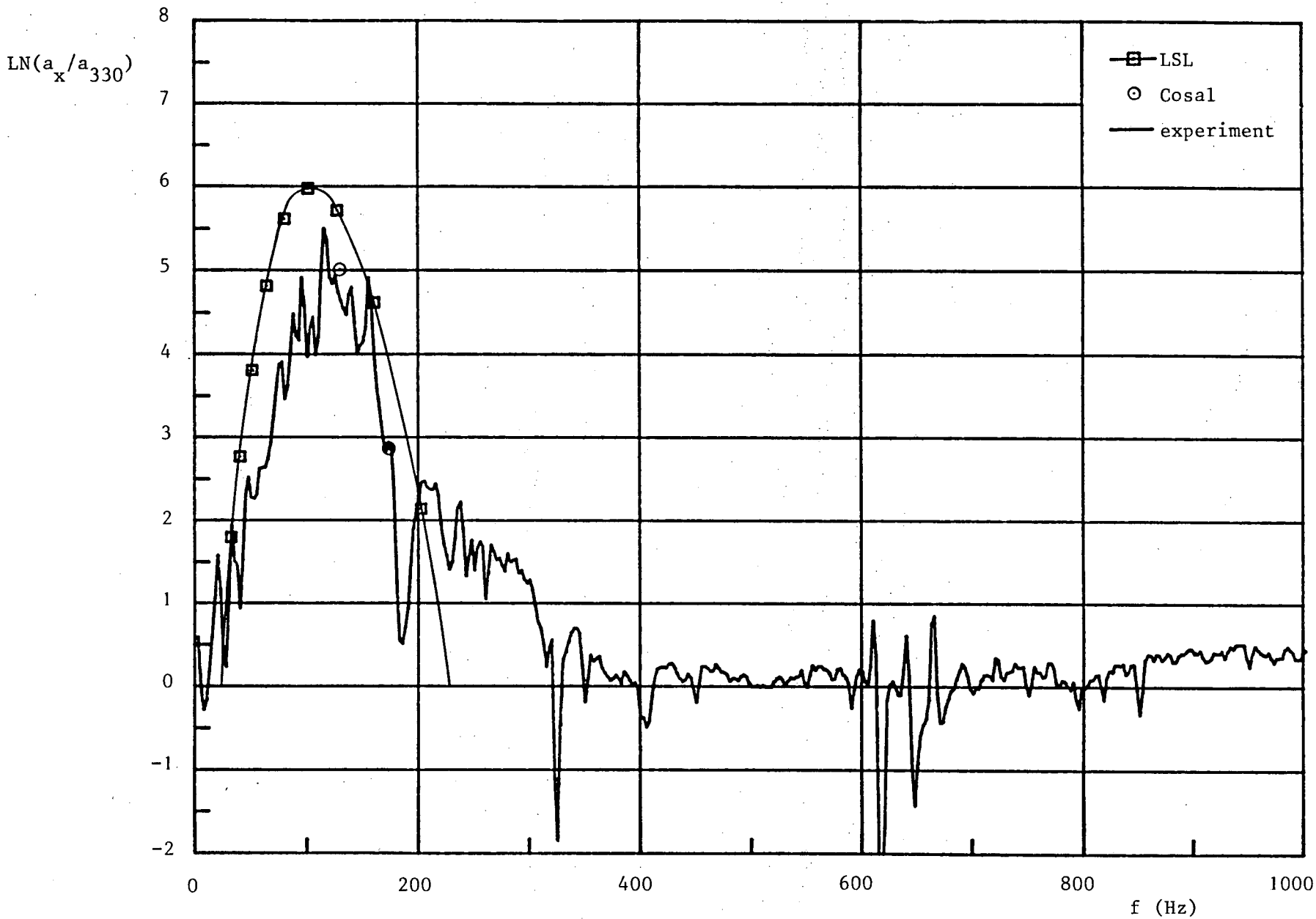

Figure 6.22f : Experimental amplification, compared with Cosal and LSL data, between x = 330^2 mm (y/θ = 0.52) and x = 616 mm (y/θ = 0.29).

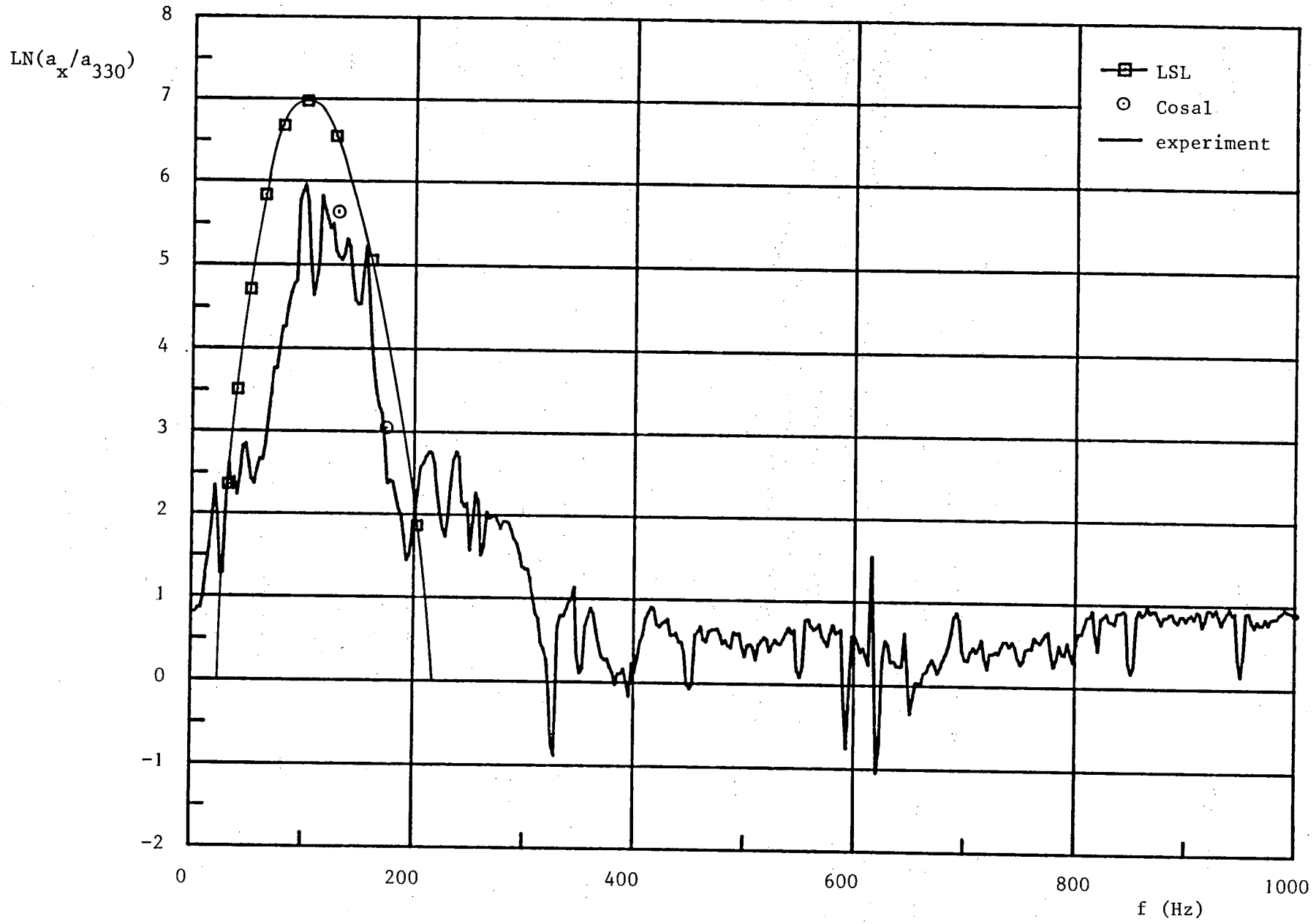

Figure 6.22g : Experimental amplification, compared with Cosal and LSL data, between x = 330[1] mm (y/θ = 0.49) and x = 673 mm (y/θ = 0.57).

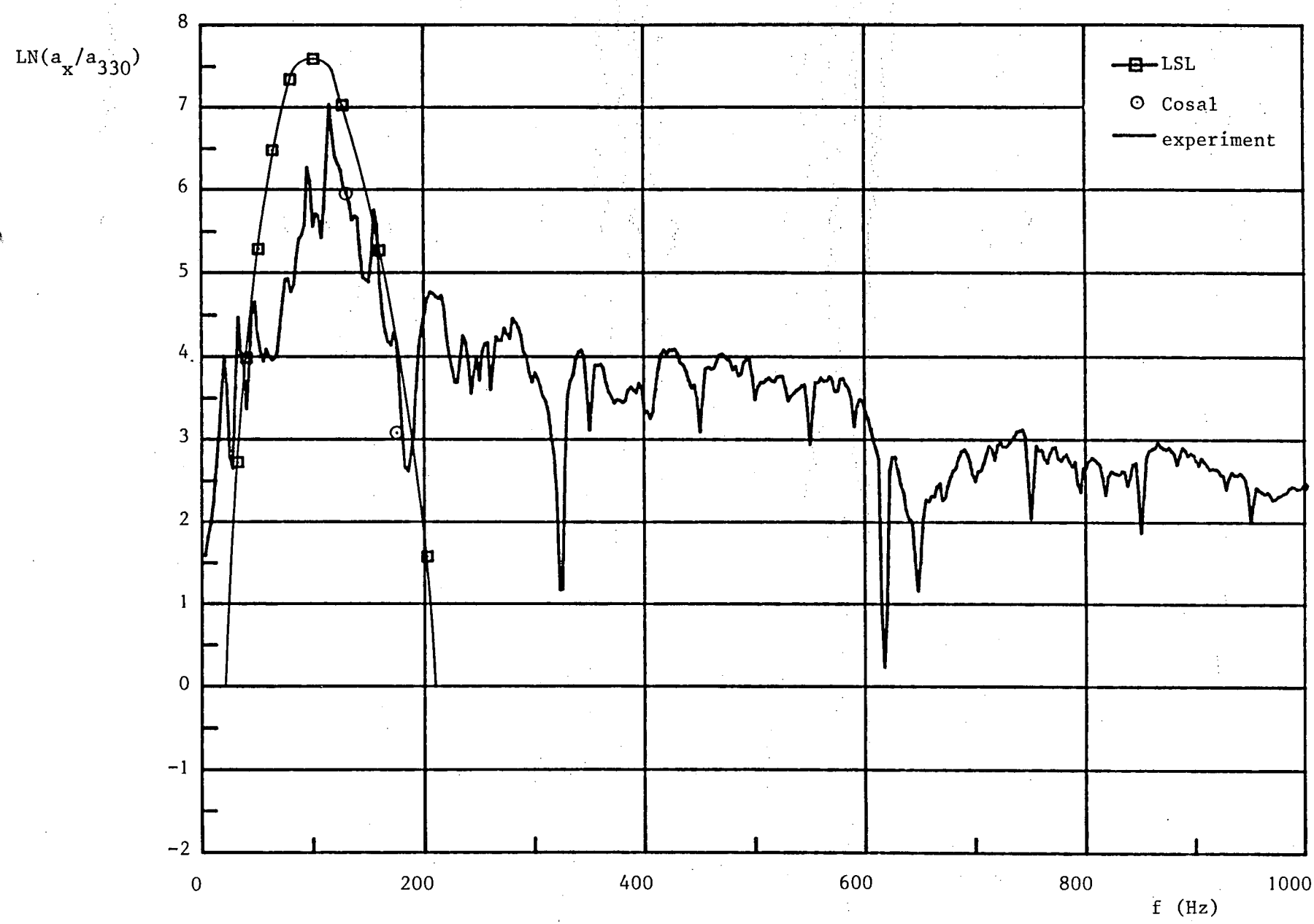

Figure 6.22h : Experimental amplification, compared with Cosal and LSL data, between x = 330^2 mm (y/θ = 0.52) and x = 709 mm (y/θ = 0.78).

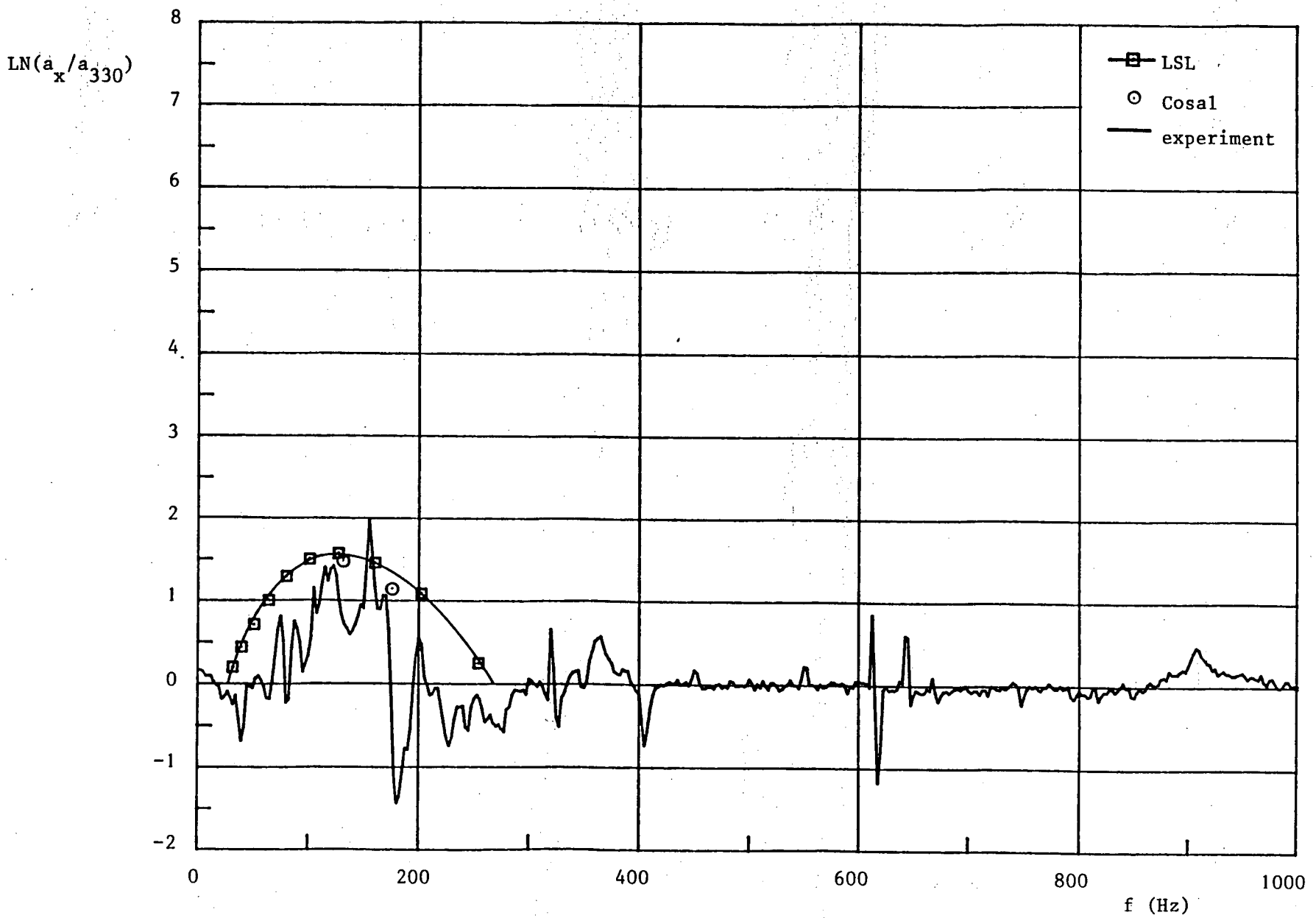

Figure 6.23a : Experimental amplification, compared with Cosal and LSL data, between x = 330^2 mm (y/θ = 2.53) and x = 396^2 mm (y/θ = 2.69).

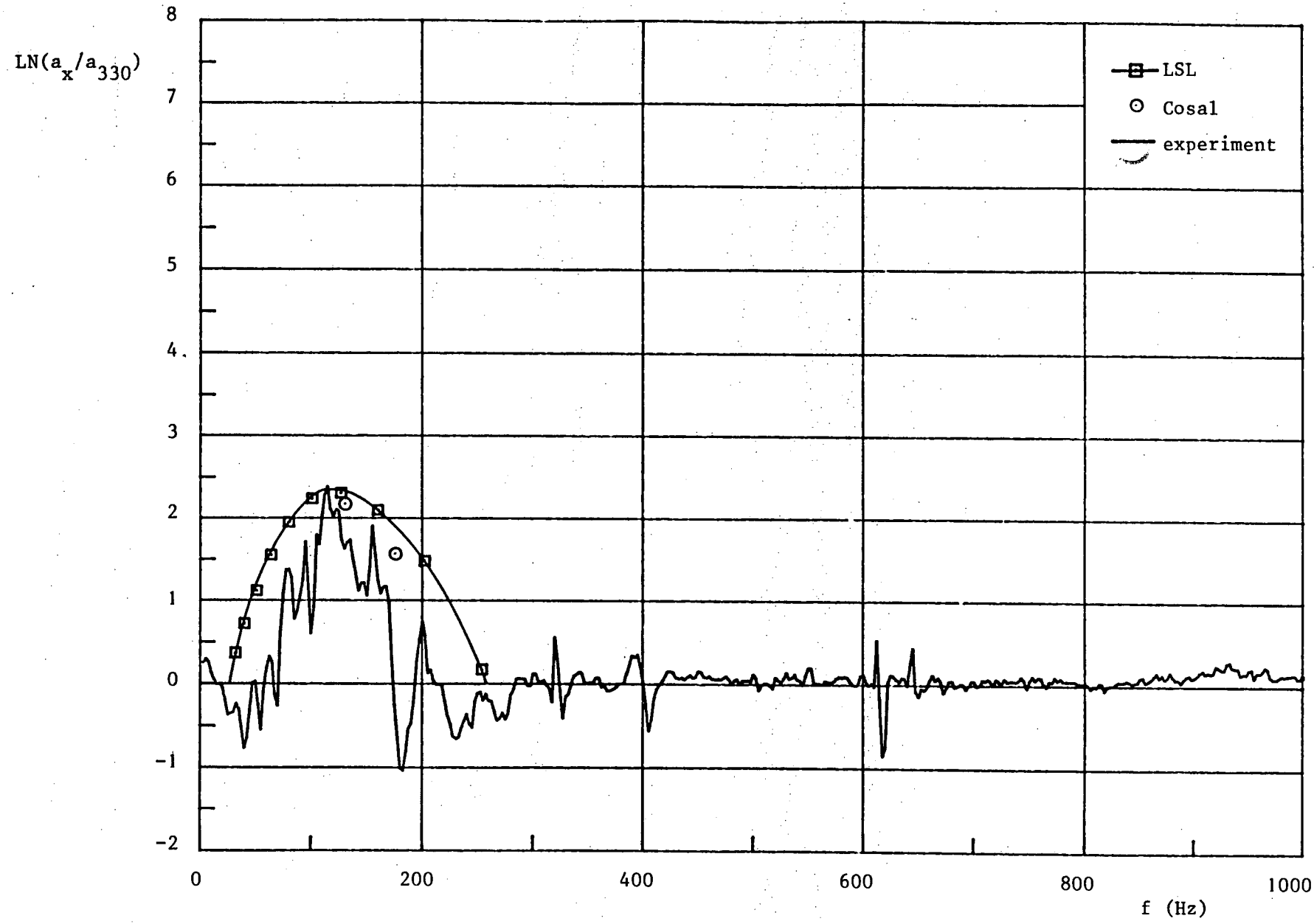

Figure 6.23b : Experimental amplification, compared with Cosal and LSL data, between x = 330^2 mm (y/θ = 2.53) and x = 430 mm (y/θ = 2.91).

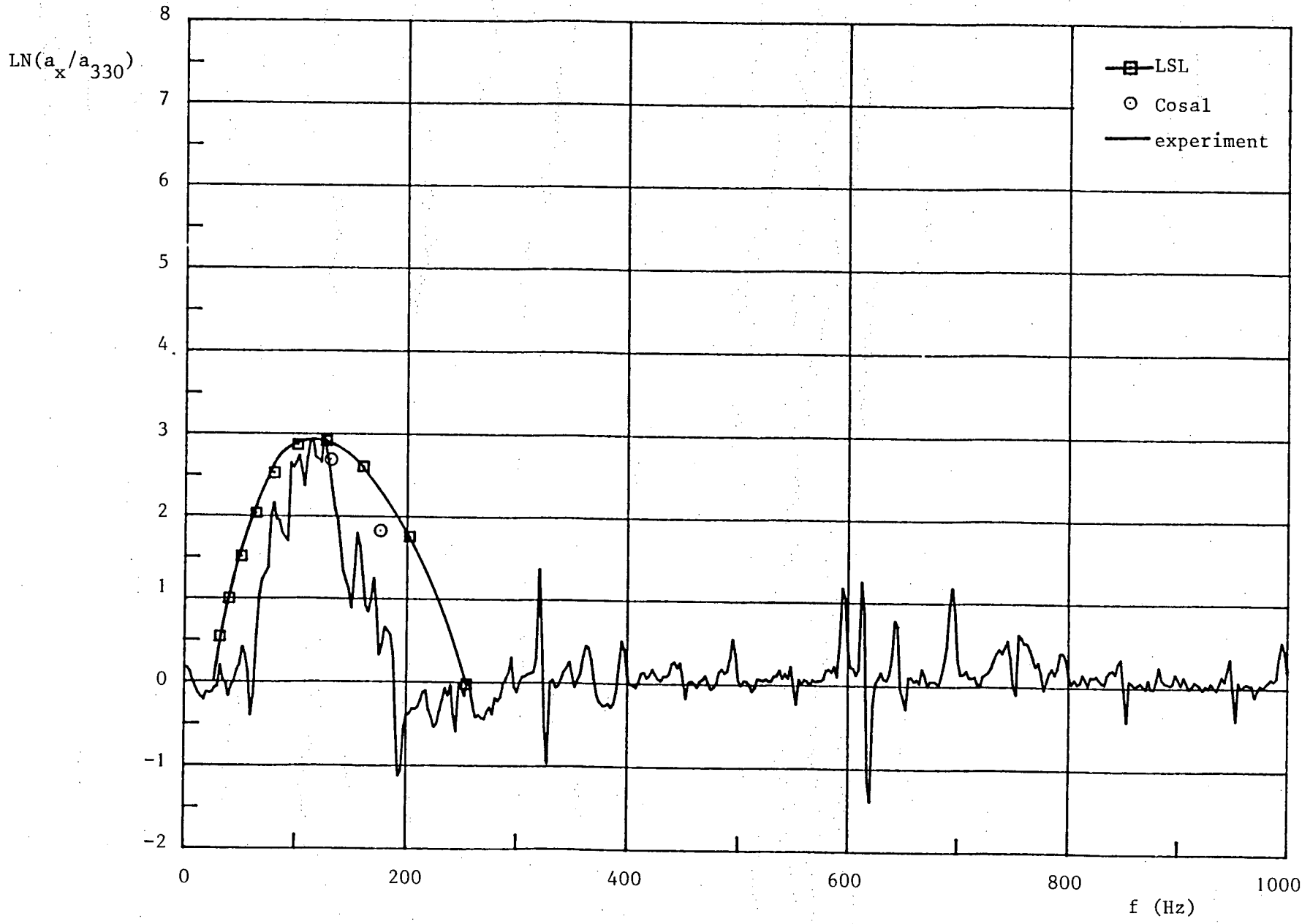

Figure 6.23c : Experimental amplification, compared with Cosal and LSL data, between x = 330[1] mm (y/θ = 2.50) and x = 458 mm (y/θ = 2.78).

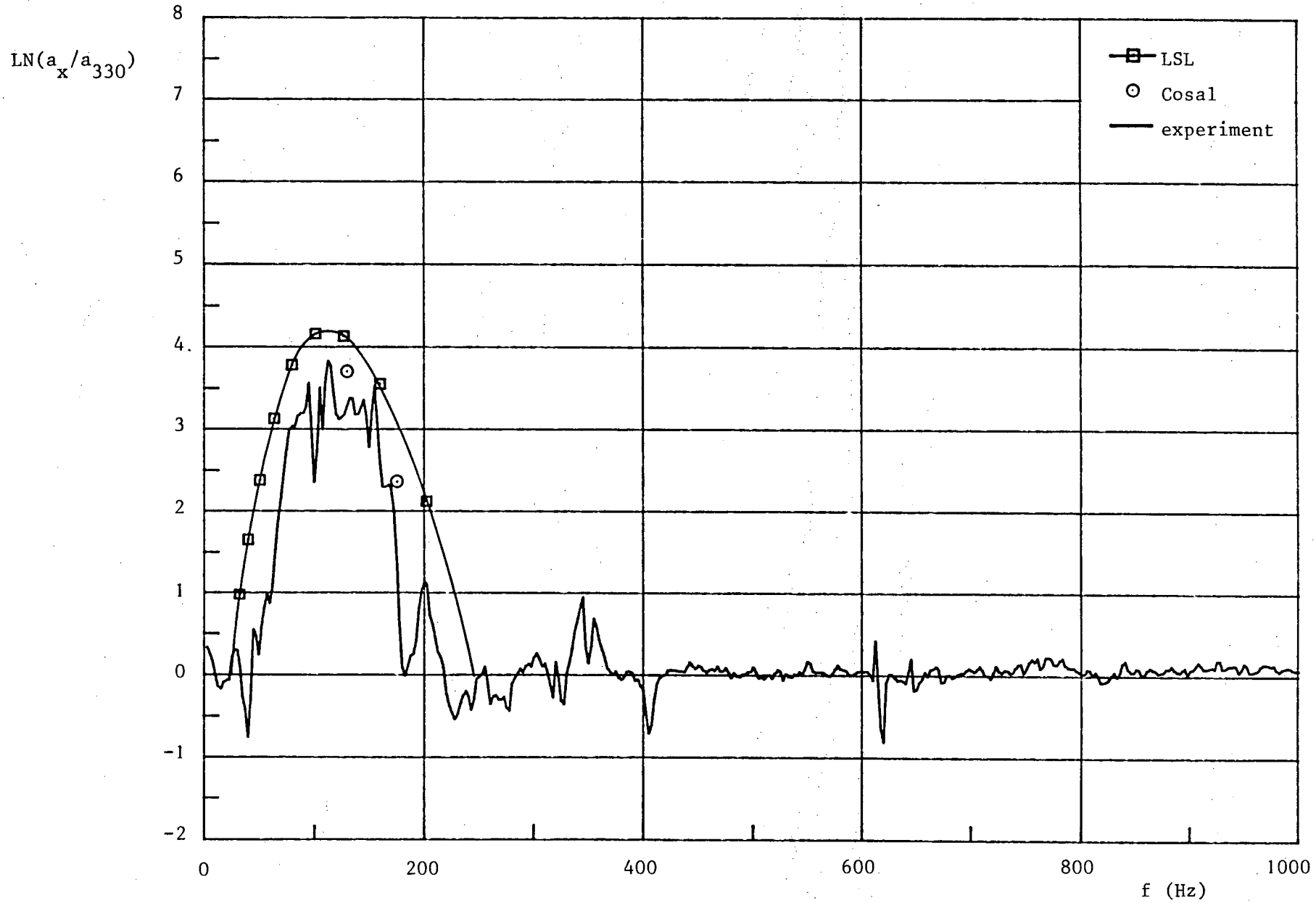

Figure 6.23d : Experimental amplification, compared with Cosal and LSL data, between x = 330^2 mm (y/θ = 2.53) and x = 518 mm (y/θ = 2.89).

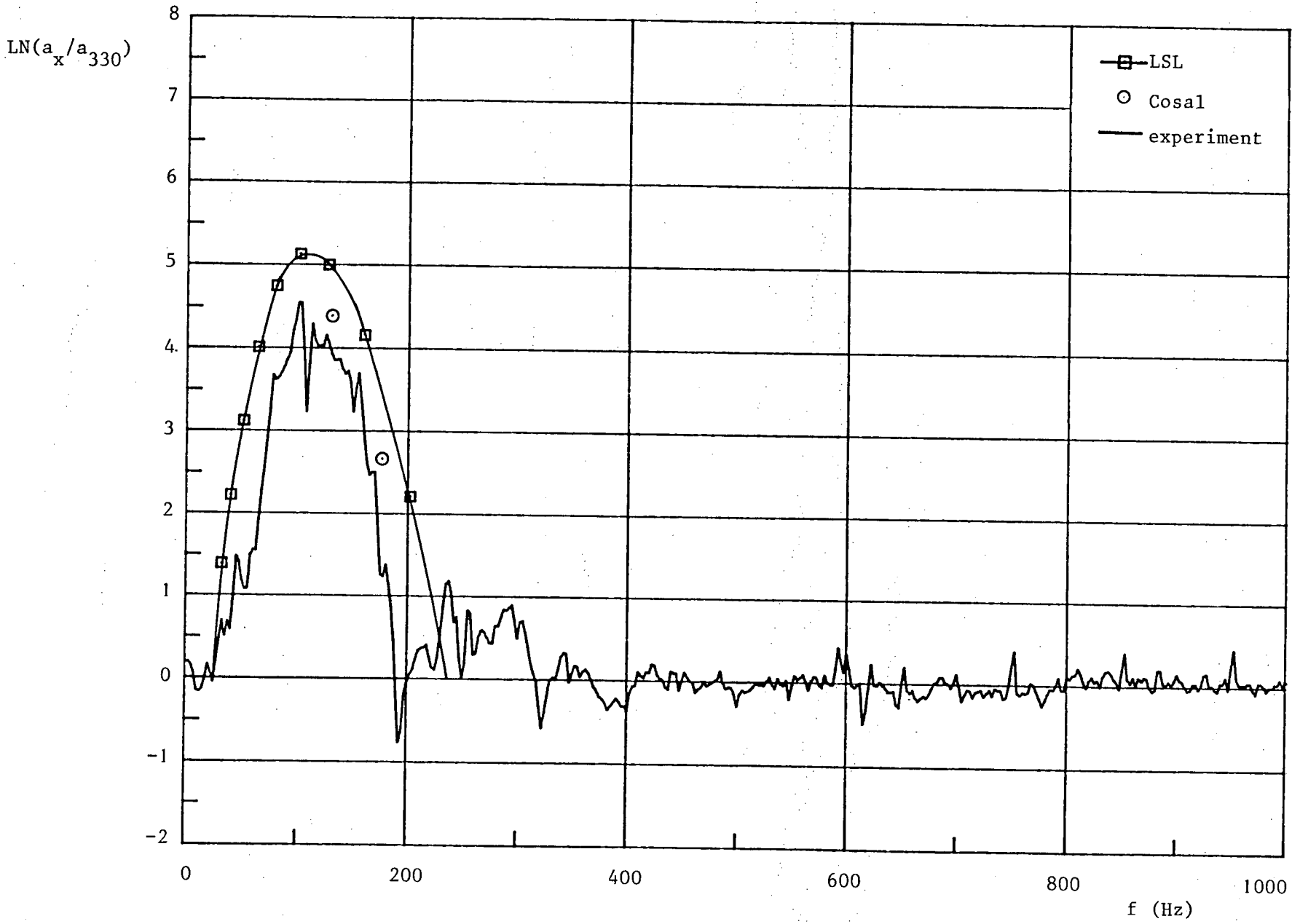

Figure 6.23e : Experimental amplification, compared with Cosal and LSL data, between x = 330[1] mm (y/θ = 2.50) and x = 568 mm (y/θ = 2.81).

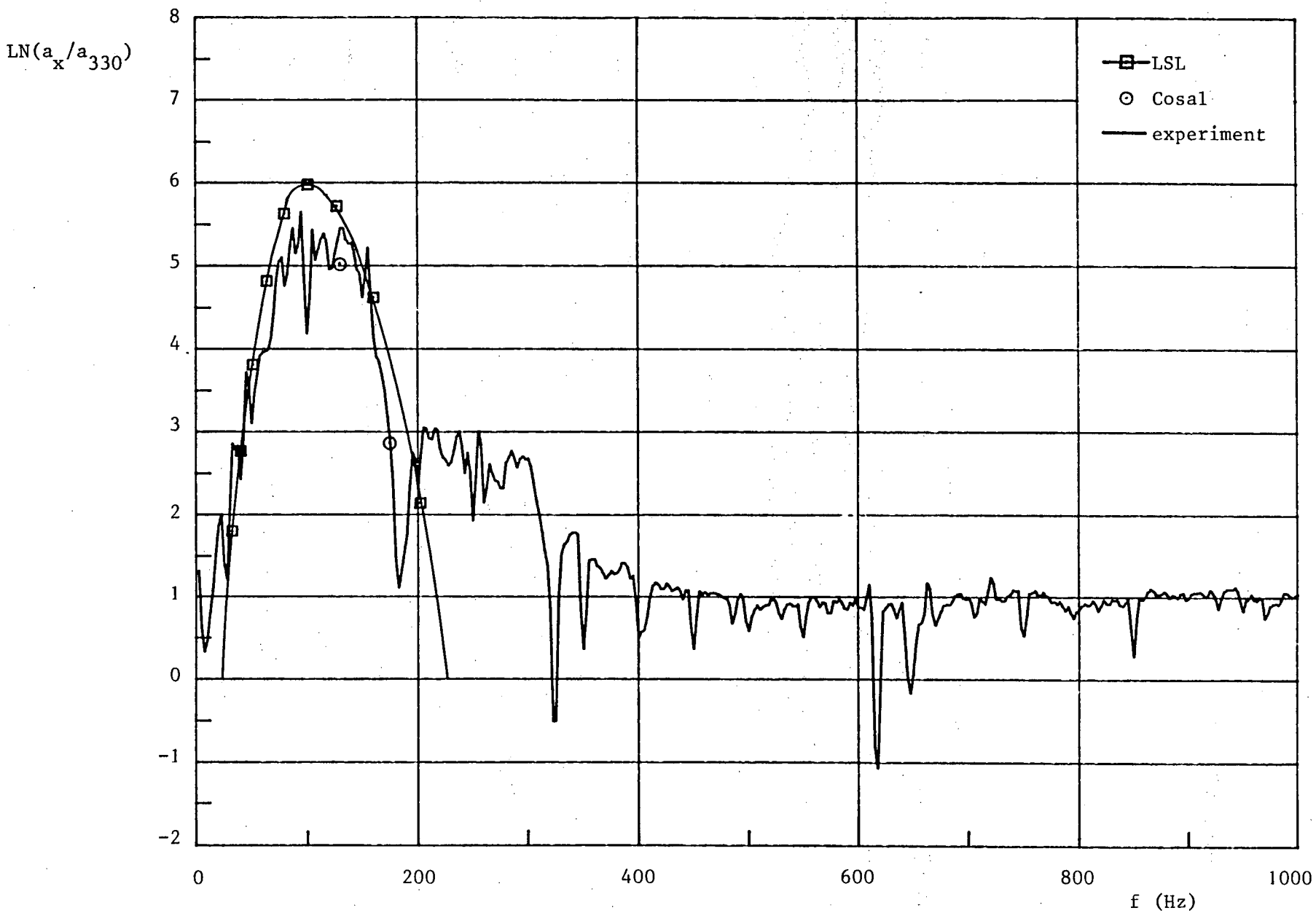

Figure 6.23f : Experimental amplification, compared with Cosal and LSL data, between x = 330^2 mm (y/θ = 2.53) and x = 616 mm (y/θ = 2.67).

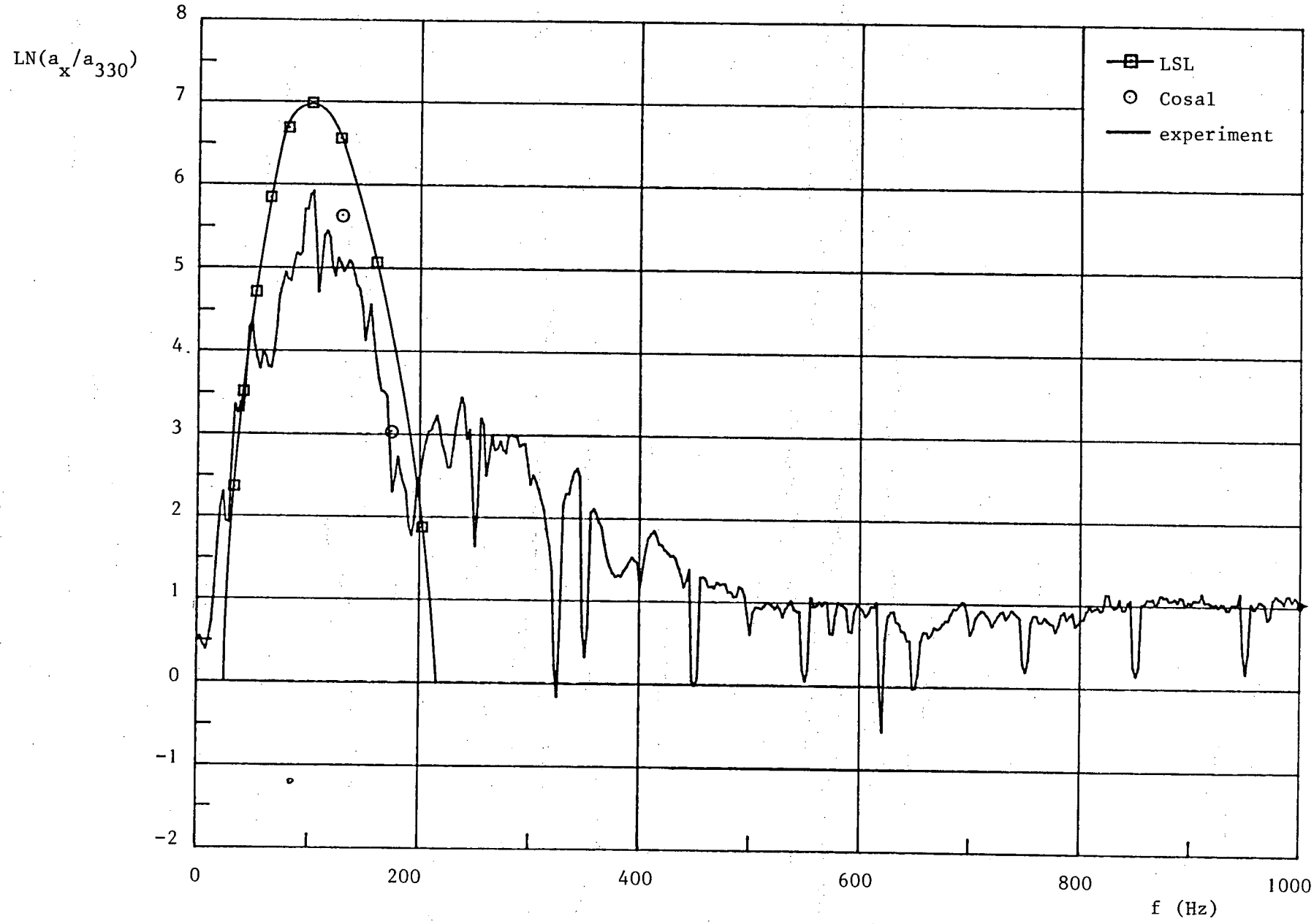

Figure 6.23g : Experimental amplification, compared with Cosal and LSL data, between x = 330[1] mm (y/θ = 2.50) and x = 673 mm (y/θ = 2.87).

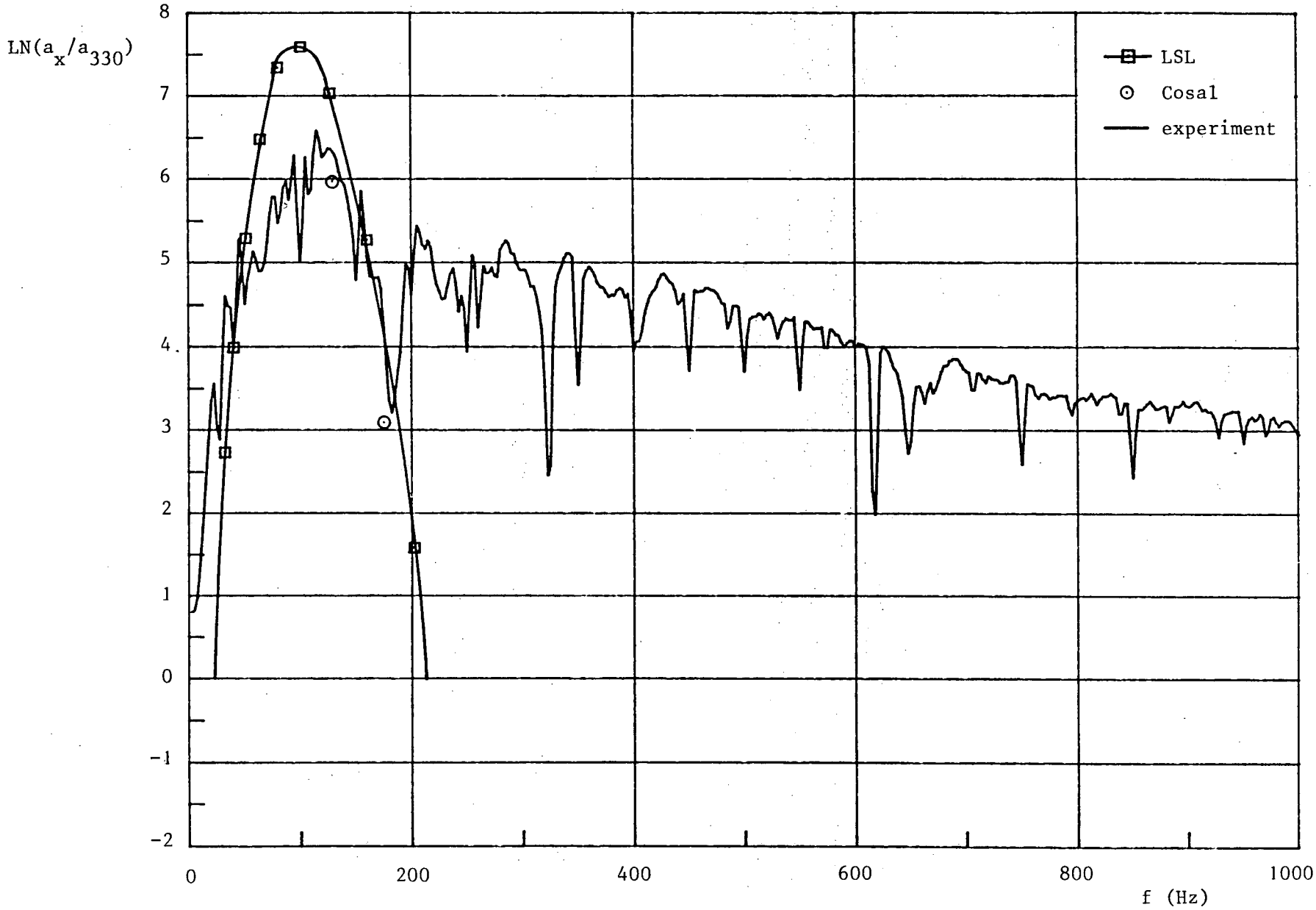

Figure 6.23h : Experimental amplification, compared with Cosal and LSL data, between x = 330^2 mm (y/θ = 2.53) and x = 709 mm (y/θ = 2.79).

APPENDIX A
POSITIONING OF HOT WIRE PROBE AND DETERMINATION OF DISTANCE TO THE WALL

The hot wire probe was illuminated with a Spindler & Hoyer spotlight and was observed with a Taylor Hobson telescope, placed behind the open end of the test section (figure A.1).
Two methods were applied to determine the distance of the hot wire in normal direction to the wall:

a. the reflection- or shadow image method;
b. the transparant ball method.

With regard to the first method, the wire was traversed over a distance y_1 and the projection $\Delta\ell'$ of $\Delta\ell$ between the hot wire and its reflected image in the test wall was measured with the telescope, Repeating this procedure, a graph was obtained in which y_1 was plotted as function of $\Delta\ell'$ (figure A.2).
Linear extrapolation to $\Delta\ell' = 0$, the value of y_{1_w}, at which the hot wire would touch the wall, was found. This procedure was performed at the tunnel speed used during boundary layer measurements. Because of the limited intensity of the spotted light in the tunnel, it was difficult to obtain clear reflection images of the wire.(The small angle between test wall and telescope made it impossible to observe the shadow image). Hence, another method was also applied in which a small transparant ball, with diameter 1 mm, was pressed against the wall at the considered boundary layer station.
The wall position was found at the point where the ball touched the reflected image. Further, a similar procedure was performed as above, with $\Delta\ell'$ measured with respect to the determined wall position.
Both methods showed a standard deviation of about 0.05 mm and were used interchangeable.

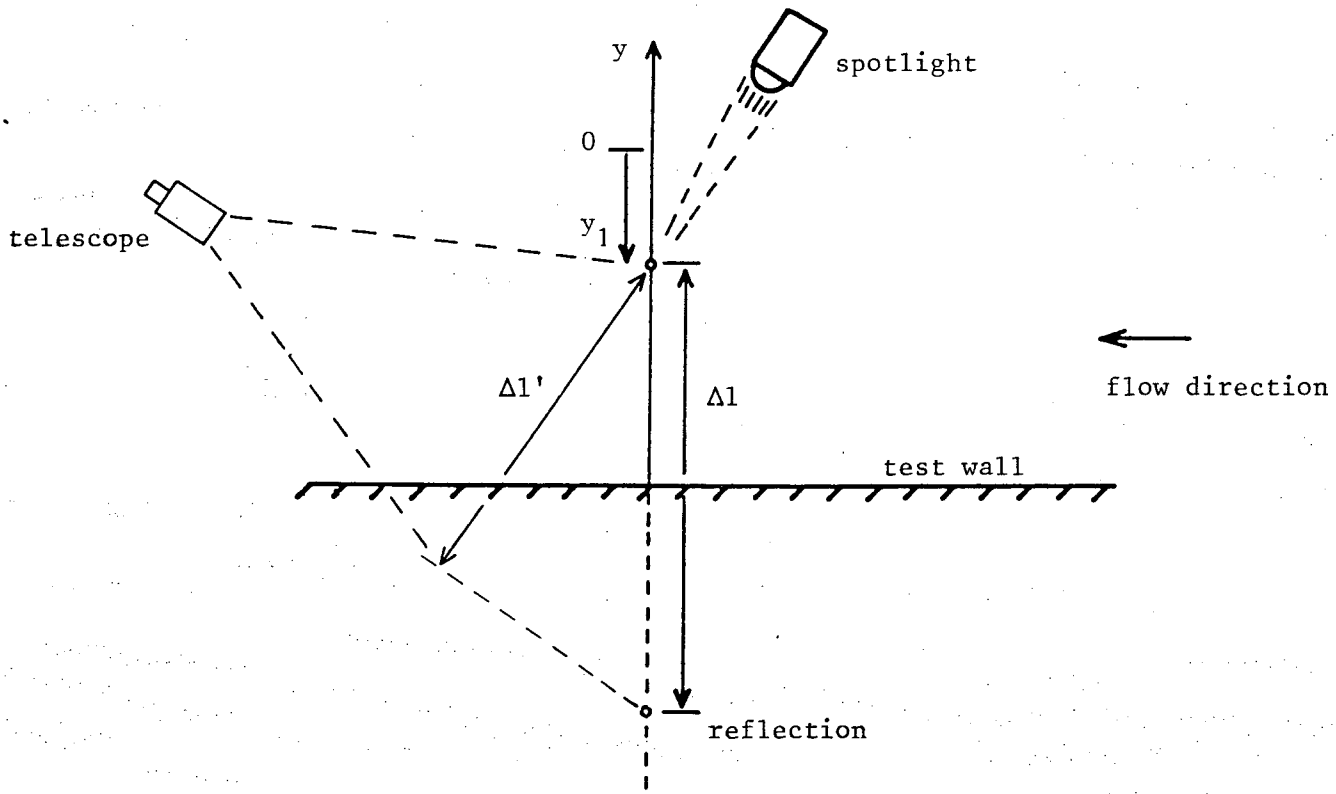

Figure A.1 : Schematic view of test set-up for determination of wall distance of hot wire.

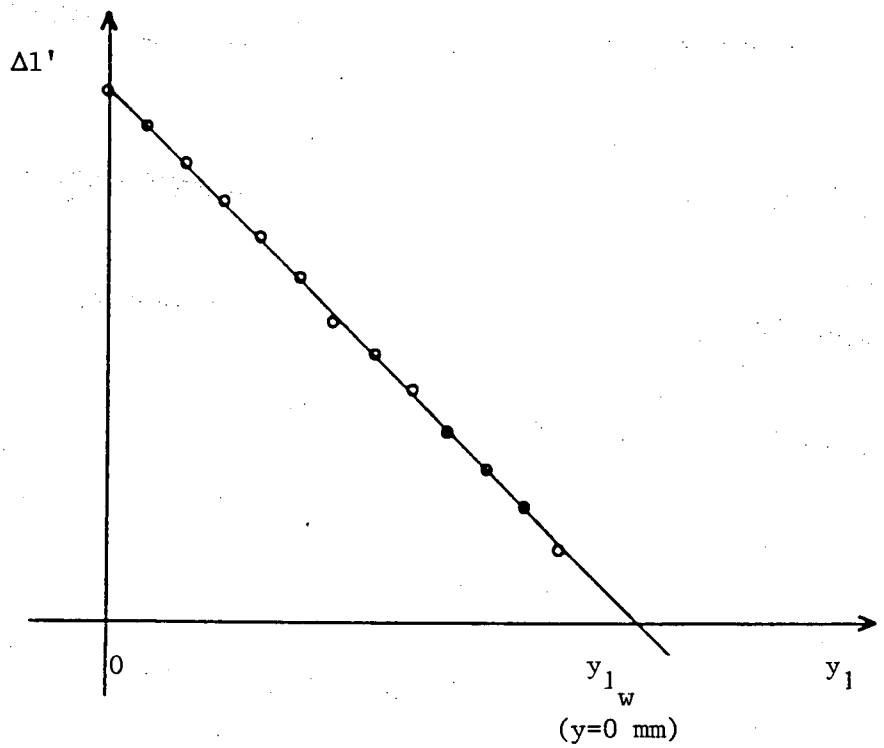

Figure A.2 : Determination of wall distance of hot wire by extrapolation.